Minimisation of optical pathlength noise for the detection of gravitational waves with the spaceborne laser interferometer LISA and LISA Pathfinder

Von der Fakultät für Mathematik und Physik der
Gottfried Wilhelm Leibniz Universität Hannover
zur Erlangung des Grades

Doktor der Naturwissenschaften
– Dr. rer. nat. –

genehmigte Dissertation von

Licenciado en Física
Antonio F. García Marín

geboren am 6. Mai 1979 in Almería, Spanien

2007

A mi abue.

Abstract

Gravitational waves were predicted by Albert Einstein in 1916 as a consequence of his theory of general relativity. Hulse and Taylor provided indirect experimental evidence of their existence based on the increasing rotation frequency of a pulsar in the binary star system PSR 1913+16. They were awarded with the Nobel price in 1993. The direct detection of gravitational waves is expected to be one of the most exciting advances in physics in the next years.

Currently, several large-scale laser interferometers [1] in different parts of the world constitute the main effort to observe gravitational waves, the most important projects being GEO600, LIGO, VIRGO and TAMA. The sensitivity of these ground-based laser interferometers is limited below 1 Hz by the unshieldable background of local gravitational noise and by the fact that ground-based interferometers are limited in length to a few kilometres.

The space project LISA (Laser Interferometer Space Antenna) aims to overcome this limitations and observe gravitational waves in the frequency range 10^{-4} Hz to 10^{-1} Hz, where the main sources expected are massive black holes and galactic binaries. The fundamental measurement of the LISA interferometry are the position fluctuations between two test masses separated by 5 million km, which constitutes one LISA arm. This challenging task is divided into two local measurements of a test mass with respect to the local optical bench plus one long-distance measurement between the local and remote optical benches. The local measurements with free-floating test masses will be tested on-orbit with a technology demonstration mission named LISA Pathfinder (LPF).

This thesis deals with the interferometric determination of the alignment and the position fluctuations of the free-floating test masses. The first part of the thesis presents the features of the local LISA interferometry and its capabilities: first, the laboratory implementation of the LISA pathfinder interferometry using the engineering model of the LPF optical bench is presented. The required sensitivity, dynamic range, and alignment capabilities are demonstrated. The first task of this interferometer in space will be the initial alignment of the test masses with respect to the optical bench. This procedure is implemented in the laboratory. Furthermore, a dedicated optical readout for the non-sensitive degrees of freedom of the test masses is also considered in order to reduce cross-coupling from these coordinates in the main measurement axis. A breadboard demonstration of an optical readout based on a "deep internal phase modulation" is presented.

The second part of this thesis analyses various interferometric noise sources. First, a thorough analysis of the implementation of the laser control loops for LPF is done, with emphasis on the direct technology transfer for LISA. The most challenging noise source for the LISA interferometry is the frequency, because more than eleven orders of magnitude of laser noise have to be suppressed with a combination of three techniques. One of these techniques is the so-called arm-locking: Using a hardware simulation of the LISA configuration, it is demonstrated for the first time that the frequency of the laser can be locked to the length of a LISA arm with higher control bandwidth than the inverse of the light round-trip travel time. Another important noise source are the optical windows of the vacuum enclosures containing the test masses, as they constitute the only transmissive elements of the interferometer that are not bonded on an ultra stable optical bench. Optical window prototypes manufactured using a specially selected athermal glass are included in the optical path of the LPF interferometric demonstration, which shows that the windows do not affect the interferometric performance.

Keywords: Gravitational waves, space interferometry, laser control loops

Kurzzusammenfassung

Albert Einstein sagte 1916 die Existenz von Gravitationswellen als eine Konsequenz seiner Allgemeinen Relativitätstheorie voraus. Hulse und Taylor lieferten einen indirekten experimentellen Beweis für Gravitationswellen, der auf der zunehmenden Rotationsfrequenz eines Pulsars im Doppelsternsystem PSR 1913+16 beruht. Sie erhielten dafür 1993 den Nobelpreis. Die direkte Detektion von Gravitationswellen wird in den nächsten Jahren voraussichtlich einer der aufregendsten Fortschritte der Physik.

Momentan konzentrieren sich die Bemühungen zur Beobachtung von Gravitationswellen auf mehrere große Interferometer auf verschiedenen Kontinenten, wobei GEO600, LIGO, VIRGO und TAMA die wichtigsten Projekte sind. Die Empfindlichkeit dieser erdgebundenen Interferometer ist unter 1 Hz limitiert, da der Hintergrund von lokalem Gravitationsrauschen nicht abschirmbar ist und die Länge der Interferometer auf wenige Kilometer begrenzt ist.

Das Weltraumprojekt LISA (Laser Interferometer Space Antenna) soll diese Begrenzungen überwinden und Gravitationswellen im Frequenzbereich von 10^{-4} Hz bis 10^{-1} Hz beobachten, wo als Hauptquellen massive schwarze Löcher und Binärsysteme in unserer Galaxie erwartet werden. Die grundlegende Messung in der LISA-Interferometrie sind Abstandsänderungen zwischen zwei Testmassen, die fünf Millionen Kilometer voneinander entfernt sind. Dieser Abstand stellt einen sogenannten LISA-Arm dar. Diese herausfordernde Aufgabe unterteilt sich in zwei lokale Messungen der Testmassenposition bezüglich der jeweiligen lokalen optischen Bank und eine Langstreckenmessung zwischen der lokalen und der entfernten optischen Bank. Die lokalen Messungen an freischwebenden Testmassen werden mit einer Weltraummission namens LISA Pathfinder getestet, die zur Überprüfung der LISA-Technologie dient.

Die vorliegende Arbeit beschäftigt sich mit der interferometrischen Bestimmung der Winkelfreiheitsgrade und der Positionsfluktuationen der freischwebenden Testmassen. Der erste Teil der Arbeit behandelt die lokale LISA-Interferometrie: Zunächst wird die Implementierung der LISA-Interferometrie im Labor mit Hilfe des Engineering Models der optischen Bank des LPF vorgestellt. Die benötigte Empfindlichkeit, der dynamische Bereich und Möglichkeiten zur Justage werden demonstriert. Die erste Aufgabe des Interferometers im Weltraum wird die anfängliche Justage der Testmassen bezüglich der optischen Bank sein. Diese Prozedur wird im Labor realisiert. Darüber hinaus wird auch ein optisches Auslesen der unempfindlichen Freiheitsgrade der Testmassen betrachtet, um die Querkopplung dieser Koordinaten an die zu messende Armlänge zu reduzieren. Eine praktische Umsetzung des optischen Auslesens im Labor, die auf „tiefer interner Phasenmodulation" beruht, wird vorgestellt.

Der zweite Teil dieser Arbeit analysiert verschiedene interferometrische Rauschquellen. Zunächst wird die Realisierung der Laserregelkreise des LPF sorgfältig untersucht, wobei das Hauptgewicht auf dem direkten Technologietransfer zu LISA liegt. Die Frequenz ist die herausfordernste Rauschquelle bei der LISA-Interferometrie, da mehr als elf Größenordnungen von Laserrauschen durch eine Kombination dreier verschiedener Techniken unterdrückt werden müssen. Eine dieser Techniken ist das sogenannte Armlocking: Mit Hilfe einer Hardware-Simulation der LISA-Konfiguration wird in dieser Arbeit erstmals demonstriert, dass bei Verwendung der Länge des LISA-Arms als Referenz die Laserfrequenz mit größerer Kontrollbandbreite als das Inverse der Lichtumlaufzeit stabilisiert werden kann. Die optischen Fenster des Vakuumtankes, der die Testmassen umschließt, stellen eine weitere wichtige Rauschquelle dar, da diese die einzigen lichtdurchlässigen Elemente des Interferometers sind, die nicht auf eine ultra-stabile Bank gebondet sind. Prototypen der optischen Fenster, die aus speziell ausgewähltem athermischen Glas hergestellt sind, werden im LPF Interferometer-Prototyp in den optischen Weg eingebracht. Diese Untersuchung ergibt, dass die Fenster die Empfindlichkeit des Interferometers nicht beeinflussen.

Schlagworte: Gravitationswellen, Weltrauminterferometrie, Laserstabilisierung

Contents

List of figures

List of tables

List of Abbreviations

A/D	analogue to digital
AEI	Albert-Einstein-Institute, Hannover
AOM	acousto-optic modulator
AR	anti-reflection
BS	beam splitter
c	interferometric contrast, speed of light in vacuum
CAD	computer-aided design
DC	very low or zero frequency
DMU	data management unit
DWS	differential wavefront sensing
ESA	european space agency
FFT	fast Fourier transform
FPGA	field programmable gate array
GEO600	British-German gravitational-wave detector
het	heterodyne
IGR	Institute for gravitational research, Glasgow
IEEC	Instituto de estucios espaciales de Cataluña, Barcelona
LISA	laser interferometer space antenna
LPF	LISA Pathfinder
LTP	LISA technology package
LSD	linear spectral density
LPSD	linear frequency axes power spectral density
NASA	National Aeronautics and Space Administration
mod	modulation
NPRO	non-planar ring oscillator
PBS	polarising beam splitter
PD	photodiode (see QPD and SED)
PDH	Pound-Drever-Hall
PM	phasemeter
PZT	piezo-electric transducer

QPD	quadrant photodiode
SED	single element photodiode
RF	radio frequency
rms	root mean square
SBDFT	single bin discrete Fourier transfor
SNR	signal-to-noise ratio
VCO	voltage controlled oscillator

Part I.

Interferometric determination of test mass position fluctuations

Chapter 1.

LISA overview

The Laser Interferometer Space Antenna (LISA) is a joint ESA-NASA mission designed to observe gravitational waves in the frequency range between 0.1 to 100 mHz, where ground-based detectors are limited by terrestrial noise. Sources in this frequency range include supermassive black holes and galactic binary stars. LISA consists of three identical spacecraft separated by 5 million kilometers carrying a total of six free flying test masses in heliocentric drag-free orbit. The fluctuations in separation between two of these test masses located in different satellites will be measured by laser interferometry with picometre precision.

This chapter presents a brief overview of the LISA mission with special emphasis on the interferometry, the research field of this work.

1.1. Introduction

This chapter does not aim to present a complete description of the LISA mission design, as this would not even probably fit in the whole thesis. As usual in a project of this scale, the published literature about LISA is sometimes very specific and discusses either one of the many required technology developments or one of the many predicted scientific results. It is thus not trivial to find one source of literature that will satisfy the different backgrounds of readers potentially interested in LISA. The following references summarise the starting points from which most of what has been published can be found:

- Brief general overviews of the mission can be read in [5, 6].
- Several documents going from public outreach to the latest scientific achievements can be found in the LISA International Scientific Community (LISC) website [7], as well as links to the different research groups and institutions working on LISA.
- The proceedings of the biannual LISA Symposiums constitute probably the most complete collections of scientific papers about LISA. The last two of them can be found in [8] and [9].
- The most accurate formulation of the LISA baseline design has been published during the years in the form of extensive technical reports resulting from different major industrial studies of the mission [10, 2, 11]. They can all be found, together with other relevant mission documentation, in the ESA official website of LISA [12].

Currently a mission formulation study is underway and some of its preliminary results have been already published [13].

The configuration of the LISA constellation is shown schematically in Figure 1.1. The three satellites form an equilateral triangle that orbits the sun following the earth at a distance of 50 million kilometer. This orbit provides a highly stable environment for the free-floating test masses in the relevant frequency range.

The 5 m km long sides of the triangle are defined by two free floating test masses from different satellites: each satellite is equipped with two free-floating test masses and two telescopes aligned (in $60°$) towards the other two satellites, so that the line of sight between two test masses in different satellites that face each other through the telescopes is a LISA arm.

Using the telescopes, two test masses placed in different satellites can be "linked" with a laser beam that uses them as end mirrors of an interferometer. This way, the fluctuations of the 5 million km that separate them (a LISA arm) can be monitored. The combination of two such LISA arms can be used as a Michelson-like interferometer to detect gravitational waves. Several other interferometric combinations are possible [2].
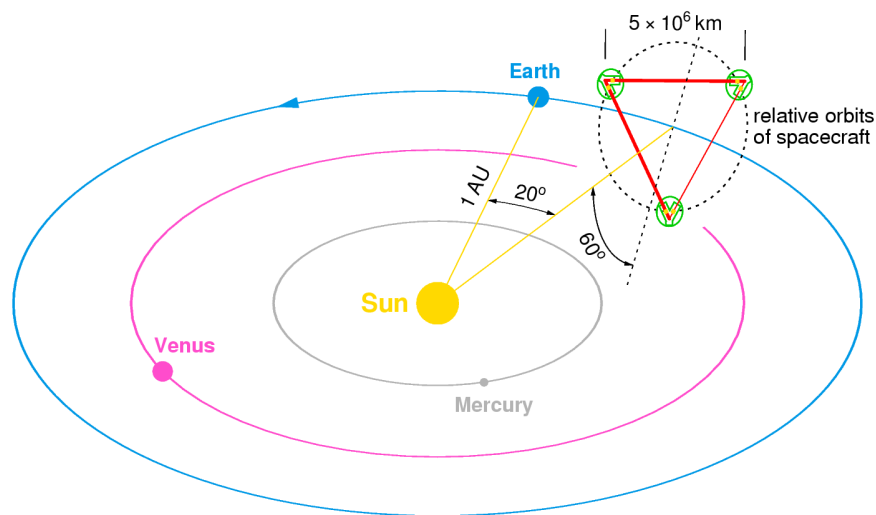
Figure 1.1: The LISA configuration: the three satellites form an equilateral triangle with sides of 5 million km. It follows the earth at a distance of 50 million kilometer. The armlength are blown up by more than an order of magnitude. Source [2].

1.2. **LISA sensitivity**

The designed LISA sensitivity h to gravitational waves sources is shown in Figure 1.2. LISA will achieve a its best sensitivity at the millihertz frequency range

$$h_{\text{best}} = \frac{2\delta l}{L} = 10^{-23}, \tag{1.1}$$

where δl are the detected fluctuations of the armlength and L the armlength of 5 million km. This sensitivity is comparable to that of the ground-based detectors at higher frequencies, and it has been calculated under the assumptions of one year observation time, a signal-to-noise ratio of 5 and averaging over all possible sources locations and polarisations.
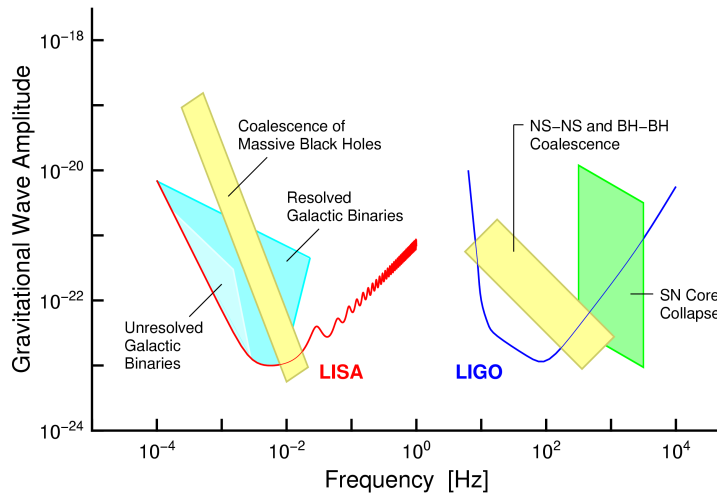
Figure 1.2: The LISA sensitivity at low frequencies is comparable to that of the ground-based gravitational wave detectors. This sensitivity is calculated for an observation time of one year and a signal to noise ratio of 5, averaged over all possible source locations and polarisations. Source [2].

LISA relies on two main technologies to achieve the target sensitivity: the free-falling test masses and the interferometric measurement system. In this sense, there are two main groups of noise sources for LISA: apparent pathlength noise sources that limit the interferometer sensitivity to real position fluctuations of the test masses, and acceleration noise that limit the performance of the drag-free control systems [14] at keeping the test masses in perfect free-fall.

The total estimated apparent pathlength noise is $40\,\text{pm}/\sqrt{\text{Hz}}$ and the acceleration noise $3 \cdot 10^{-15}\,\text{m\,s}^{-2}/\sqrt{\text{Hz}}$. The acceleration noise will lead to displacement errors of the test masses that will dominate the detector sensitivity below $1\,\text{mHz}$, as they scale as $1/f^2$ towards low frequencies. Between $1\,\text{mHz}$ and $10\,\text{mHz}$, the apparent pathlength noise of the interferometer will limit the detector sensitivity, and above $10\,\text{mHz}$ the antenna pattern of the interferometer reduces the sensitivity proportionally to the frequency.

In order to express the total requirements for the implementation of the interferometry and drag-free control system, it has to be taken into account that integrating the acceleration noise two times leads to position noise. In this sense, the requirements for the interferometer can be relaxed at low frequencies, as the detector noise will be dominated by the acceleration induced position fluctuations:

$$\widetilde{\delta x}(f) = 40 \cdot 10^{-12} \times \left[1 + \left(\frac{1\,\mathrm{mHz}}{f} \right)^2 \right] \frac{\mathrm{m}}{\sqrt{\mathrm{Hz}}}. \tag{1.2}$$

Equivalently the acceleration requirement for the drag-free control of the test masses can be relaxed at high frequencies, as the interferometer noise will limit the detector sensitivity:

$$\widetilde{\delta a}(f) = 3 \cdot 10^{-15} \times \left[1 + \left(\frac{f}{1\,\mathrm{mHz}} \right)^2 \right] \frac{\mathrm{m} \cdot \mathrm{s}^2}{\sqrt{\mathrm{Hz}}}. \tag{1.3}$$

Figure 1.3 shows the graphical representation of Equations (1.2) and (1.3). These performance values were assumed for the sensitivity presented in Figure 1.2. Also shown in Figure 1.3 are the requirements for acceleration and pathlength noise for the technology demonstration mission LISA Pathfinder, that will be discussed in Chapter 2. The performance to be demonstrated by LISA Pathfinder is relaxed a factor of ten with respect to LISA.
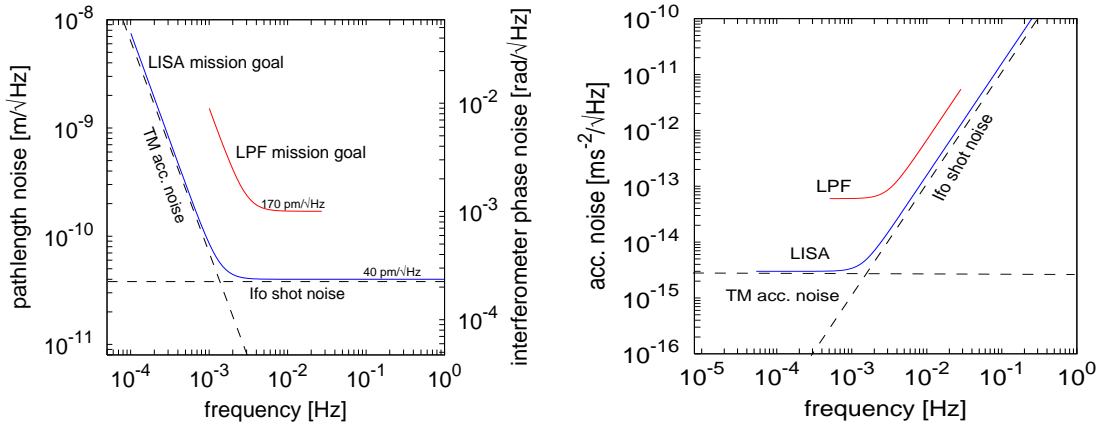
Figure 1.3: Left: requirement for the interferometer sensitivity to pathlength fluctuations. Right: residual acceleration noise of the test masses to be achieved by the drag-free control system. The requirements for the technology demonstration mission LISA Pathfinder, relaxed with respect to LISA in one order of magnitude, are also presented. LISA Pathfinder (LPF) is discussed in Chapter 2.

1.3. Interferometric conceptual design

As explained in Section 1.1, the basic measurement of the LISA interferometry is one LISA arm. The actual implementation of the interferometry for one arm will splits the measurement in three parts, as shown schematically in Figure 1.4: the position of the local test mass with respect to the optical bench d_1, the distance between the local and the remote optical bench d_{12}, and the position between the remote test mass and the remote optical bench d_2.

This way, the technical difficulties are separated: the interferometry between the satellites does not contain any free floating test masses.
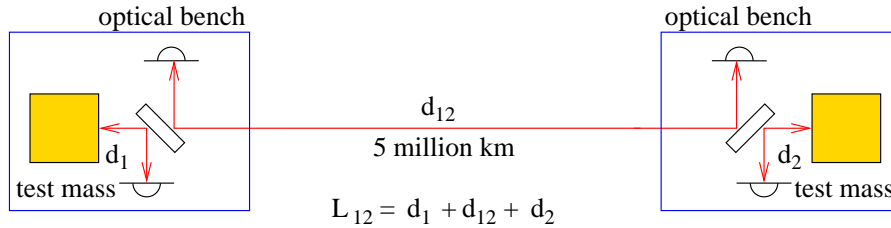
Figure 1.4: LISA arm split into three parts.

1.4. Technology demonstration: LISA Pathfinder

Several technical challenges have to be met to achieve the sensitivity requirements explained in Section 1.2:

Drag free control system: it must keep the residual acceleration of each test mass below $3 \times 10^{-15} \mathrm{ms}^{-2}/\sqrt{\mathrm{Hz}}$ at 3 mHz.

Interferometry: its sensitivity has to be better than $40 \times 10^{-12} \mathrm{m}/\sqrt{\mathrm{Hz}}$ at 3 mHz.

Micronewton Thrusters: they must provide with very low noise the continuous forces of micronewton magnitude that are necessary for the drag-free operation.

The in-flight test for LISA to be presented in Chapter 2, LISA Pathfinder, is designed to test these technologies and it will be practically test the implementation of the local interferometry.

Although the necessary technology for the remote interferometry will also profit from some elements in the Pathfinder design, most of its elements have to be tested separately on ground.

Chapter 2.

Interferometry on-board LISA Pathfinder

LISA Pathfinder is a technology demonstration mission for LISA consisting of two LISA-like test masses in a single satellite. As in LISA, these test masses will be kept drag-free and an interferometer will monitor their position fluctuations with picometre precision. In this sense, LISA Pathfinder can be regarded as a single LISA arm scaled down to 30 cm and enclosed in one satellite. Its implementation phase has already begun and launch is presently scheduled for 2009.

This chapter presents the interferometry design for the European payload on-board LISA Pathfinder, the LISA Technology Package (LTP). The LTP interferometry has been tested in the laboratory using the engineering model of the LTP optical bench and dummy mirrors acting as test masses. We present this experimental setup and the achieved interferometric sensitivity, which fulfils the required sensitivity.

2.1. Introduction: LISA Pathfinder and the LISA technology package

LISA Pathfinder (LPF) will carry two different payloads: the European LISA technology package (LTP) and the NASA provided Disturbance Reduction System (DRS). This chapter will concentrate on the LTP experiment [15, 16, 17, 3, 14] .

Figure 2.1 shows the orbit of the LISA Pathfinder satellite. After several apogee raising manoeuvres and an injection manoeuvre, the final orbit will be a Lissajous orbit around L1, the first Sun-Earth Lagrange point [18].

A CAD drawing of the LPF satellite can be seen on the left side of Figure 2.2. Several panels of the outer compartments, mostly occupied by electronics, have been omitted to show more clearly the cylindrical structure in the centre that contains the LTP core assembly (LCA), which is the main hardware of the LTP experiment. The satellite structure has already been manufactured and is shown in the right part of Figure 2.2. It is made out of thermally and mechanically stable Carbon Fibre Reinforced Plastic (CFRP), and constitutes a double layer isolation to achieve a highly stable environment for the most sensitive payload, the LCA.
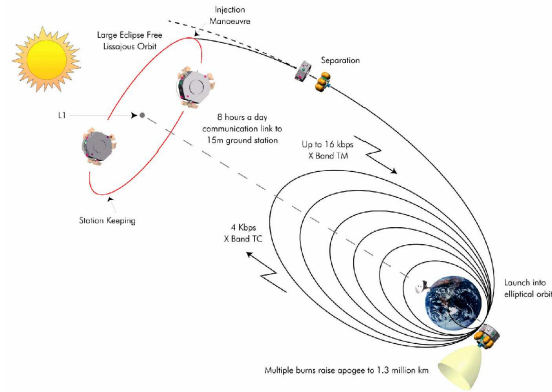
Figure 2.1: LISA Pathfinder will orbit the first Lagrange point (source: ESA official LPF website [3]).
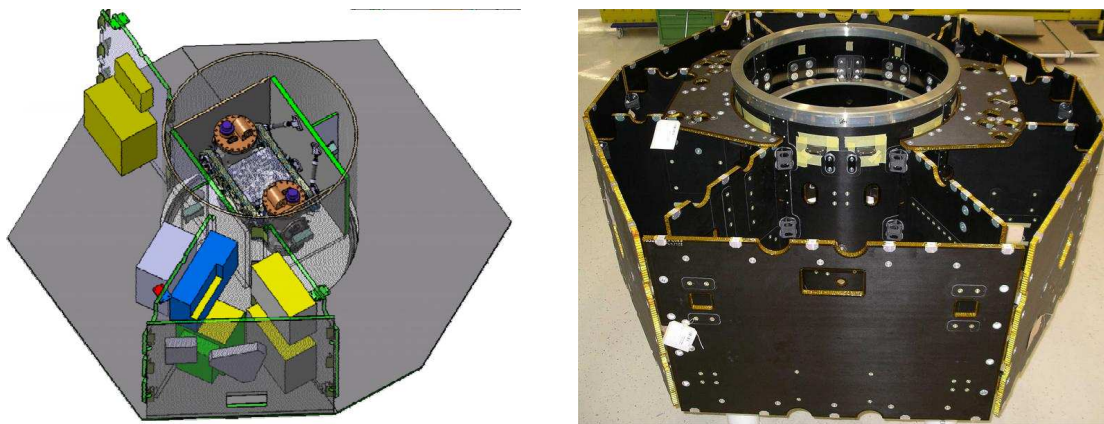
Figure 2.2: Left: CAD view of the LISA Pathfinder satellite with the LTP core assembly in the centre (source EADS Astrium). Several panels of the satellite structure are omitted for simplicity. Right: flight model of the satellite structure entirely made of Carbon Fibre Reinforced Plastic (CFRP) sandwich panels (source: ESA official LPF website [3]).

A detailed view of the LCA is shown in Figure 2.3(a): it consists of two free floating LISA-like test masses (TM) whose relative motion along a common sensitive axis is measured with a laser interferometer. Each test mass is enclosed in its own cylindrical vacuum tank. Between the vacuum tanks there is an ultra-stable optical bench made of Zerodur [19] and the whole structure is stably held together by two side plates also made out of Zerodur. Figure 2.3(b) consists of a sectional view of the LCA showing the laser interferometry on top of the optical bench. The position fluctuations of the test masses are measured with laser beams that are directed from the optical bench into each vacuum tank through an optical window and reflected back from the test masses to the optical bench. This concept of using the test masses as mirrors of the interferometer is more clearly shown in Figure 2.3(c), where the vacuum tanks have been omitted for clarity. Finally, Figure 2.3(d) shows the engineering model (EM) of the optical bench, where the test masses

have been replaced by dummy mirrors to test the LTP interferometry on ground.
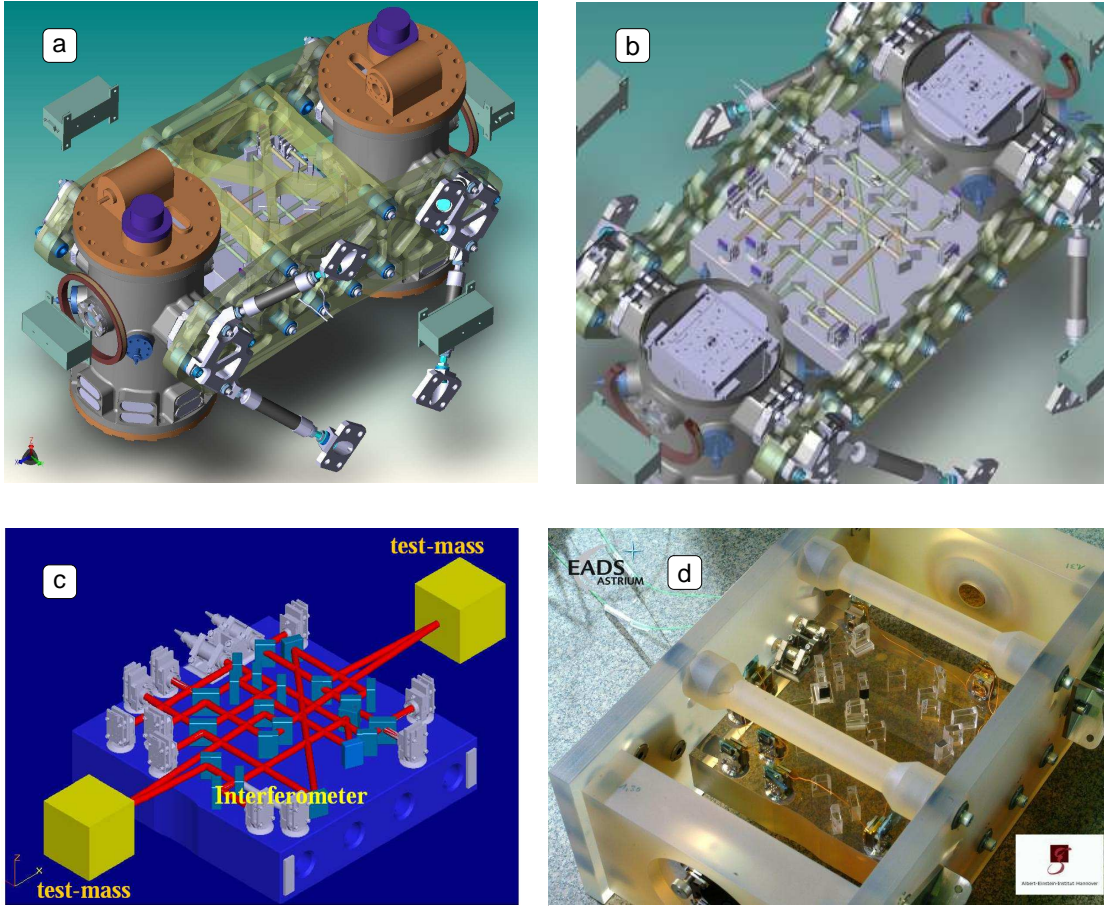
Figure 2.3: The LTP core assembly (LCA). a: CAD drawing showing two vacuum enclosures for the test masses, the optical bench between them and the side slabs holding the structure together. b: sectional view of the LCA showing the interferometry on top of the optical bench. c: the conceptual view of the LCA showing the test masses as mirrors part of the interferometer and omitting the vacuum tanks. d: engineering model of the optical bench. The test masses have been substituted by gold-coated mirrors for ground testing. Source: EADS Astrium.

The main goal of the mission is the demonstration of geodesic motion of the test masses. To this end, they will be kept free-falling using a drag-free attitude control system (DFACS), a set of control laws for the stabilisation of the different degrees of freedom of the satellite and the test masses. The target level of residual acceleration noise for the test masses in the sensitive axes is one order of magnitude relaxed compared to LISA, as shown in Figure 1.3, and can be written as:

$$\widetilde{\delta a}(f) = 3 \cdot 10^{-14} \times \left[1 + \left(\frac{f}{3\,\mathrm{mHz}} \right)^2 \right] \frac{\mathrm{m}}{\mathrm{s}^2\,\sqrt{\mathrm{Hz}}}. \tag{2.1}$$

As error signal for the DFACS, the position fluctuations of the free floating test masses in the sensitive axis (called x-axis) will be measured with the interferometer, as shown in Figure 2.3. This way, high precision interferometry in space will be also demonstrated by LISA Pathfinder.

In the other axes, the position fluctuations of the test masses with respect to the satellite will be determined by a set of electrodes that surround them [16, 14], shown in Figure 2.4. These electrodes will also be used by DFACS for capacitive actuation of the test mass position. In the sensitive, "drag-free" coordinates, the actuation will be done on the satellite instead of the test mass. The position of the satellite will be actuated with micronewton thrusters that are attached to its outer structure. The micronewton thrusters, together with the DFACS and the space interferometry constitute the three LISA core technologies (see Section 1.4) that LPF will demonstrate in space.

Several control modes are foreseen for the DFACS in order to extract the largest possible amount of information of the interaction between the three LISA technologies on-board LPF [17]. In the nominal operation mode, the eighteen degrees of freedom of the satellite and the two test masses are separated into "drag-free" coordinates —measured by the interferometer and actuated by the micronewton thrusters—, and the "suspension coordinates" for which the capacitive electrodes are used [16]. The full integration in space of the three technologies in one real-time control loop with the required precision makes the output of the Pathfinder so valuable for LISA.
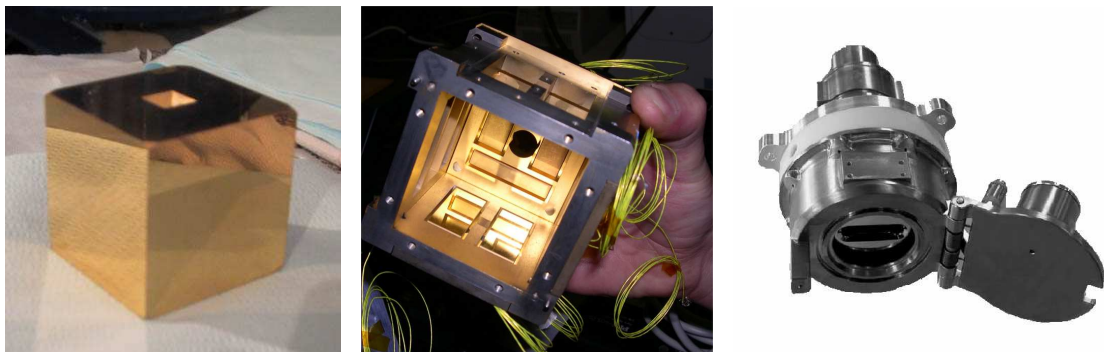
Figure 2.4: From left to right: cubic test mass with four cm side made of a gold-platinum alloy to minimise its magnetic susceptibility. Test mass electrode housing, showing the hole for the laser beam. Micro-Newton thruster based on Field emission electric propulsion (FEEP) technology using liquid caesium (source: ESA official LPF website [3]).

2.2. Requirements for the LTP interferometry

The pathlength sensitivity required for LTP interferometry [20] is set at $170\,\mathrm{pm}/\sqrt{\mathrm{Hz}}$, as shown in Figure 2.5. It follows the relaxation by a factor of ten with respect to LISA in frequency and sensitivity that was already mentioned for the acceleration noise requirement from Equation (2.1). The interferometric sensing must be able to monitor

the test mass position along the sensitive axis with a pathlength sensitivity twenty times
more stringent:

$$\widetilde{\delta x}(f) = 9 \cdot 10^{-12} \times \left[1 + \left(\frac{3\,\text{mHz}}{f} \right)^2 \right] \frac{\text{m}}{\sqrt{\text{Hz}}}. \tag{2.2}$$

This sensitivity goal for the interferometry is also shown in Figure 2.5, together with the
LISA sensitivity of $40\,\text{pm}/\sqrt{\text{Hz}}$ and the allocation of $1\,\text{pm}/\sqrt{\text{Hz}}$ for each interferometric
noise source.
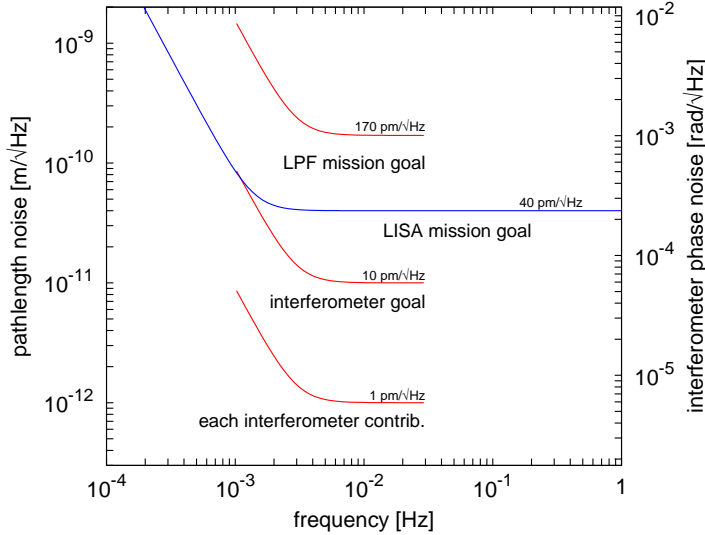
Figure 2.5: Required sensitivity for the LTP interferometry: at $3\,\text{mHz}$, $170\,\text{pm}/\sqrt{\text{Hz}}$ are allocated
for the total pathlength noise of the test masses, $10\,\text{pm}/\sqrt{\text{Hz}}$ for the interferometry and $1\,\text{pm}/\sqrt{\text{Hz}}$
for each contribution from the interferometer.

Apart from the required sensitivity, the interferometer must be capable of tracking the
drifts of the test masses that will occur below the LTP measurement band and that
can go over hundreds of microns. The interferometer must also be capable of delivering
angular alignment sensitivity for the test masses with $10\,\text{nrad}/\sqrt{\text{Hz}}$ at $3\,\text{mHz}$. All the
requirements regarding sensitivity are valid between 3 and $30\,\text{mHz}$, relaxing as $1/f^2$
towards low frequencies, as shown in Figure 2.5.

2.3. Interferometry design for LTP

After a technology study, a set of four non-polarising heterodyne Mach-Zehnder interfer-
ometers was chosen as design for the LTP interferometry [20, 21].

The principle of operation of the heterodyne Mach-Zehnder interferometer for LTP is
shown in Figure 2.6: a laser is split in two paths and each of them is shifted in its
frequency by a different amount with an acousto-optic modulator (AOM) before they are

recombined on a photodiode. The output photocurrent is given by a beat note signal at the frequency difference between the two interfering beams, the heterodyne frequency f_{het}, and can be written as [22, 23, 24]

$$I(t) = A(1 - c\,\cos(2\,\pi\,f_{\text{het}}\,t + \varphi_{\text{int}}(t))). \tag{2.3}$$

where I is the measured photocurrent, A the average photocurrent of the heterodyne signal, c the interferometric contrast and f_{het} the heterodyne frequency, which is chosen to be in the range of 1 to 5 kHz for LTP.
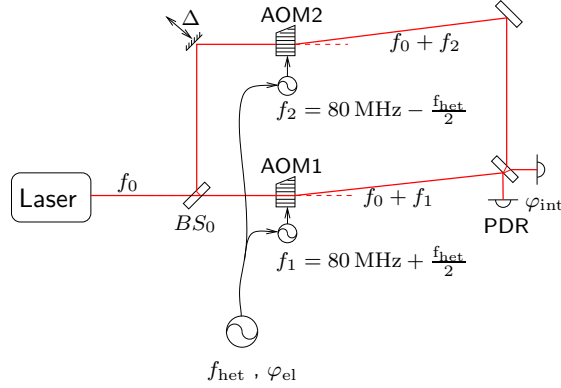
Figure 2.6: Basic schematic setup of a heterodyne Mach-Zehnder interferometer: any movement Δ of the optical components in the arms is detected as a change in the interferometric phase of the heterodyne signal φ_{int}.

The interferometric phase φ_{int} is given by

$$\varphi_{\text{int}} = \frac{2\pi}{\lambda}(L_1 - L_2) \tag{2.4}$$

where λ is the laser wavelength and L_1 and L_2 are the length of the interferometer arms, i.e. the optical path of each beam between the first and the second beam splitter. Any movement Δ of the optical components in the arms will cause a change in the armlength and thus in the interferometric phase φ_{int}.

This kind of interferometer will be used in LTP with a free floating test mass as mirror to derive its displacement fluctuations from the measurement of the interferometric phase φ_{int}, as shown schematically in picture c in Figure 2.3. A millirad change in the phase of the 1 kHz heterodyne signal corresponds to a position change of the test mass in the sub-nanometre range.

The sensitivity limitation of this interferometer is given by the position fluctuations of the other optical components, which have to be in the picometre range to achieve the $10\,\text{pm}/\sqrt{\text{Hz}}$ requirement shown in Figure 2.5. This is not feasible for components such as the AOMs, and in order to cope with this impediment the actual LTP interferometric design includes more than one interferometer, as explained below.

Figure 2.7 shows a more realistic scheme of the actual LTP interferometry. It is split in two parts:

- the modulation bench, containing the unstable components such as AOMs, the first beam splitter BS_0 and optical fibres
- the optical bench (OB), which contains the recombination part of the interferometry and the photodiodes. It is made of a Zerodur base plate with fused silica optical components bonded on top of it via the so-called "hydroxide catalysis bonding [25, 26, 27]". This construction technique allows a monolithic design that makes it very stable regarding mechanical and thermal disturbances [19].

On the optical bench, the two frequency shifted beams are split again and recombined at two different beam splitters, forming two different interferometers: a "reference (R)" interferometer and a "measurement (M)" interferometer.
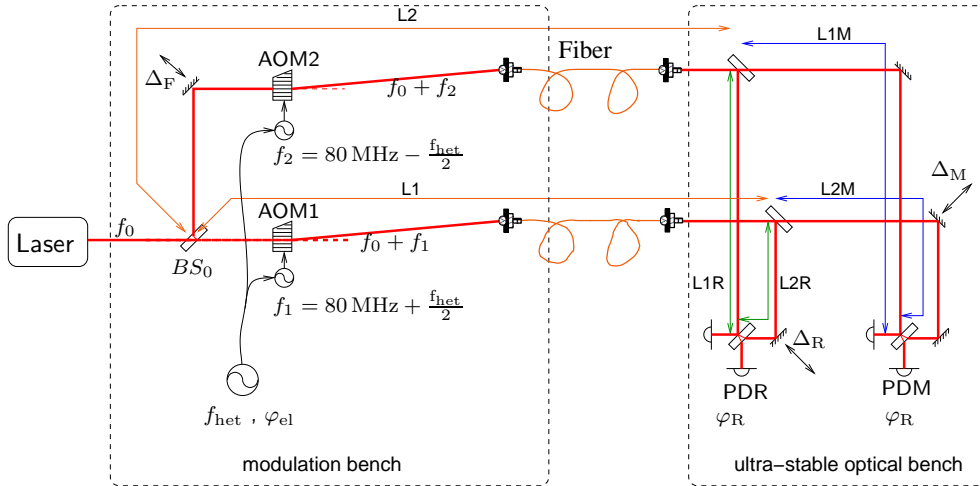
Figure 2.7: Scheme of the setup used for the LTP interferometry, where two heterodyne Mach-Zehnder interferometers have a first common unstable part and second stable part specific to each one. The subtraction of the output phases $\varphi_R - \varphi_M$ cancels the common-mode pathlength fluctuations from the unstable part.

Following the optical paths shown in Figure 2.7, the phase of the reference and measurement interferometers φ_R and φ_M can be written as:

$$\varphi_R = \frac{2\pi}{\lambda}(L_1 - L_2 + L_{1R} - L_{2R}) = \Delta_F + \Delta_R \tag{2.5}$$

$$\varphi_M = \frac{2\pi}{\lambda}(L_1 - L_2 + L_{1M} - L_{2M}) = \Delta_F + \Delta_M \tag{2.6}$$

where Δ_F represents the large pathlength variations present in both interferometers (common-mode), caused by the unstable parts of the modulation bench and the optical fibres. The pathlength variations specific to each interferometer Δ_R and Δ_M occur on the stable optical bench and are thus much smaller than Δ_F. The main interferometric measurement of LTP consists of the subtraction between φ_R and φ_M

$$\varphi_M - \varphi_R = \Delta_M - \Delta_R, \tag{2.7}$$

as this cancels the common fluctuations Δ_F and leaves only the small position fluctuations

of the components on the ultra-stable optical bench as ultimate sensitivity limitation for the LTP interferometry [20, 21].

As the LTP interferometry has to measure the position fluctuations of two test masses, there are two measurement interferometers on the LTP optical bench, as shown in Figure 2.8. The interferometer on the left part of Figure 2.8 is the "X1" interferometer, with output phase φ_1. It measures the position fluctuations of test mass 1 (TM1) with respect to the optical bench in the sensitive axis x. The interferometer on the right side of Figure 2.8 is the "X12" interferometer, with output phase φ_{12} . It measures the relative position fluctuations of both test masses with respect to the optical bench.
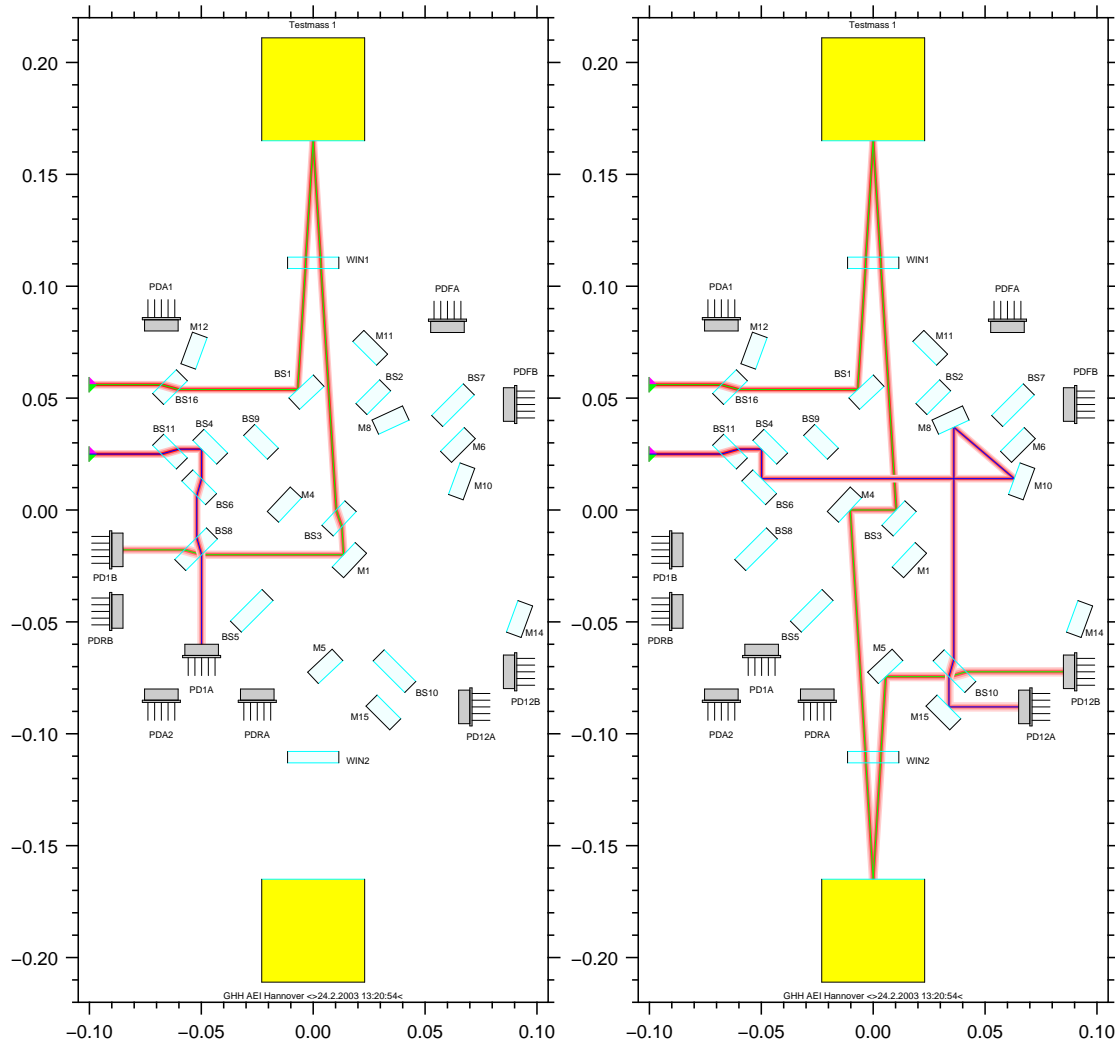
Figure 2.8: Optical layout of the measurement interferometers X1 and X12 on the optical bench. The pathlength difference between both beams are zero in both interferometers, when an extra pathlength of 356.7 mm difference between the fibres that bring the light from the modulation bench (not drawn) is included.

However, there are other noise sources, such as the laser amplitude[1] and frequency noise, that limit the interferometer sensitivity unless they are stabilised. Frequency noise $\delta\nu$ couples in the interferometric phase φ_{int} due to the armlength mismatch $\Delta L = L_1 - L_2$ as can be seen from Equation (2.8):

$$\varphi_{\text{int}} = \frac{2\pi}{\lambda}(L_1 - L_2) = \frac{2\pi\nu}{c}\Delta L \quad \Rightarrow \quad \delta\varphi_{\text{int}} = \frac{2\pi\delta\nu}{c}\Delta L. \tag{2.8}$$

The strategy foreseen in LTP to suppress the laser frequency noise consists in a supplementary interferometer on the optical bench with an intentional armlength mismatch of 38 cm, called the "frequency" interferometer, that can be seen on the right side of Figure 2.9. Its output phase φ_{F} is used as sensor for the laser frequency noise in a frequency stabilisation that will be explained in detail in Chapter 5. The left part of Figure 2.9 shows the reference interferometer, with output phase φ_{R}.

Note that the 38 cm intentional armlength mismatch for the frequency interferometer is implemented with the optical fibres between the modulation bench and the optical bench. This explains that the layouts of the X1,X12 and reference interferometers in Figures 2.8 and 2.9 have a pathlength mismatch that is compensated by the fibres, while the frequency interferometer has nearly equal armlength on the optical bench and a total armlength mismatch of 38 cm, due to the not shown fibres.

The laser amplitude noise couples also directly in the phase readout [28, 22], so that single element photodiodes are foreseen on the optical bench to measure the laser power of each beam independently. The implementation of the amplitude stabilisation using these photodiodes will be described in detail in Chapter 5. They are called PDA1 and PDA2, as shown in Figure 2.10, which summarises the function of all the optical bench components.[2] Each interferometer output is recorded with two redundant quadrant photodiodes (QPD), which obtain alignment information in addition to the longitudinal phase φ. Each QPD is labelled "PDxA" and "PDxB" with x being the abbreviation for each interferometer (1, 12, R or F). The beam that is reflected off the test masses is labelled as "measurement beam (MB)", and the beam that always remains on the optical bench is the "reference beam (RB)".

2.4. Readout of longitudinal phase and alignment signals

In order to extract the phase from the heterodyne signal, a phase readout procedure has been designed [28, 21], based on a Single Bin Discrete Fourier Transform (SBDFT). The procedure consists of three stages, the first two of which are realised independently for each of the 32 channels from the eight QPD:

---

[1]The widely spread terminology "amplitude noise" is used in this work, although strictly speaking only the laser power is measurable. The amplitude is the square root of the power.

[2]The layouts presented here correspond to the engineering model of the LTP optical bench, which was extensively used in the investigations presented in this work. The layouts foreseen for the flight model [27, 29] present some design improvements, but the relevant features presented here remain unchanged.
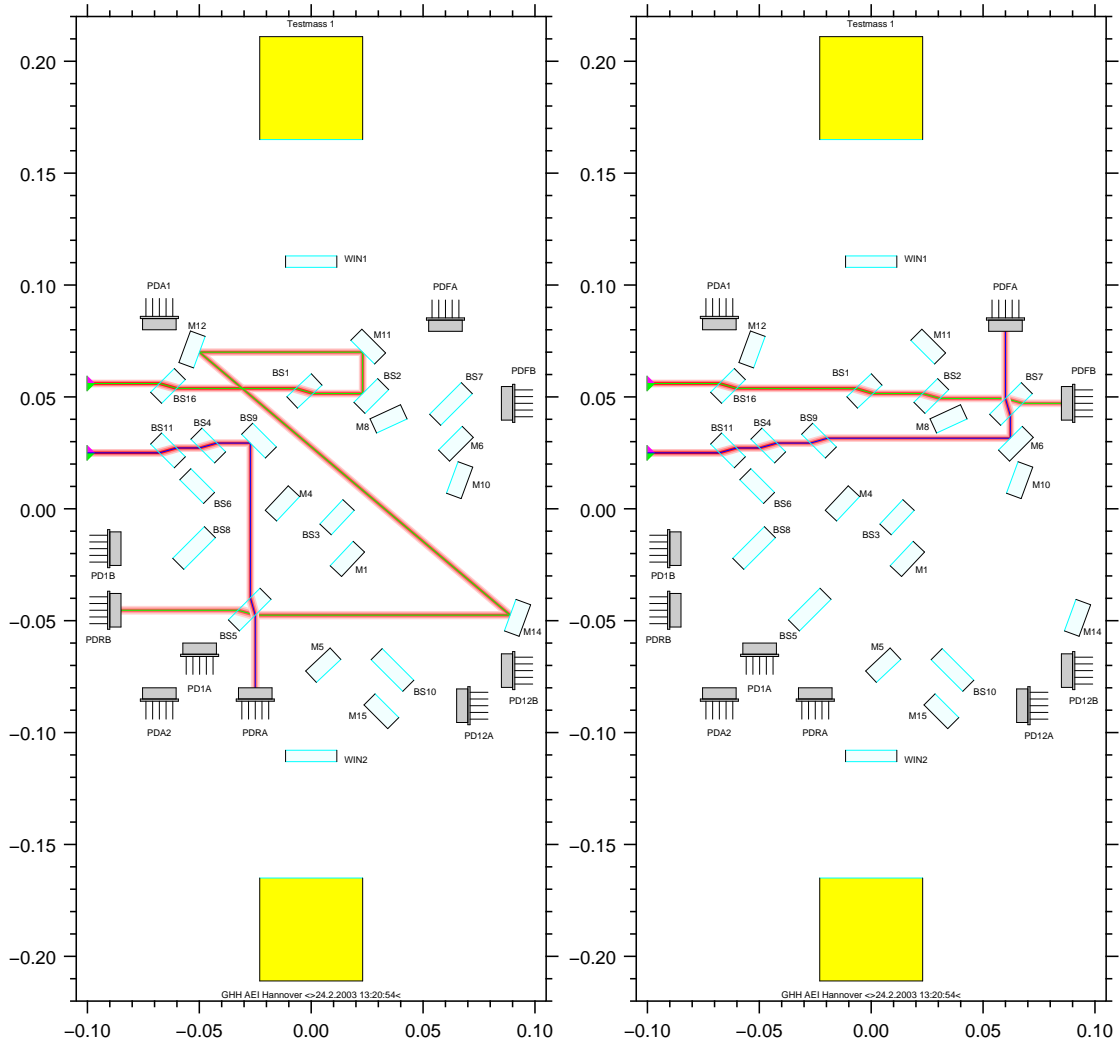
Figure 2.9: Optical layout of the reference and frequency interferometer on the optical bench. The pathlength difference between both beams are zero in the reference interferometer (left), when an extra pathlength difference of 356.7 mm between the fibres that bring the light from the modulation bench (not drawn) is included. The pathlength difference in the frequency interferometer (right) is then 380 mm.
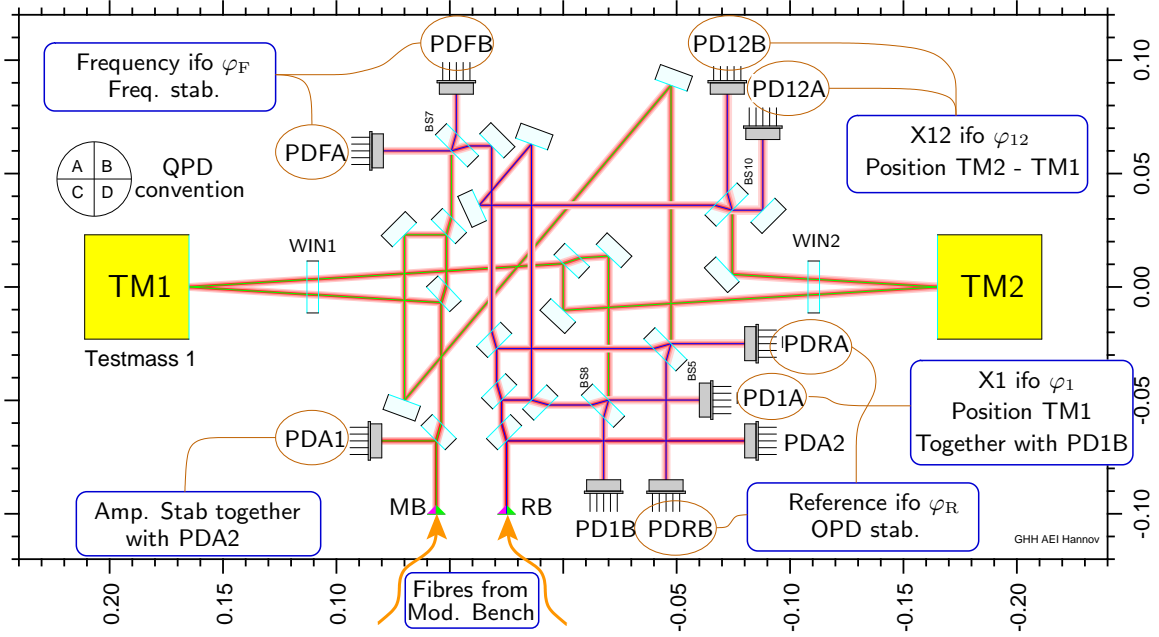
Figure 2.10: Scheme of the optical bench with all four interferometer layouts. The function and labelling of the different interferometer outputs is also explained.

Preamplifiers and A/D conversion: The photocurrent is converted into a voltage with a transimpedance preamplifier, sent through a low-pass filter to avoid aliasing and digitised at a sample rate $f_{\mathrm{samp}} = 50$ to $100\,\mathrm{kHz}$. This results in a time series $x_{\mathrm{i}}(t_{\mathrm{i}})$.

SBDFT: It consists of a Fourier transformation for only one frequency: only one Fourier result —also called bin— corresponding to the heterodyne frequency is calculated. The result is the complex amplitude of the photodiode signal at the frequency f_{het},

$$F(\mathrm{f}_{\mathrm{het}}) = A_{\mathrm{v}} \, \exp^{\mathrm{j}\varphi} \tag{2.9}$$

where A_{v} is the voltage amplitude of the heterodyne signal as measured by the photodiode preamplifier. One value of $F(\mathrm{f}_{\mathrm{het}})$ is obtained from N samples of $x_{\mathrm{i}}(t_{\mathrm{i}})$ as

$$\Re\{F(f_{\mathrm{het}})\} = \frac{1}{N} \sum_{i=0}^{N-1} x_{\mathrm{i}}(t_{\mathrm{i}}) \cdot \cos\left(2\pi f_{\mathrm{het}} \frac{i}{f_{\mathrm{samp}}}\right), \tag{2.10}$$

and

$$\Im\{F(f_{\mathrm{het}})\} = \frac{1}{N} \sum_{i=0}^{N-1} x_{\mathrm{i}}(t_{\mathrm{i}}) \cdot \sin\left(2\pi f_{\mathrm{het}} \frac{i}{f_{\mathrm{samp}}}\right). \tag{2.11}$$

Besides, the DC mean value of the signal is calculated as

$$DC = \frac{1}{N} \sum_{i=0}^{N-1} x_{\mathrm{i}}(t_{\mathrm{i}}). \tag{2.12}$$

19

These stages are implemented in a dedicated hardware phasemeter based on FPGA[3] chips. This way, a considerable data reduction is achieved before the next processing stage in the data management unit (DMU).

Phasemeter back-end processing: The previous results are obtained for each of the 32 quadrants. For each QPD (there are two redundant QPD for each interferometer reference, frequency, X1, and X12), the signals of the quadrants A, B, C and D (see convention in Figure 2.10) are combined to obtain the longitudinal phase and alignment signals of the different interferometers:

The longitudinal phase φ is obtained from the previous results as

$$\varphi = \arg(F_\Sigma) + n\,2\pi \quad \text{with} \qquad F_\Sigma = F_A + F_B + F_C + F_D, \tag{2.13}$$

where the term $n\,2\pi$ comes from a phasetracking algorithm [21] that removes jumps in the obtained phase time series by appropriately adding an integer number of 2π. These longitudinal phases build the base for the main interferometric results, the displacements of test mass 1 along the sensitive axis

$$\delta x_1 = \frac{1}{2}\delta(\varphi_1 - \varphi_R)\frac{\lambda}{2\pi} \tag{2.14}$$

and the displacement of test mass 2 with respect to test mass 1

$$\delta x_{12} = \frac{1}{2}\delta(\varphi_{12} - \varphi_R)\frac{\lambda}{2\pi}, \tag{2.15}$$

where the extra factor $1/2$ with respect to Equation (2.4) comes from the quasi-normal reflection of the laser beam on the test mass.

Furthermore, alignment signals are also obtained from the phasemeter results. Using the so-called "differential wavefront sensing" (DWS) technique [30], the relative angle between the wavefront of the beams impinging on the photodiode can be obtained in the horizontal plane as

$$DWS^\phi = \arg\left(\frac{F_A + F_C}{F_B + F_D}\right), \tag{2.16}$$

i.e. by evaluating the phase difference between the heterodyne signal on the left side of the QPD and the heterodyne signal on the right side of the QPD. Equivalently, for the vertical plane

$$DWS^\eta = \arg\left(\frac{F_A + F_B}{F_C + F_D}\right). \tag{2.17}$$

The DWS signals deliver very sensitive information about angular fluctuations of the test masses, as these cause angular misalignment between the interfering beams. Let ϕ_1 and η_1 be the misalignment of TM1 in x and y directions, respectively, and ϕ_2 and η_2 similarly for TM2. These angles are referred to the nominal TM orientation when all DWS results are zero.

---

[3]Field Programmable Gate Array

The DWS alignment signals will then be

$$DWS_1^\phi = k_1 \cdot \phi_1, \tag{2.18}$$

$$DWS_1^\eta = k_2 \cdot \eta_1, \tag{2.19}$$

$$DWS_{12}^\phi = k_3 \cdot \phi_1 + k_4 \cdot \phi_2, \tag{2.20}$$

$$DWS_{12}^\eta = k_5 \cdot \eta_1 + k_6 \cdot \eta_2. \tag{2.21}$$

The typical value for the constants k_1 to k_6, which convert DWS angles (in radians) in test mass angles (also in radians) is about $5000\,\text{rad/rad}$ [31]. The only disadvantage of the DWS alignment is its reduced dynamic range of about $200\,\mu\text{rad}$ [31], as there has to be interference between the two beams that results in measurable heterodyne amplitude for the calculations in Equations (2.16) and (2.17).

This limitation of the DWS alignment can be overcome by the DC alignment signals. They consist of the subtraction of the mean laser power impinging on one half of the photodiode minus the power impinging on the other, normalised by the total power on the QPD, so that the results ranges from 0 to 1. The horizontal alignment is calculated as

$$DC^\phi = \frac{(DC_\mathrm{A} + DC_\mathrm{C}) - (DC_\mathrm{B} + DC_\mathrm{D})}{\Sigma}, \tag{2.22}$$

with

$$\Sigma = DC_\mathrm{A} + DC_\mathrm{C} + DC_\mathrm{B} + DC_\mathrm{D}. \tag{2.23}$$

And equivalently for the vertical plane

$$DC^\phi = \frac{(DC_\mathrm{A} + DC_\mathrm{B}) - (DC_\mathrm{C} + DC_\mathrm{D})}{\Sigma}. \tag{2.24}$$

The DC alignment signals are about ten times less sensitive than the DWS signals, but they work as soon as any amount of light is impinging on the photodiode, what makes them very useful for the initial alignment of the test masses with respect to the interferometer, as explained in Chapter 3.

Finally, the interference contrast of each interferometer is calculated as

$$c = \frac{F_\Sigma}{\Sigma}. \tag{2.25}$$

2.5. Laboratory implementation

In order to test the principle of operation and sensitivity of the LTP interferometry discussed above, prototypes of the different subsystems have been setup to mimic the LTP configuration as closely as possible. This section presents the experimental setup that has been used in most of the LTP-related investigations presented in this work and some variations that have been introduced during different investigations campaigns.

2.5.1. Experimental setup

The components of the LTP interferometry are summarised in Figure 2.11. The laser
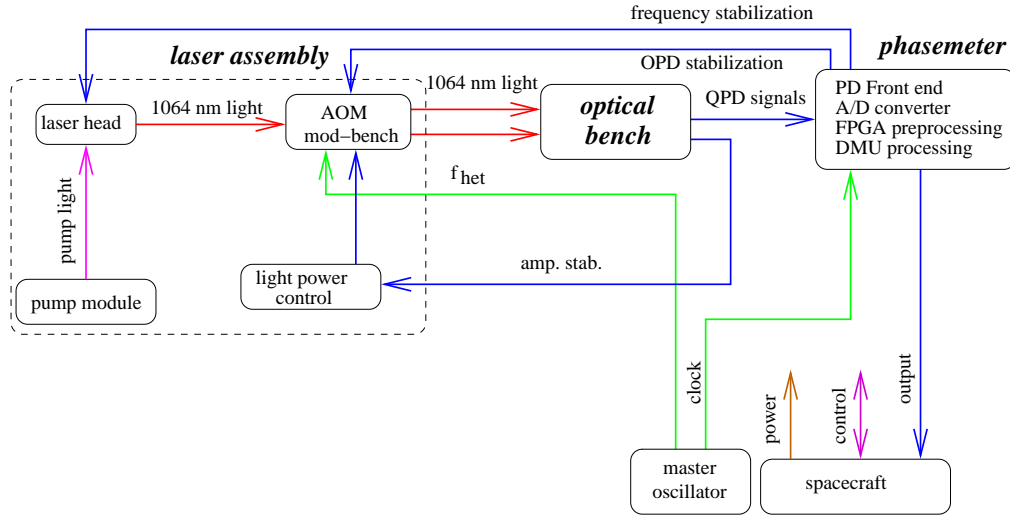
Figure 2.11: Scheme of the different subsystems of the LTP interferometry.

head and pump module that was used for most of the tests, unless otherwise noted, was an Innolight Mephisto 500 [32], a commercial NPRO laser at $\lambda = 1064\,\text{nm}$. The Tesat laser "Smart2 engineering model breadboard[4]", an engineering model of the laser to be used on LTP with $25\,\text{mW}$ output power was also characterised and it met all the requirements for the LTP interferometry, what practically qualified it as a valid master for a master oscillator power amplifier laser system for LISA. Its free-running frequency noise will be used as example in this work for the frequency stabilisation of LTP (Chapter 5, Figure 5.9) and LISA (Chapter 6, Figure 6.1). It can be seen in Figure 2.12.

Also a prototype of the LTP modulation bench made by Contraves was characterised with the setup presented here and is shown in Figure 2.12, but most of the measurements presented in this work were performed with the breadboard implementation of the modulation bench shown in Figure 2.13.

The laboratory implementation of the laser and modulation bench can be seen in the left part of Figure 2.13. Apart from the Mephisto laser, the used free-beam AOMs were $2\,\text{mm}$ aperture models from Isomet (1205C-2) operating nominally at 80MHz and $2\,\text{Watt}$ RF power. There were also several discrete optic components, in particular a PZT-mounted mirror that allowed to control the optical pathlength difference of the beams on the modulation bench. Finally, two single mode polarisation maintaining optical fibres inject the frequency shifted beams onto the optical bench inside the vacuum tank, shown in the right part of Figure 2.13. It is the engineering model of the LTP optical bench. This optical bench was manufactured at the Rutherford Appleton Laboratory

---

[4]The actual LISA Pathfinder Mission was previously called Smart2
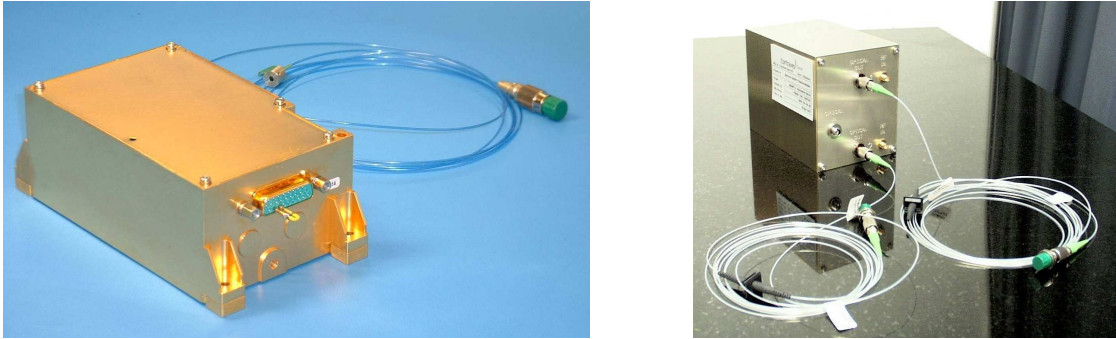
Figure 2.12: Left: Engineering model breadboard laser of Tesat for the LTP interferometry. Right: prototype of the modulation bench made by Contraves.

(RAL) with scientific support from IGR[5], AEI, University of Birmingham and integrated by Astrium Germany, thus representing the successful international collaboration of the LTP team. Its interferometric functionality and performance was tested in the frame of an extensive environmental test campaign [28, 33, 34]. Since then it has been used at the AEI laboratory facilities.
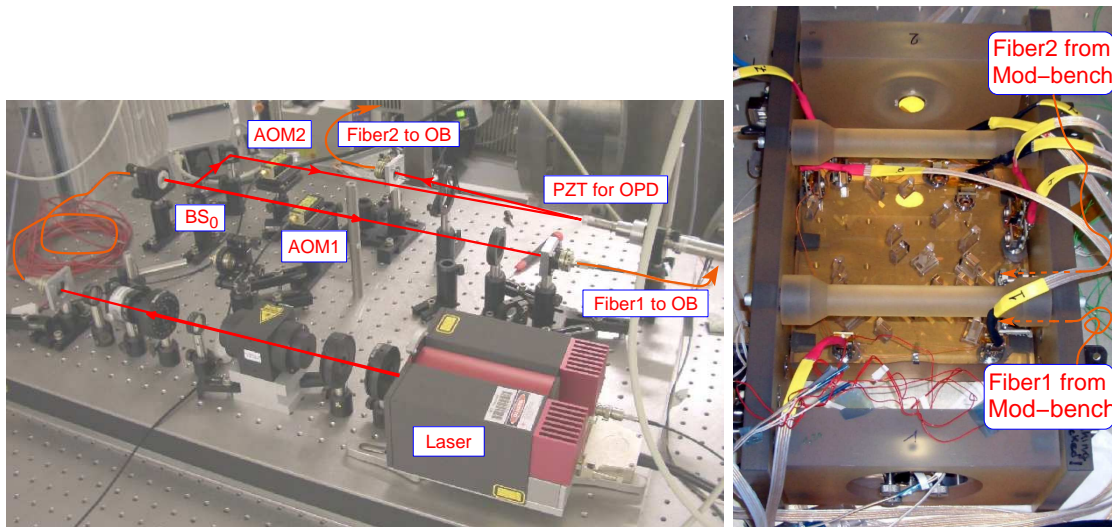
Figure 2.13: Left: Modulation bench of the present laboratory implementation of the LTP interferometry at the AEI. Right: OB in the vacuum tank.

The main difference between this setup and the real LTP interferometry lies in the test masses, which have been substituted for testing purposes by two gold coated mirrors, as can be seen in Figure 2.13 and 2.3. These movable dummy mirrors represent a possible cause for temperature driven pathlength noise at low frequencies, as they are not bonded to the optical bench (OB) but supported with metallic mounts. To keep temperature fluctuations as low as possible at the optical bench, it was kept inside a vacuum

---

[5]The Institute for Gravitational Research in Glasgow

tank and a laboratory ventilation system with a long-term temperature regulation was used, in opposition to "fast" air-conditioning systems that have shown worse performance. This allowed a temperature stability of $10^{-4}\,\mathrm{K}/\sqrt{\mathrm{Hz}}$ on the optical bench, as shown in Figure 7.23.

The phasemeter prototype used resembles the FPGA-based design for LTP [28, 21]. The parameters of the front-end electronics (18 bits A/D converters at 800 kHz) have been designed for higher precision than the LTP phasemeter, in order not to limit the interferometric performance unnecessarily and thus be able to make debugging tests of the other elements of the setup. The sensitivity of this "pm3" phasemeter, which is well below the specifications, is shown in Figure 2.14 together with a picture of the hardware implementation.
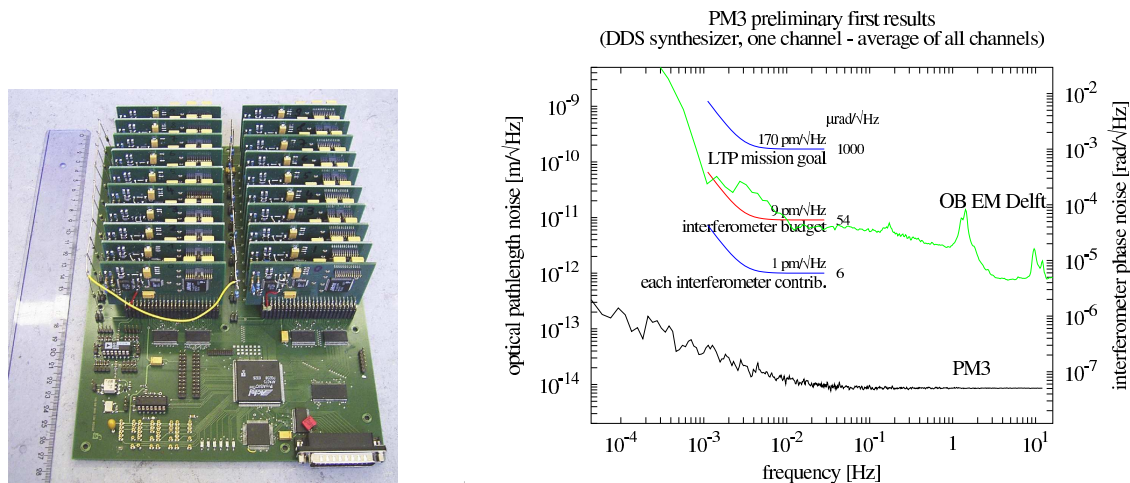
Figure 2.14: Phasemeter "pm3". Hardware implementation on the left, with 20 input channels. Its performance, well below the requirements is shown on the right part of the Figure.

The back-end calculations to obtain the alignment signals and longitudinal phases described in Section 2.4 are performed in a laboratory PC with dedicated software.

2.5.2. Initial performance: "small vector" noise

Figure 2.15 shows a typical time series of the main interferometric measurement $\varphi_1 - \varphi_{\mathrm{R}}$ over 4000 s, measured with the setup presented in Section 2.5.1. A linear drift of the phase, corresponding to long term thermal pathlength fluctuations of the metallic mounts of the dummy mirrors has been subtracted. The general notation φ_{M} will be used to refer to any measurement phases φ_1 or φ_{12}.

The residual phase noise in a time scale of 1000 seconds was several millirad, and was given by slow pathlength fluctuations on the optical bench. But for any given short time-segment, there is some excess noise that made the measured phase fluctuate between two defined values with an amplitude of approximately 1 mrad.
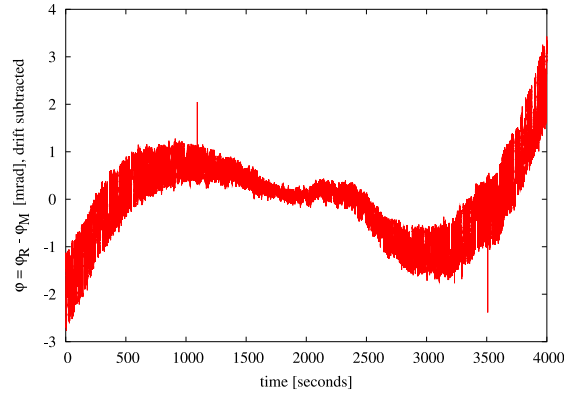
Figure 2.15: Time series of the main measurement $\varphi_M - \varphi_R$, showing excess noise of approximate amplitude 1 mrad.

The excess noise does not show any clear structure if the main measurement $\varphi_M - \varphi_R$ is plotted with the time in the x-axis, as in Figure 2.15. The nature of this excess noise can be understood by analysing the main measurement with respect to the common mode pathlength outside the interferometer Δ_F, which is shown in Figure 2.16. It reveals a sinusoidal structure of the noise term with respect to Δ_F. This means that the cancellation of Δ_F (see Figure 2.7) in the main measurement explained in Equation (2.7) of Section 2.3 is not perfect and works only down to the millirad level, corresponding to nanometre pathlength fluctuations.
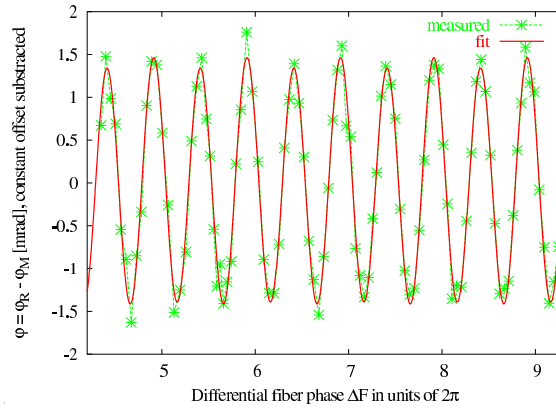
Figure 2.16: Excess noise of the main measurement $\varphi_M - \varphi_R$ with respect to the common mode pathlength outside the interferometer Δ_F, showing a strong periodic dependence.

This noise term was the object of a thorough investigation campaign [28], being its origin found in electromagnetic interferences between the high power RF signals from the AOM drivers. The interferences lead to spurious sidebands in each 80 MHz signal at frequencies which are integer multiples of the heterodyne frequency f_{het}. This causes that both laser beams already contain spurious amplitude and frequency modulation at the heterodyne frequency and harmonics before they are sent onto the optical bench to interfere. These

modulations appear in the detected interference signal as small beat notes at the hetero-dyne frequency that add to the ideal optical beat note of Equation 2.3, but with different phase. The phasemeter extracts the phase of the the vectorial addition of the optical beat note plus the unwanted interference and not from the pure optical beat note, what motivated the name of "small vector" noise for this phenomenon.

This kind of noise sources where a signal at the same frequency but with a different phase adds to the measurement signal appear very frequently in interferometry caused by different mechanisms such as polarising optics, stray-light, cross-talk between phasemeter or front-end channels. Care has been taken since the explanation of the origin for this particular coupling mechanism to define the requirements of LTP electronics such as the modulation drivers and QPD preamplifiers. The experience gained with this noise source will also be of great advantage for the future LISA design and testing.

To show the clear dependence of $\varphi_M - \varphi_R$ with Δ_F in the measurement presented in Figure 2.16, the PZT-mounted mirror on the modulation bench was used to ramp Δ_F over several radians. Using this same PZT actuator as part of an stabilisation to lock Δ_F is the best way to suppress the effects of the excess noise described in the past section. The implementation of the stabilisation of the optical pathlength difference (OPD) will be discussed in detail in Section 5.4.

2.5.3. Final Performance

Once the OPD stabilisation was implemented, the measured interferometric sensitivity fulfilled the specifications. Figure 2.17 shows four curves that represent a summary of the milestones achieved in the last years in demonstration of performance with the LTP metrology system.

All curves were obtained as the linear spectral density of a long time series of one main interferometric measurement $\varphi_M - \varphi_R$.

Beginning from the top, the first curve was obtained at TNO[6] during the environmental qualification campaign of the optical bench engineering model [31] without the OPD stabilisation. The second curve was obtained during the same campaign with active OPD stabilisation. The third curve was obtained previously in Glasgow in collaboration between the IGR and the AEI. It was measured with the AEI phasemeter on the IGR monolithic optical bench prototype [26, 27]. Finally, the last curve represents the best performance obtained in the AEI laboratories with the experimental setup described in Section 2.5.1.

Figure 2.18 shows the interferometric sensitivity to test mass angular noise and the re-quirement of $10\,\mathrm{nrad}/\sqrt{\mathrm{Hz}}$. It was obtained from the DWS alignment signals recorded during the measurement run showing the best performance in Figure 2.17 and scaled with a factor 5000 rad/rad to obtain test mass angular fluctuations, as presented in Section 2.4.

---

[6]TNO: Netherlands Organisation for Applied Scientific Research
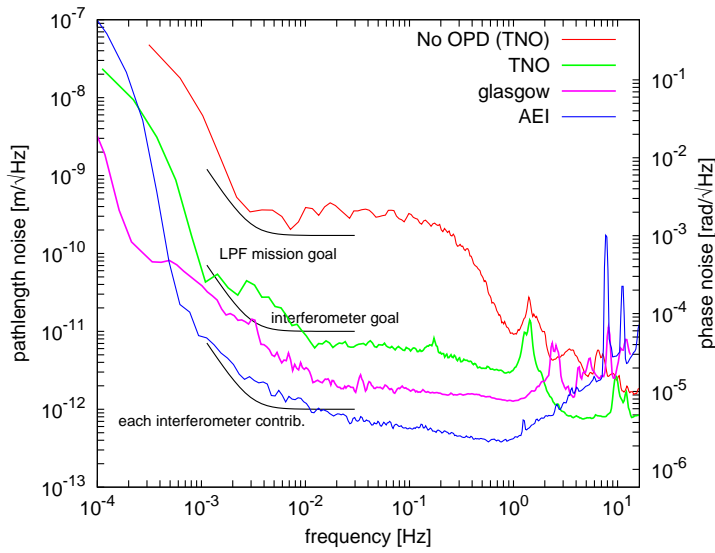
Figure 2.17: Milestones in the performance of the LTP interferometer and phasemeter: the first test of the AEI phasemeter with a monolithic interferometer in Glasgow, the environmental qualification of the EM OB at TNO and the actual performance with the EM OB at the AEI laboratories.
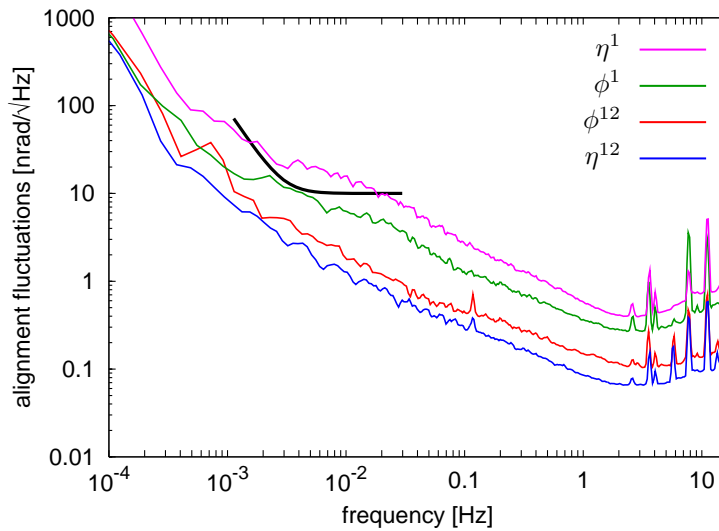
Figure 2.18: Alignment noise corresponding to the best performance shown in Figure 2.17.

2.6. Conclusions

The implementation of the LTP interferometry discussed in this Chapter has demonstrated the required sensitivity of $10 \, \mathrm{pm}/\sqrt{\mathrm{Hz}}$ at $1 \, \mathrm{mHz}$ shown in Section 2.2. The required dynamic range and alignment sensitivity have been also demonstrated. The setup of such a sensitive demonstration, has allowed the exact definition of design requirements to be delivered to the industry for the manufacture of the flight hardware and software.

Besides, the sensitivity achieved and the resemblance with the LTP design allow realistic characterisations of procedures as the initial alignment of the test masses presented in Chapter 3, the analysis of performance and limitations of the laser stabilisations necessary to achieve picometre sensitivity presented in Chapter 5 and the investigations of the excess pathlength noise introduced by the optical windows, the only transmissive elements of the interferometer outside the optical bench, presented in Chapter 7.

Chapter 3.

Autonomous alignment of the LTP test masses

LTP comprises two free-floating test masses as inertial sensors whose positions and alignment fluctuations are monitored by a set of interferometers that use them as end-mirrors. At the beginning of the LTP science operations, the test masses will not be aligned with the interferometer, so that an alignment procedure was developed that uses the interferometric DC and DWS alignment signals to correctly position the test masses.

This chapter presents the successful test of this procedure on the engineering model of the optical bench, using movable mirrors actuated by piezoelectric-electric transducers as test masses.

The results presented here have been already been published [35, 36, 37]. The different subsystems of the LTP interferometry and alignment signals used for the implementation discussed here have been presented in Chapter 2.

3.1. Introduction

The LISA and LTP test masses are designed to be free floating during nominal mission operation, but have to be firmly caged with the caging mechanism shown in Figure 3.1 during launch and subsequent manoeuvres until the science phase of the mission begins.

The alignment of the test masses with respect to the interferometer just after being released will most probably be far from the nominal position and no interference signal will be detected in the measurements interferometers X1 and X12.

It will be necessary to perform a spiral-shaped scanning movements with the test masses until some light hits the photodiode and use the alignment signals from the interferometer from this point to obtain interference between the two laser beams first and finally maximise the interferometric contrast.

Figure 3.1: Caging mechanism. Source EADS Astrium.

3.2. Selected alignment signals

Some of the alignment signals presented in Chapter 2 will be used in the alignment procedure:

Total power Σ: is the sum of the averaged power measured by each quadrant, as described in Equation (2.23). This is a non-negative number, which is scaled such that a value of 1.0 (nominal value) indicates when both the Measurement Beam (MB) and Reference Beam (RB) are switched on and well-aligned. Experimental values from previous runs or the best available prediction are used for this scaling.

DC alignment DC^{ϕ} and DC^{η}: the horizontal DC alignment DC^{ϕ} is calculated as the difference between the averaged power measured by the left and right section of the QPD, as described in Equation (2.22). The vertical DC alignment DC^{η} is calculated as the difference between the upper and lower section, as described in Equation (2.24). They are normalised by the unscaled Σ, such that the variation range is $-1 \ldots 1$ (0 at the centre of the QPD).

DWS alignment DWS^{ϕ} and DWS^{η}: gives the difference, in radian, between the phase measured by the left and right section of the QPD (horizontal DWS^{ϕ}, Equation (2.16)) or the upper and lower section (vertical DWS^{η}, Equation (2.17)).

Contrast on the QPD c: provides the contrast measured over the whole surface of the QPD. This is a number between 0 and 1 (also usual to be expressed as $0\,\% \ldots 100\,\%$).

Raw data delivered by the phasemeter [33] is used to generate these signals in the Data Management Unit (DMU). These signals are labelled with a lower index '1', '12', 'R' or 'F' to indicate from which interferometer they originate. For example, interferometer X1 produces the signals Σ_1, DC_1^{ϕ}, DC_1^{η}, DWS_1^{ϕ}, DWS_1^{η} and c_1.

3.3. Interferometer initial acquisition

The procedure is designed as a control sequence in three different stages. It begins from a completely misaligned interferometer, where the beam that is reflected off the test mass (MB) does not hit the photodiode and uses the alignment signals delivered by the DMU as criterion to enter the next alignment stage. The flow diagram of the control logic for the alignment of TM1 is shown in Figure 3.2 and can be summarised as follows:

Scan: At this step, only the reference beam (RB) hits the QPD. The test mass is moved following a spiral around the nominal incoming beam axes. This way, the reflected measurement beam (MB) describes an spiral on the detection plane until a certain percentage of it is detected by the QPD and enters the next stage "DC".
If this process exceeds a certain predefined time, a time-out flag is set: RB is turned off to be able to detect the slightest amount of MB that hits the photodiode and the scanning process is repeated with a finer spiralling ratio. If this second scanning is not successful a second "time-out" event occurs and an ERROR message signalises a malfunction of the Optical Metrology System, requiring intervention from ground.
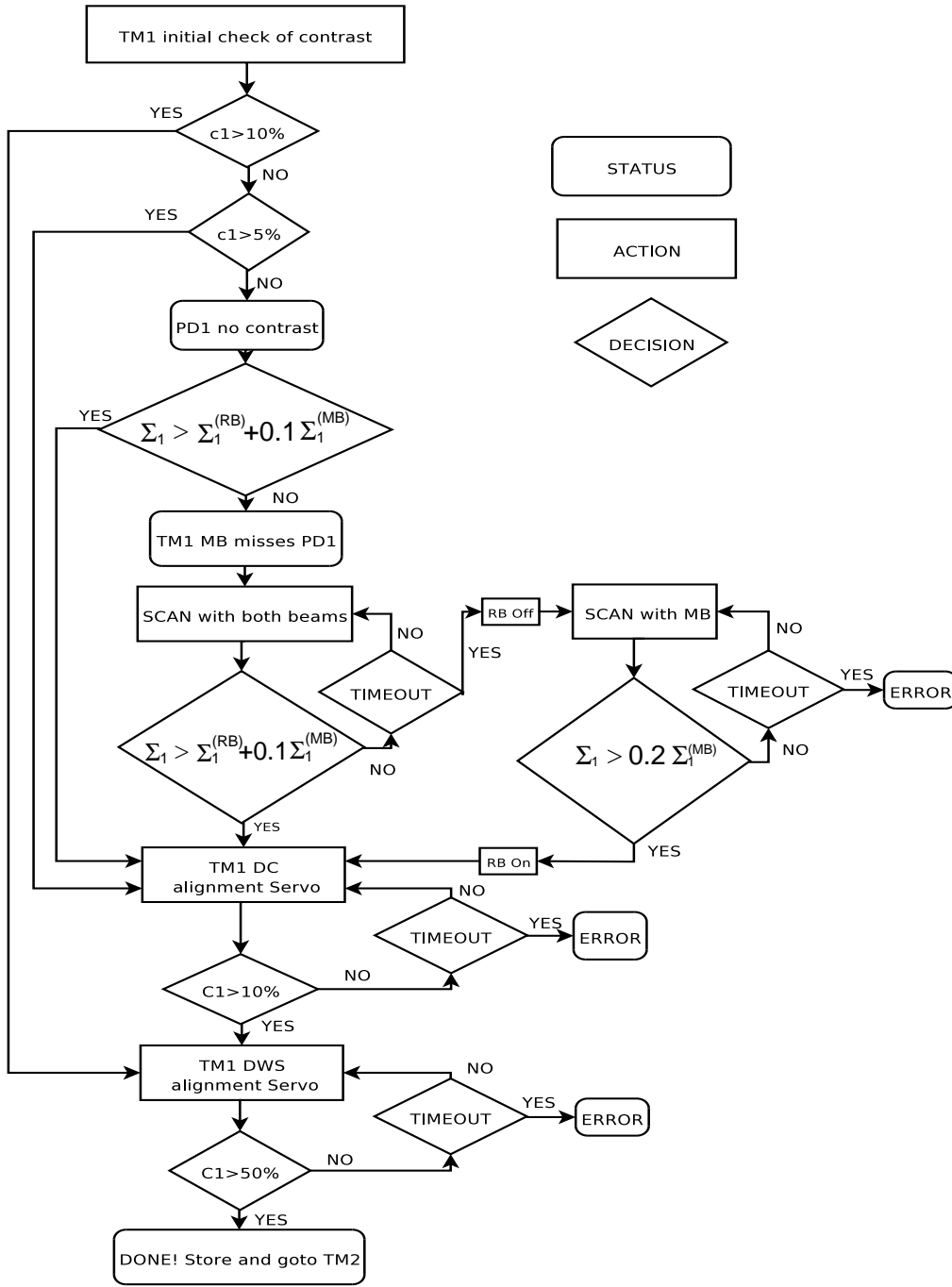
Figure 3.2: Alignment procedure for test mass one (TM1). Reference values for Σ are indicated with an upper index in parentheses such us RB or MB depending on which of the two beams is switched on. For this and other reference values, measurements stored during past runs or predictions based on ground tests are used.

DC: The measurement beam hits the QPD, but no interference occurs. The test mass is aligned using a control loop with the DC alignment signals as error signals. The target is not to reach zero but a value estimated in earlier runs or the best theoretical prediction.

DWS: Both beams interfere to a level such that a predefined contrast threshold has been achieved. The test mass is aligned using a control loop with the DWS alignment signals as error signals. The target is to reach zero, as this means optimal overlap of the two interfering beams. This alignment has a higher sensitivity in comparison to the DC alignment but a smaller dynamic range.

Each interferometer is considered to be properly aligned if it delivers contrast values greater than 50 % and the DWS signals reach zero.

Note the different nature of the DC and DWS alignment signals: DC signals have a larger dynamic range and are not necessarily zero for optimal alignment, as they base on ratiometric measurement of the laser power referred to the centre of the QPD. DWS signals are zero for an optimal alignment, which is to first order independent of the diode position ([30]), and offer better precision over a shorter dynamic range, as they are based on the interference between the two beams.

3.3.1. Experimental implementation

The alignment procedure was tested on the Engineering Model of the LTP optical bench shown in Figure 2.13 with the experimental setup presented in Section 2.5.1 but the dummy mirror that usually acts as TM1 was substituted by a 3-axis PZT. Alignment signals were produced by the phasemeter "pm3" shown in Figure 2.14 and the back-end calculations were performed by a laboratory PC (instead of the DMU on-board LTP).

For this experiment, the PC also produced the feedback signals for the 3-axis PZT that acts as TM1. Because of the limited dynamic range of the used PZT, the criteria to switch between the stages during the acquisition had to be re-defined as follows: for a contrast value below 60 % the PZT performs a scan. The DC-servo is switched on when the contrast reaches th threshold of 60 % and the DWS-servo takes over from 75 % until the end of the alignment. Implementation of the procedure with higher dynamic range PZTs is foreseen to study the convergence of the procedure under more stringent start parameters.

Figure 3.3 shows the time evolution of the alignment procedure. The upper part shows the evolution of the contrast of the interferometer being aligned X1 c_1 and the contrast of the reference interferometer c_R, that remains constant, for comparison. The lower part of the figure shows the evolution of the DC and DWS alignment signals.

During the first stage (SCAN) the TM is scanned and the contrast c_1 varies accordingly until it achieves the predefined threshold of 60 %, and enters the next stage (DC). In the second stage the DC signals are used as error signals for a control loop that drives the test masses. The contrast increases rapidly and achieves the 75 % threshold that leads

to the DWS stage. In this final stage, the DWS signals are used as error signals for the control loop and the highest contrast value near 85 % is achieved. Note how both DWS alignment signals in the lower plot of Figure 3.3 are brought to zero, which characterises an optimal overlap of the interfering beams.
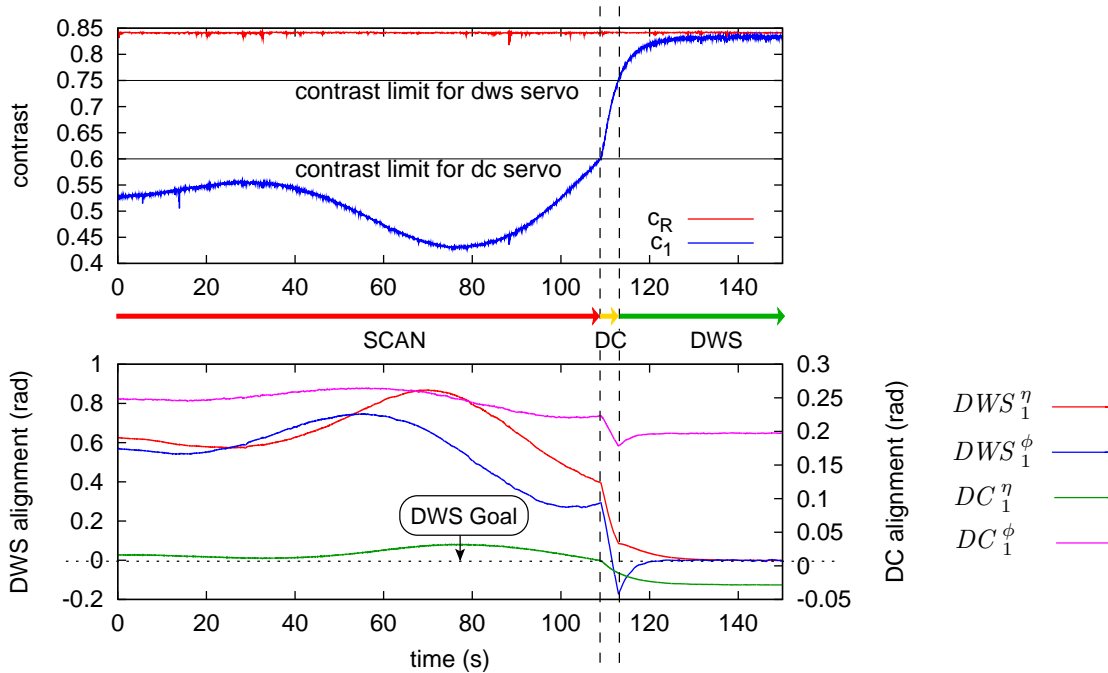
Figure 3.3: Time evolution of the alignment: test mass is scanned until contrast in interferometer **1** (blue curve in upper graph) reaches the 60 % threshold. Then the DC-servo is switched on (signals green and magenta in the lower graph) and contrast value achieves 75 %. At this point the DWS-servo takes over until its error signals (red and blue in the lower graph) are zero and the contrast is optimal.

Figure 3.4 and 3.5 show a different representation of the alignment signals. It is a parametric plot of the alignment procedure presented in Figure 3.3 with the time as running parameter. Figure 3.4 shows the evolution of the DC alignment, with the signal DC_1^ϕ on the x-axis and DC_1^η on the y-axis. The evolution of the DWS alignment can be seen on Figure 3.4. The spiral-like movement of the mirror that acts as test mass is easily recognisable in this representation, as well as the achievement of the DWS alignment goal at $(0,0)$.

3.4. Conclusions and outlook

We have presented the design and successful implementation of a procedure to align the LTP test masses with respect to the LTP interferometer. After the procedure, the alignment quality and contrast in the measurement interferometer are comparable to that
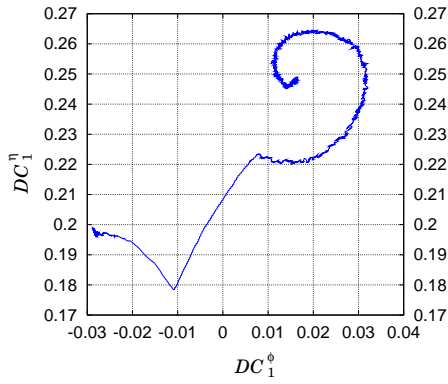
Figure 3.4: Two-dimensional representation of the DC signals during the alignment procedure.
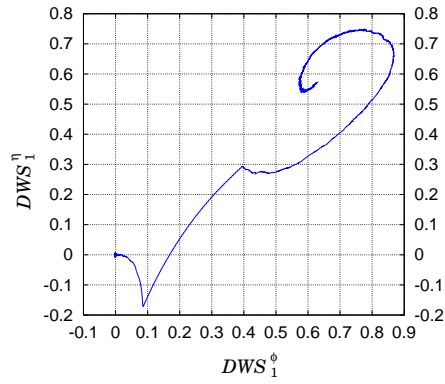
Figure 3.5: Two-dimensional representation of the DWS signals, which are zero when the procedure is finished.

of the interferometers containing only components bonded to the optical bench.

The initial misalignment of the implementation presented here was not as high as the initial misalignment expected for the first implementation of this procedure on-board LTP. This was due to the reduced dynamic range of the 3-axis PZT used as test mass. It is foreseen to implement this procedure with a larger dynamic range, so that during the scanning stage almost or no light at all hits the photodiode.

For the implementation on LTP, the dynamics of the test mass and electrode housing will have to be integrated in the procedure in order to optimise the spiral function used during the scan procedure, and determine the values of important parameters in the alignment procedure, such as the time-out flag. Simulations of the test masses dynamics have already been done in the mission master plan [38] and the determination of the exact parameters for the procedure is also underway in the frame of the software definition for the LTP on-board computer [37].

The alignment procedure for LISA is more complicated than the one presented here. In the actual baseline presented in Chapter 1, one LISA arm is split in three interferometers and the alignment of the local optical bench to the remote optical bench will be much more demanding than the procedure presented here. However, the procedure to align the test mass with the local interferometry that will have to be performed in LISA is practically identical to the one presented in this chapter.

Chapter 4.

Optical readout of LISA test mass position and attitude

The baseline strategy for the position determination of the LISA test masses in the non-sensitive degrees of freedom uses the same capacitive electrodes that surround the test mass and also actuate its position. The implementation of an optical readout would increase the sensitivity for these degrees of freedom and thus reduce the effect of their cross-coupling in the main measurement axis.

Furthermore, a dedicated optical readout could also be used for the local part of the main measurement in the sensitive axes x if it is implemented in the split interferometry configuration explained in Chapter 1. In this case, the required sensitivity would be much higher than for the others degrees of freedom y and z.

We present in this chapter a bread-board implementation of an optical readout that is based on a Mach-Zehnder interferometer with a phase modulation in one arm and the corresponding phase acquisition, from which the position fluctuations of a test mass used as mirror of this interferometer can be measured.

Other possible implementations are currently under investigation among the LISA community. The one with the most space heritage would be the direct application of the LTP interferometry discussed in Chapter 2. A line of investigation is being followed for the use of the LTP interferometry with a modified optical bench [39]. A compact homodyne interferometer [40] is also being investigated, as well as a very robust and straight-forward implementation of an optical lever [41].

4.1. Optical readout for LISA

The capabilities and required sensitivity of an optical readout system for the sensitive axes x are comparable to the ones presented for the LTP and relaxed by a factor ≈ 10 for the non-sensitive axes y and z. They can be summarised as follows:

- Longitudinal sensitivity of $5\,\mathrm{pm}/\sqrt{\mathrm{Hz}}$ for x (out of $40\,\mathrm{pm}/\sqrt{\mathrm{Hz}}$ allocated for the whole interferometry) and $100\,\mathrm{pm}/\sqrt{\mathrm{Hz}}$ for y and z, in order to obtain a noticeable

improvement with respect to the nominal $2\,\mathrm{nm}/\sqrt{\mathrm{Hz}}$ precision of the capacitive sensing.

- Longitudinal dynamic range of $\pm 50\,\mu\mathrm{m}$, as the test masses are expected to drift at frequencies below the LISA band.
- Alignment sensitivity in the sensitive angles φ, η of $10\,\mathrm{nrad}/\sqrt{\mathrm{Hz}}$. This is required to mitigate impact of crosscoupling from other degrees of freedom. For an auxiliary system in y and z, the alignment noise in the sensitive angles φ, η should be better than $200\,\mathrm{nrad}/\sqrt{\mathrm{Hz}}$.
- Alignment dynamic range of $\pm 100\,\mu\mathrm{rad}$, as the uncertainty of the absolute orientation may be a few $10\,\mu\mathrm{rad}$ during operation.
- It is also desirable to acquire low precision, absolute longitudinal position information.
- Finally, the optical readout must not disturb the main measurement x by more than $1\,\mathrm{pm}/\sqrt{\mathrm{Hz}}$ in any situation.

The frequency dependence of the mentioned requirements is flat down to $1\,\mathrm{mHz}$ and scales like f^{-2} to lower frequencies, as for the LTP and LISA requirements presented in Chapters 1 and 2.

4.2. Deep internal phase modulation

Of several possible implementations, the one discussed in this chapter is the deep internal phase modulation. As will be shown, it fulfils the requirements listed in Section 4.1 and it has potentially the same performance as the LTP interferometry. It also presents the advantage of a much simpler modulation scheme, with the subsequent mass and power saving. In particular, the modulation scheme does not include RF electronics to avoid EM interference effects and reduce heat dissipation.

4.2.1. Motivation

The two-beam interferometer using a local oscillator is the most general and flexible configuration for an optical readout, as shown in Figure 4.1:

This approach offers two complementary output ports and thus redundant signal extraction. The output signal of one photodiode, once it has been converted to voltage by a preamplifier, has been plotted in the right part of Figure 4.1 and is given by

$$V_{\mathrm{PD}} = k\left(1 + c\cos\varphi\right) = k\left(1 + c\cos\left(\frac{2\pi}{\lambda}\delta s\right)\right), \tag{4.1}$$

where k is the mean value of the photodiode output. The interferometric visibility or contrast c is given by

$$c = \frac{V_{\mathrm{max}} - V_{\mathrm{min}}}{V_{\mathrm{max}} + V_{\mathrm{min}}} \tag{4.2}$$
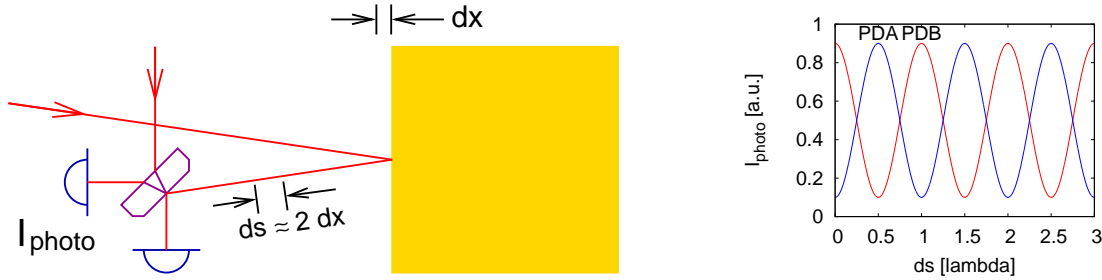
Figure 4.1: Left: general approach to optical readout using a two beam interferometer with non normal incidence. Right. The photodiode output signal with respect to the pathlength difference shows a very reduced linear range. In the maxima and minima there is no sensitivity to test mass position change.

and the interferometric phase φ is proportional to the pathlength difference between the two interferometer arms δs. The output of the complementary output port is phase shifted by π, as can be seen on the right graph in Figure 4.1.

The two input beams can be homodyne or heterodyne, as in the LTP interferometry discussed in Chapter 2. A homodyne implementation is more straightforward, but the sensitivity range where the output signal is linear with respect to the test mass displacement is limited to a small range around mid-fringe, as shown in the right part of Figure 4.1. Near the maxima and the minima, the sensitivity is completely lost: the time series of the photodiode output signal for these operating points would be constant. The required large dynamic range mentioned in Section 4.1 could not be fulfilled.

A small phase modulation in one arm is an established technique to produce a quadrature signal after coherent demodulation ("internal modulation"). With a strong modulation > 1 fringe, distinctive signal shapes are obtained for each operating point. In terms of the photodiode output signal, when a phase modulation of depth m at frequency f_{mod} is applied in one interferometer arm, Equation (4.1) becomes

$$V_{\mathrm{PD}} = k \left(1 + c \cos(m \cos(2\pi f_{\mathrm{mod}} \, t + \psi) + \varphi) \right), \tag{4.3}$$

where the phase ψ has no interferometric relevance and indicates only the phase of the modulation signal. When the photodiode signal is digitised, ψ represents the offset between the sampling clock and the modulation clock.

A graphical interpretation of Equation (4.3) can be seen in Figures 4.2 and 4.3: the first figure shows the original signal from Equation (4.1) with respect to the armlength difference δs and a black arrow indicating a phase modulation that drives the output signal over more than one rad. This causes the time evolution of the photodiode output shown in Figure 4.3. For any given interferometric phase φ or pathlength difference δs, the output signal in the time domain oscillates from its maximum to its minimum amplitude and this way there is always enough signal to noise ratio to extract the value of δs, unless the conversion is not so straightforward as in the simpler sinusoidal form of Equation (4.1) shown in Figure 4.1.
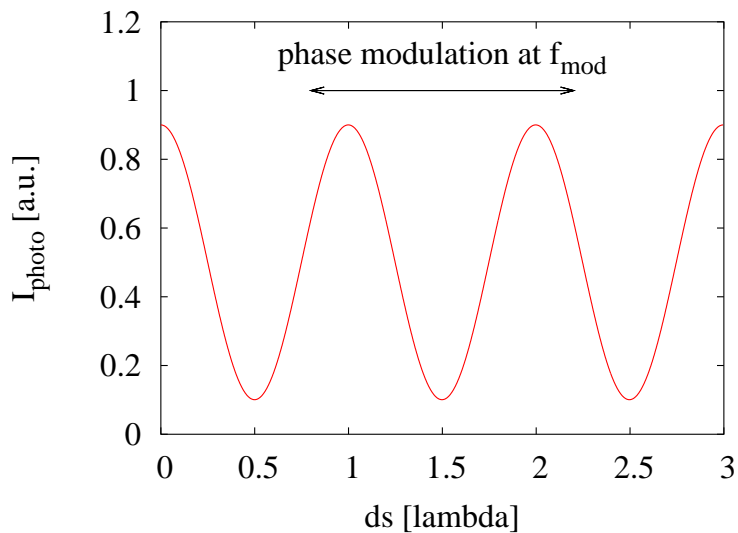
Figure 4.2: The photodiode output signal with respect to the armlength difference δs or interferometric phase φ. When the phase modulation indicated by the black arrow is turned on, the distinctive signals shown in Figure 4.3 are obtained in the time domain for any given operating point.
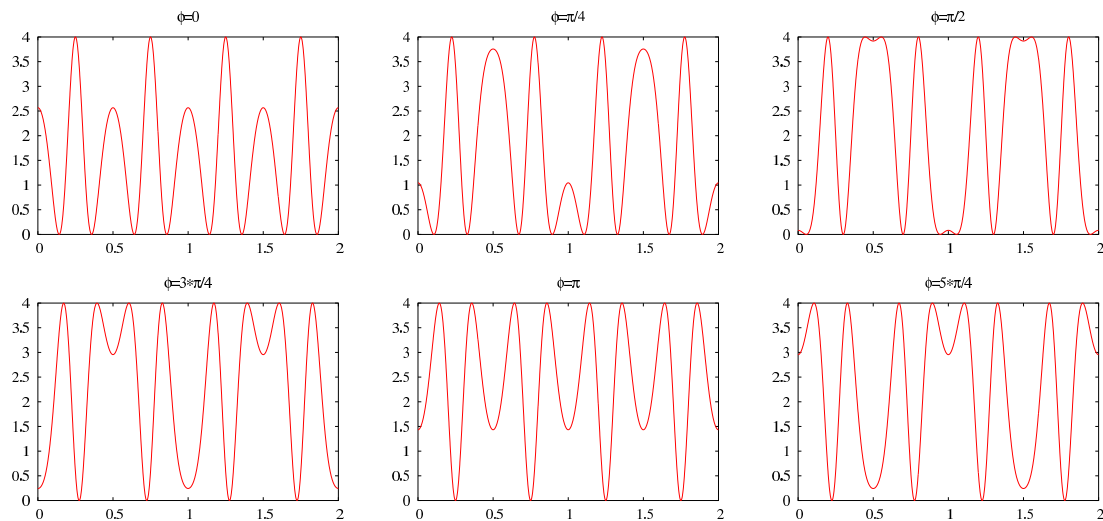
Figure 4.3: Simulation of the time series of the photodiode output for several working points when the phase modulation is applied. For any given working point, enough signal to noise ratio to extract the phase φ is available.

4.2.2. Harmonics analysis

The photodiode signal

$$V_{\mathrm{PD}} = k\left(1 + c\cos(m\cos(2\pi f_{\mathrm{mod}}\,t + \psi) + \varphi)\right),$$

is composed of sinusoidal terms at f_{mod} and its harmonics. It can be expanded in terms of Bessel functions [42] $J_{\mathrm{n}}(m)$ as:

$$V_{\mathrm{PD}} = k + \sum_{n=1}^{\infty} a_n\,\exp\left(\mathrm{i}\,n\,\omega_{\mathrm{mod}}\,t + \psi\right) \tag{4.4}$$

with

$$a_1 = c\,k\,J_1(m)\sin(\varphi),$$
$$a_2 = c\,k\,J_2(m) - \cos(\varphi),$$
$$a_3 = c\,k\,J_3(m) - \sin(\varphi),$$
$$a_4 = c\,k\,J_4(m)\cos(\varphi),$$
$$a_5 = c\,k\,J_5(m)\sin(\varphi),$$
$$\ldots$$

The coefficients of the Fourier series a_n contain all necessary information to extract the interferometric phase φ. In fact, once the two first harmonics are measured, the interferometric phase φ can be estimated with an arctan operation.

4.2.3. Phase readout

The phase readout is divided in three stages, the firsts two of which are very similar to the LTP readout presented in Chapter 2:

Preamplifiers and A/D conversion : The photocurrent is converted into a voltage with a transimpedance preamplifier, sent through a low-pass filter to avoid aliasing and digitised at a sample rate $f_{\mathrm{samp}} = 50$ to $100\,\mathrm{kHz}$. This results in a time series $x_{\mathrm{i}}(t_{\mathrm{i}})$.

FFT : A Fast-Fourier-Transform is performed on the time series $x_{\mathrm{i}}(t_{\mathrm{i}})$. The ten frequency results corresponding to the first ten harmonics of the modulation frequency f_{mod} are selected and sent to the next stage.

Phase readout fit : The Fourier coefficients at frequencies f_{mod} and harmonics are used in a non-linear fit to model the expression of the output signal given by Equation (4.4). There are 4 unknown quantities: the common factor k, the interferometer phase φ, the modulation index m and the modulation phase ψ. For the fit to converge, at least 4 amplitudes $a_1 \ldots a_4$ must be measured. Assuming m and ψ to be known and constant (they are selectable parameters in the experimental implementation), explicit formulae for k and φ exist. In our setup, we assume all 4 quantities unknown and find a least-squares solution using a Levenberg-Marquardt algorithm

and 10 amplitudes $a_1 \ldots a_{10}$, leaving room for additional nonlinearity parameters in the model. After initialisation, the fit algorithm has good initial estimates and hence converges quickly.

This method has several features in common with the LTP readout: first, if QPDs are used on the optical bench, DC and DWS alignment signals can be obtained with identical phasemeter back-end processing as explained in Section 2.3. Second, there is an great reduction in the data to be processed by the back-end computer: N (with N typically 1000) samples of the time series enter the FFT and are reduced to 10 (complex) quantities.

An alternative method would be a direct fit using the digitised time series and the model for the output signal from Equation 4.3. This method has been used for the debugging of the laboratory implementation to be presented in the next section, but would not be easily implemented in real time due to the modest computer performance on-board a satellite.

4.3. Implementation considerations for LISA

Figure 4.4 shows the a conceptual representation of how the deep internal modulation could be implemented for LISA.

In the same way as was discussed for the LTP interferometry, the unstable phase modulator requires that the implementation of this optical readout is split in two different benches, a modulation bench and an optical bench. Also as in LTP, on the optical bench there has to be a reference interferometer that measures all the common mode pathlength noise from the unstable paths and subtracts them from the measurement phase, φ_M - φ_R.

This may at the first sight appear as a disadvantage but there is a way to overcome this difficulty that may result in a system simplification: a multiple modulation bench could provide all necessary pairs of modulated beams to all the optical benches, as shown in Figure 4.4. For the case of a LISA satellite, with two test masses and a maximum of six optical readout system pro test mass, a single dedicated laser (or pick-up from a LISA laser) with one modulation bench could provide light for all twelve optical readout systems from a location far enough from the test masses not to introduce any temperature or mechanical fluctuations near them. Only the heat dissipated by the photodiodes on the optical benches would remain.

The use of QPDs would allow to obtain alignment signals with the differential wavefront sensing (DWS) technique in the same manner as for LTP, as explained in Section 2.4. Absolute displacement of the test mass can also be measured with reduced performance by modulating the laser frequency. This procedure will be discussed in more detail for LTP in Chapter 5

The best way to suppress the coupling of laser frequency noise due to armlength mismatch the optical bench would be the use of a pick up from the already stabilised LISA laser (less than ten milliwatts would be sufficient), or the use of a dedicated laser with a LTP-
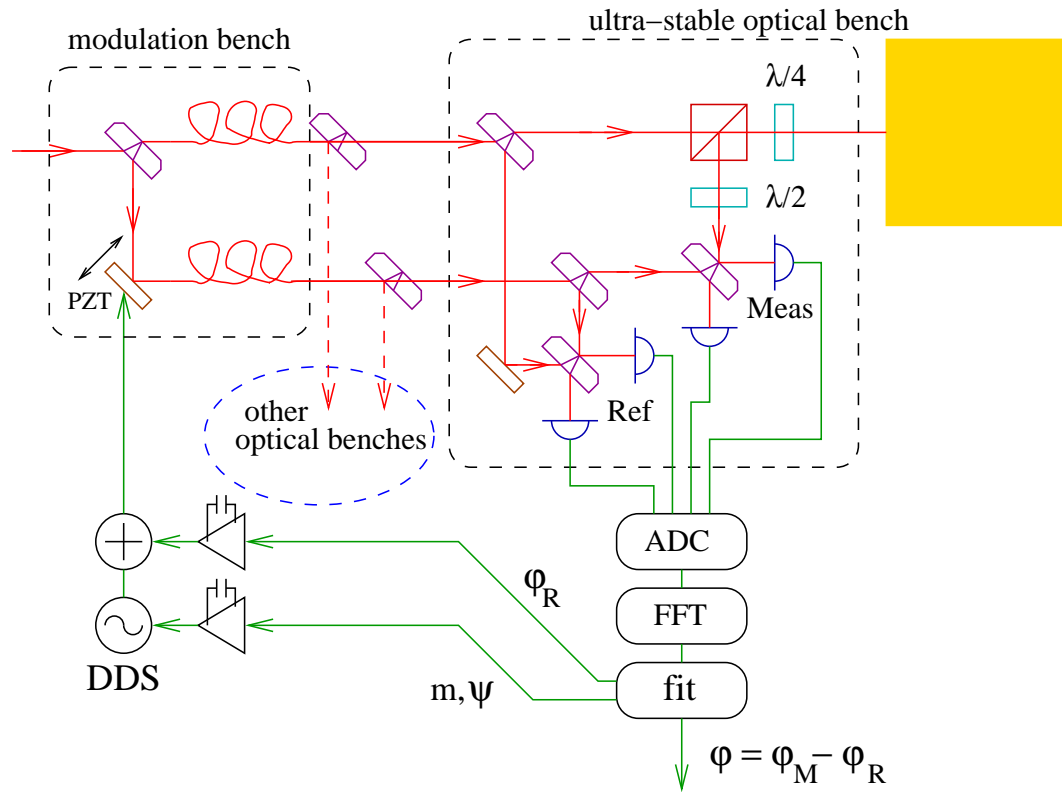
Figure 4.4: Simulation of the time series of the photodiode output for several working points when the phase modulation is applied. For any given working point, enough signal to noise ratio to extract the phase φ is available.

like frequency stabilisation with an extra interferometer with an intentional armlength mismatch on any of the optical benches. A third option would be the use of a dedicated laser phase offset locked to a LISA laser, which would have the advantage of different laser frequencies with respect to the main beam and thus reduced influence of stray light.

Regarding the design of the optical benches, they should be monolithic and as compact as possible. As they only must have two interferometers, a good starting point for an estimation of the achievable dimensions could be the fibre injector optic subassembly (FIOS) [27] designed for LTP ($\approx 5 \times 4\,\mathrm{cm}^2$). The vertical output beams of the FIOS polarising beam splitters (PBS) could be recombined to form the reference interferometer by bonding one more beamsplitter and a half wave plate on top of the present PBS. Only the two beamsplitters of the measurement interferometer shown in Figure 4.4 would need extra space on the assembly itself.

Figure 4.4 also shows the data processing, for which the FFT could be implemented in a dedicated FPGA phasemeter and the back-end processing in a DMU. The immediate results from the DMU can be used for a closed-loop control of the parameters of the DDS responsible for the modulation (to compensate for effects such as slow drifts or aging of the modulator) and also to implement an stabilisation of the pathlength difference outside the optical bench, similar to the OPD stabilisation of LTP.

4.4. Bread-board implementation

The laboratory breadboard implementation of the deep modulation optical readout is shown schematically in Figure 4.5. The phase modulators employed consist of a fibre wound and glued around a ring-shaped PZT, so that a voltage applied on the PZT results in a stretching of the fibre that changes the pathlength of the modulator. These modulators are thoroughly described in Section 5.6.

The main aim of this prototype was to test the functionality of the phase readout presented in Section 4.2.3. The functionality of the implementation can be seen in Figure 4.6, where the modulator in one arm was used for the internal modulation and the other in the second arm was used to ramp the interferometric pathlength with a triangular function of frequency $300\,\mathrm{mHz}$ over ≈ 8 fringes. The readout could track the phase.

The optical bench was made of discrete optical components on metallic mounts and no vacuum environment, so that no representative pathlength stability could be measured. In order to evaluate the sensitivity of the phase readout, a test measurement was done as depicted in Figure 4.5: an independent measurement of φ_A and φ_B was performed and the subtraction $\varphi_\mathrm{A} - \varphi_\mathrm{B} = \pi$ was evaluated. The two complementary output ports of the interferometer cancelled the complete common mode pathlength noise and the nominal phase difference remained π. The linear spectral density of the phase difference calculated this way is shown in Figure 4.7

The achieved performance is around the level of $100\,\mathrm{pm}/\sqrt{\mathrm{Hz}}$ at $1\,\mathrm{mHz}$, and for comparison the relevant performance benchmarks of the LTP interferometry are shown (1, 10
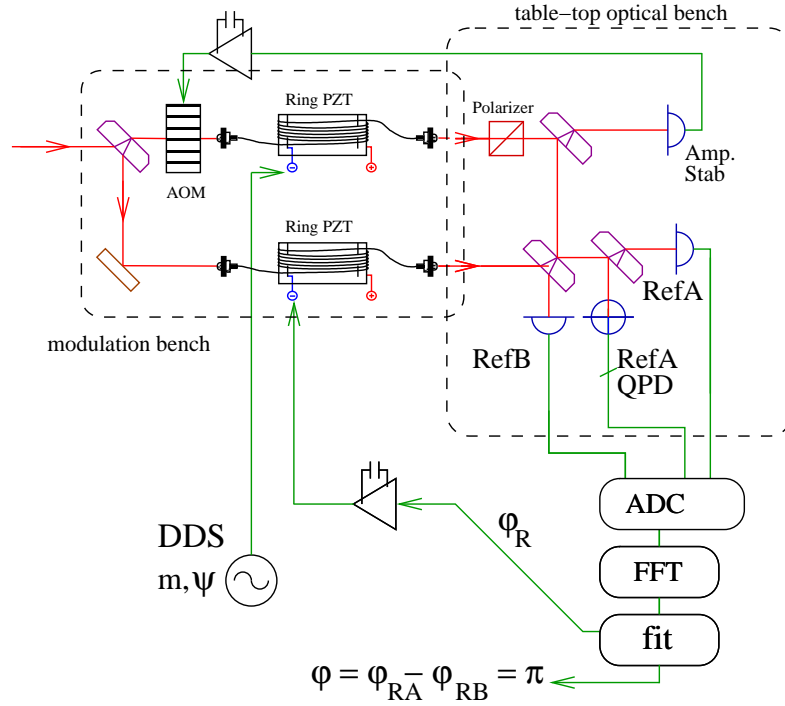
Figure 4.5: Actual laboratory breadboard implementation.
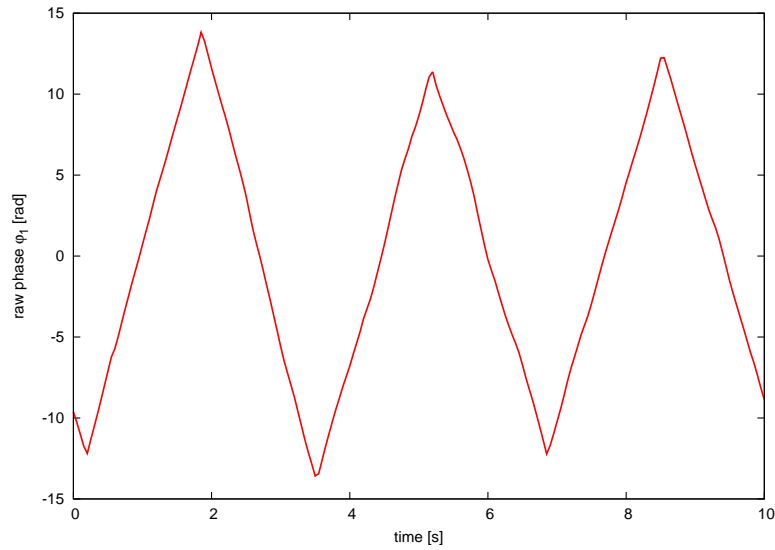
Figure 4.6: Time series of one raw phase measured with the breadboard implementation. The pathlength difference was intentionally ramped over several fringes using the spare phase modulator in one arm.
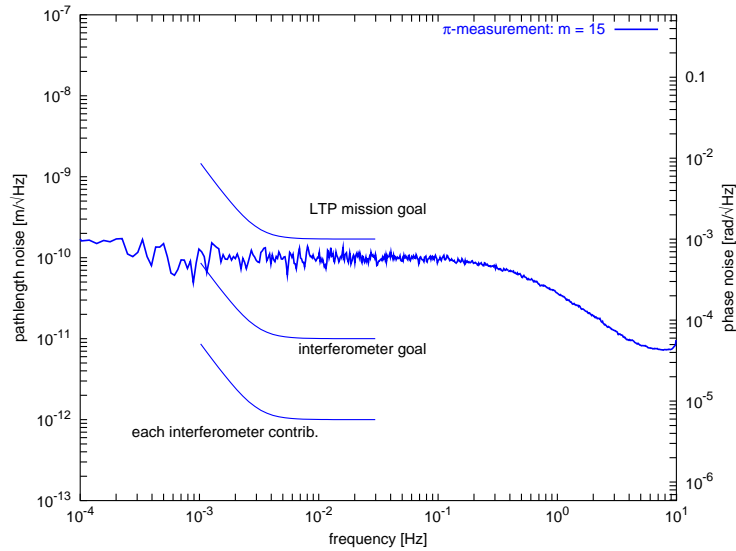
Figure 4.7: Performance of the phase readout system obtained as the subtraction of the phase from two complementary output ports, so that the optical pathlength noise cancels and only the readout noise remains.

and $170\,\mathrm{pm}/\sqrt{\mathrm{Hz}}$, respectively). It is clear from the spectral shape of the obtained noise floor that it is not just given by white digitalisation noise from the phasemeter, but by some kind of systematic error.

Following the experience gained with the LTP interferometry regarding non-linearities at the interferometer output at the sub nanometre level, the representation of the time series of the phase difference $\varphi_1 - \varphi_2$ with respect to the raw phase φ_1 was investigated to try and discover any structure in the noise. Figure 4.8 shows the result of such a measurement, in which is a periodicity of the noise can be recognised.

This non linearity in the subtraction of the two raw phases is what limits the interferometric performance measured in Figure 4.7. It is a similar effect as in the LTP interferometry, and consequently the best method to suppress its influence would be the implementation of an OPD stabilisation as shown in Figure 4.4. Nevertheless, it remains to be understood where exactly this non-linearity originates.

4.5. Conclusions and outlook

The principle of function of an optical readout technique based on a deep internal phase modulation has been demonstrated, including the measurements of position fluctuations and alignment. The unstable breadboard setup did not allow for sensitive measurements of effective pathlength noise but could be used to investigate the readout sensitivity by comparing the phase difference between the two output ports of the interferometer and show a readout sensitivity in the required sub-nm range. This technique brings
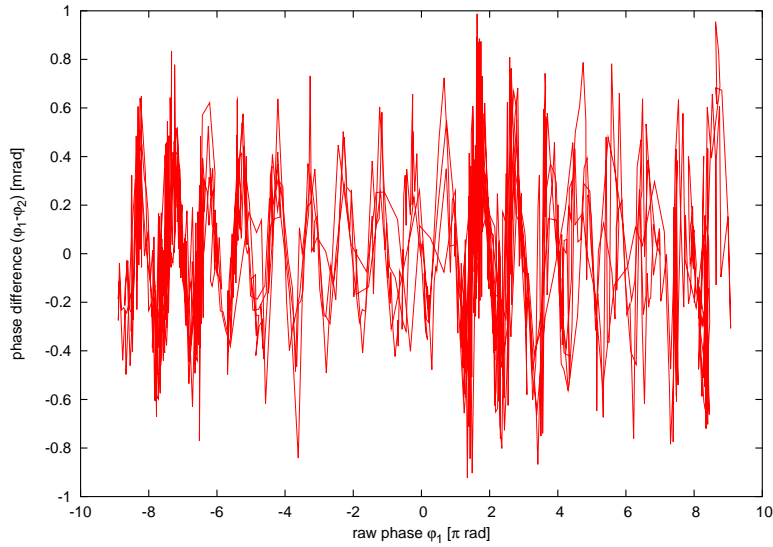
Figure 4.8: Error term of the main interferometric result $\varphi_1 - \varphi_2$ shows periodic dependence with one raw phase φ_1.

much of the advantages of the LTP interferometry with a much more simpler modulation technique.

The future investigations go in the direction of understanding and minimising the sensitivity measurement limitation. Furthermore, an optical bench in vacuum would allow for the measurement of actual pathlength noise with a completely new interferometry. Finally, an ultra stable implementation with monolithic optical bench will have to be tested with space qualification in mind.

Part II.

Characterization and minimization of sensitivity limitations

Chapter 5.

LTP interferometric control loops

In this chapter the implementation of the three main interferometric stabilisations for LTP are presented: laser amplitude[1], frequency, and optical pathlength difference (OPD). It also includes investigation results on an alternative actuator for the case of a fibre-coupled implementation of the OPD stabilisation.

As explained in Chapter 2, these stabilisations aim to maximise the interferometric sensitivity to fluctuations of the test masses position and alignment. Another feature of the stabilisations discussed here is the characterisation of the free-running fluctuations of each physical quantity and the implementation of its associated measurement procedures on-board LTP. The results of these characterisations —for example the on-orbit pathlength fluctuations of optical fibres— constitute essential scientific information for both LPF and LISA.

All the elements of the LTP interferometry referred here, as well as the notation and the experimental setup with the EM OB in the AEI laboratories were introduced in Chapter 2.

Most of the results presented here are based on the noise investigations published in the technical report S2-AEI-TN-3028 "Investigation of noise sources in the LISA Pathfinder interferometer" and have been measured by the AEI LTP team in collaboration with the Glasgow IGR LTP team.

5.1. Introduction

The same structure will be followed to a large extent in the presentation of each control loop: required stability level so that the influence of the noise source in the LTP phase readout remains below $1\,\mathrm{pm}/\sqrt{\mathrm{Hz}}$ at $1\,\mathrm{mHz}$, study of the fluctuations in the environment of the AEI laboratory and analysis of the achieved stability.

The optimal analysis of the performance of a stabilisation is based on an "out-of-loop" measurement of the residual noise. This consists of an independent measurement of the

---

[1]The widely spread terminology "amplitude stabilisation" is used in this work, although strictly speaking only the laser power is measurable and thus power fluctuations are suppressed with this stabilisation. The amplitude is the square root of the power.

stabilised physical quantity under study and represents thus an upper bound for the residual fluctuations. Such a measurement is not always at one's disposal and an indirect characterisation of the stabilised noise source has to be done, the most usual being the so-called "in-loop" fluctuations: the stabilised fluctuations measured by the same sensor used in the control loop. They represent an lower bound of the remaining noise, i.e. their being small guarantees only a proper functioning of the servo, not a low noise level of the stabilised quantity.

The criterion used in this chapter as a confirmation of the sufficient stabilisation is usually the study of the global interferometric sensitivity.

5.2. Amplitude stabilisation

5.2.1. Amplitude stability requirement

The laser amplitude has to be stabilised in two different frequency ranges: in the LTP measurement band from $1\,\mathrm{mHz}$ to $30\,\mathrm{mHz}$, laser power fluctuations produce force noise on the test masses due to radiation pressure [21, 22, 23]. The laboratory implementation of the amplitude stabilisation presented here was not designed to meet this requirement though, because this noise source does not occur with the fixed dummy mirrors that act as test masses in our laboratory. In LTP there is a separate slow digital loop that will take care of long-term drift of the laser power.

A second amplitude stability requirement of $10^{-6}/\sqrt{\mathrm{Hz}}$ relative intensity noise (RIN) is valid at $f_{\mathrm{het}} \approx 1.6\,\mathrm{kHz}$. It emerges from the fact that any amplitude noise around the Fourier frequency f_{het} shows up directly in the phase measurement, as it was already reported in early studies of the LTP interferometry [22]. Back then the requirement was intended for noise sources such as the white digitalisation noise of the phasemeter. Later noise investigations [28] showed also a coherent amplitude modulation at f_{het} caused by electromagnetic interference from the modulation electronics. This coherent amplitude modulation at f_{het} was identified in a thorough noise investigations campaign as being partly responsible for the small non-linearities detected in the LTP phase readout [28]. It was found there that the coupling factor of such a coherent amplitude modulation in the phase readout is similar to that of white noise, so that a relative power stability of 10^{-6} is required.

5.2.2. Implementation

The amplitude stabilisation was realised separately for each beam by measuring their amplitude with a single element photodiode on the optical bench, as explained in Chapter 2. The photodiode PDA1 was used for the measurement beam (MB) and PDA2 for the reference beam (RB), as can be seen in the LTP interferometric layout shown in Figure 2.10. As actuator we used the RF power of each AOM driver.

Figure 5.1 shows the open loop gain (OLG) of the two control loops. At f_{het} they achieved a gain of 42 and 34 dB, respectively. This is in accordance with the servo design which consisted mainly of a bandpass filter at f_{het}, as can be seen in Figure B.1. Together with each measured OLG, Figure 5.1 also shows a model that was fit to the data with LISO [4]. The main result from the model is a delay of $2.84\,\mu$s and $2.55\,\mu$s, respectively. They can be explained by delays in the AOMs, caused by the travel time of the acoustic wave from the RF transducer at one side of the AOM crystal to the laser beam inside the crystal.
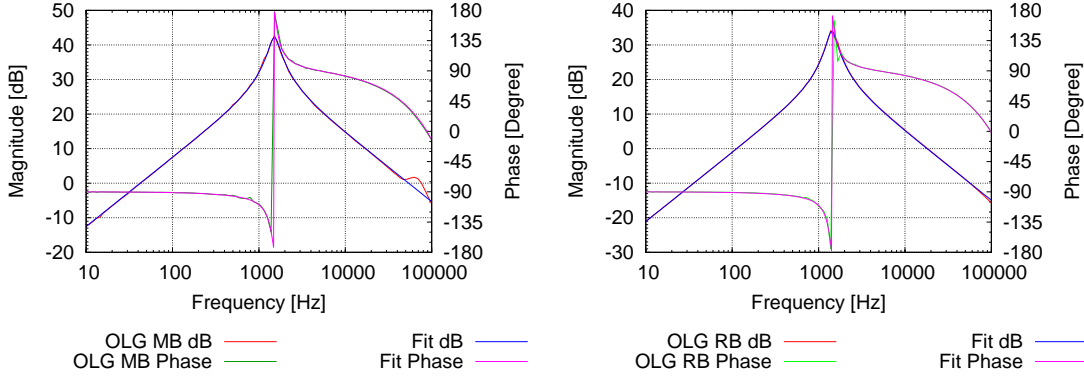
Figure 5.1: Left: Open loop gain (OLG) of the amplitude stabilisation for the measurement beam (MB) acquired with PDA1 (see Figure 2.10). Right: same measurement for the reference beam (RB) acquired with PDA2. A LISO [4] fit to the data has also been plotted, that uncovered a delay of $2.84\,\mu$s and $2.55\,\mu$s respectively, mainly caused by delays in the AOMs.

5.2.3. Performance

As a first approach to study the noise suppression achieved by the stabilisation of the reference beam we will analyse the "in-loop" noise spectra given by the photodiode PDA2, whose signal is used as error signal by the control loop. Figure 5.2 shows the relative intensity noise (RIN) of RB measured with PDA2 when the stabilisation was off (labelled "free-running") and other when the stabilisation was on (labelled "in-loop").

From this measurement we can deduce that the control electronics work properly, but an "out-of-loop" measurement, independent of the control signals, is the best way to obtain the real noise suppression. To this end, the spectra of the photodiode at the output of the frequency interferometer PDFA (see Figure 2.10) were measured. This photodiode is sitting on the optical bench, similarly to PDA2 and measures thus similar amplitude fluctuations. Figure 5.3 shows how the free-running noise is reduced by almost one order of magnitude, in particular the rather high peak at f_{het}.

The corresponding measurements for PDA1 are shown in Figures 5.4 and 5.5. The comparison between the curves free-running and in-loop from Figures 5.4 seems reasonable at the first glimpse, but the "dark noise" curve, measured without any light impinging on the photodiode is abnormally high, indicating that no high noise suppression will be actually achieved by such a photodiode. That is indeed the case, as confirmed by Figure 5.5:
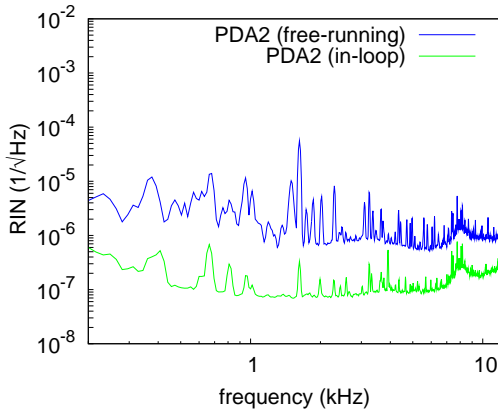
Figure 5.2: In-loop amplitude stability of RB measured with PDA2
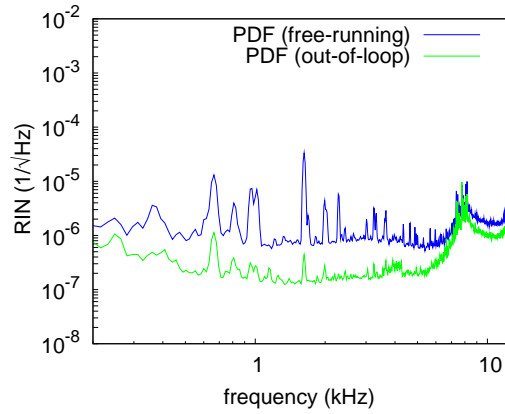
Figure 5.3: Out of loop amplitude stability of RB measured with PDFA.

the stabilised noise level shown by the curve "out-of-loop" measured again with PDFA is limited by the high dark current of the photodiode. Nevertheless there is a remarkable noise reduction in the noise peak at $f_{\text{het}} = 1.6\,\text{kHz}$.
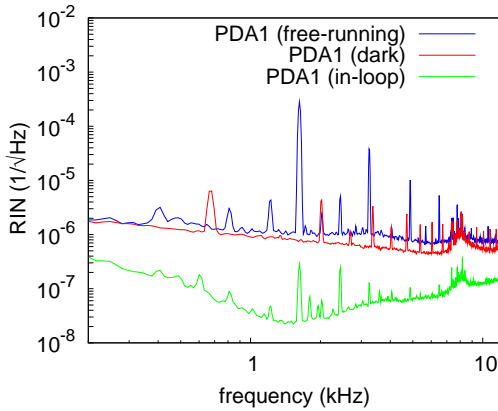
Figure 5.4: In-loop amplitude stability of MB measured with PDA1. Despite the high in-loop noise suppression, the high dark current of PDA1 predicts a worse out-of-loop measurement.
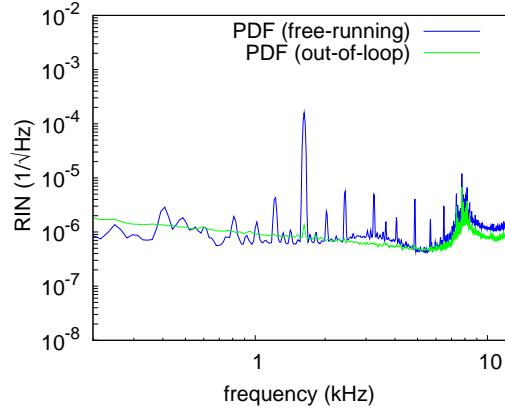
Figure 5.5: Out of loop amplitude stability of MB measured with PDFA. The out-of-loop noise suppression is limited by the high dark current of PDA1 but relevant noise suppression of the spike at f_{het} is achieved.

This photodiode PDA1 had already shown a complete failure during the environmental test campaign of the OB EM [31] but went later spontaneously back to apparently normal operation. The measurement from Figure 5.5 shows, however, that there is still some permanent damage causing the abnormally high dark current.

The present implementation of the amplitude stabilisation allowed a noticeable performance improvement. Figure 5.6 shows the measured interferometric performance without the amplitude stabilisation and just after it was implemented, showing a significantly in-

creased sensitivity in the frequency range from 3 mHz to 30 mHz.
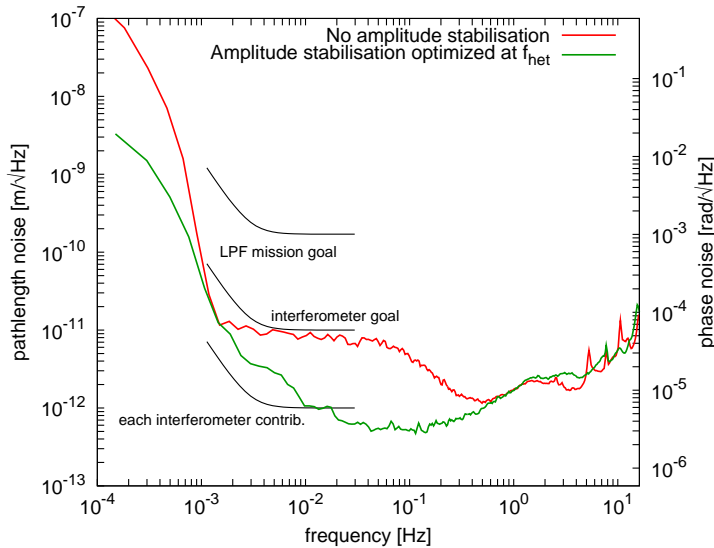
Figure 5.6: Sensitivity of the LTP interferometer and phasemeter before and after the implementation of the amplitude stabilisation with OLG optimised at f_{het}, showing a noticeable performance improvement.

This performance improvement in spite of the abnormally high dark current of PDA1, which only allowed for a noticeable noise suppression at precisely f_{het}, reinforces the prediction that the most critical amplitude noise is the coherent modulation at f_{het} caused by electromagnetic pick-up between the modulation electronics [28]. Besides, in a later setup modification, this photodiode PDA1 was replaced by a new one with a dark current noise comparable to that of PDA2 but no further performance improvement was observed.

The results presented in this section make it clear that the LTP implementation of this stabilisation must have high gain at f_{het}. The only limiting factor for this gain uncovered by the investigations presented here is the acoustic delay in the AOMs, which will eventually limit the servo bandwidth and should thus be kept as small as possible.

5.2.4. Scientific output for LTP and LISA

The amplitude stabilisation on-board LTP will be implemented as follows [37]: two high bandwidth loops will be implemented in the laser modulator using the signals from the photodiodes PDA1 and PDA2 to control separately the light of each beam on the optical bench. These loops will actuate on the two AOM drivers in the same way as the ones described in this section, but with a servo design including gain at DC.

An outer loop will actuate directly the laser power, so that the fast loops do not go out of their dynamic range. To this end, the DMU will sample different control signals (error and feedback signals, RF power, etc) from the fast loops in the laser modulator [37] and

will use them to suppress long-term drifts of the laser power with a low-bandwidth digital loop.

This implementation can be used to characterise the on orbit behaviour of the laser during LTP operation at low frequencies, as an important input for LISA. To this end, a measurement procedure has been included in the mission master plan [38, 43] in which the laser is left free-running and the monitoring signals mentioned above are collected and sent to ground.

5.3. Laser frequency stabilisation

A mismatch of about $\Delta L = 1 \, \text{cm}$ is expected between the arms of the LTP interferometers which consists of different contributions during the construction procedure and real test mass displacements. As explained in Chapter 2, this causes apparent pathlength fluctuations $\widetilde{\delta s}$ induced by frequency noise $\widetilde{\delta \nu}$ that are given by

$$\widetilde{\delta s} = \frac{\widetilde{\delta \nu}}{\nu} \Delta L, \tag{5.1}$$

where ν is the laser frequency. For the pathlength fluctuations to remain below $1 \, \text{pm}/\sqrt{\text{Hz}}$ or equivalently for the phase fluctuations $\widetilde{\delta \varphi} = \frac{2\pi \nu \widetilde{\delta s}}{c}$ to remain below $5.9 \, \mu\text{rad}/\sqrt{\text{Hz}}$, a frequency stability of

$$\widetilde{\delta \nu} = \frac{c}{2\pi \Delta L} \widetilde{\delta \varphi} = 28 \, \frac{\text{kHz}}{\sqrt{\text{Hz}}} \left[\frac{1 \, \text{cm}}{\Delta L} \right] \tag{5.2}$$

is required.

Note that in the main LTP measurement channels $(\varphi_1 - \varphi_R)$ and $(\varphi_{12} - \varphi_R)$ the frequency noise due to armlength mismatch in the common part of the interferometers (modulation bench and optical fibres) is a common-mode signal and cancels, so that armlength mismatches on the optical bench are more critical. Luckily, the high precision alignment to be achieved on the optical bench will minimise this contribution.

In order to detect the laser frequency noise, the "frequency interferometer" was designed with an intentionally large armlength mismatch of about 38 cm, as shown in Figure 2.8. To obtain a valid error signal, the reference phase φ_R is subtracted from the output phase of the frequency interferometer φ_F. In this error signal $(\varphi_R - \varphi_F)$, the common-mode environmental noise is cancelled and only the laser frequency fluctuations are left. It can then be used in two different ways: either in an active stabilisation to lock the laser frequency, or the laser can be left free-running and the signal used to remove the frequency induced phase noise of the main measurement channels $(\varphi_{X1} - \varphi_R$ and $\varphi_{X12} - \varphi_R)$ by post-processing.

5.3.1. Noise subtraction

First, we will analyse the technique of noise subtraction by post-processing. The first step is the determination of the frequency coupling coefficient in the measurement signal $\varphi_M - \varphi_R$ (where M is used to designate either the X1 or the X12 interferometer) and in the frequency detection signal $\varphi_F - \varphi_R$. This is done by modulating the laser frequency at about 1 Hz and observing the modulation in the corresponding phasemeter outputs, where they appear scaled by the armlength difference of each interferometer, as given by Equation (5.1).

This was done for example in the investigation campaign conducted in Glasgow by the LTP teams from AEI and IGR [26]. In the Glasgow OB prototype [27] used in this investigation campaign, there was only one measurement interferometer and its output phase will be denoted as φ_M. The resulting ratio of the modulation peak height was

$$\frac{\delta(\varphi_F - \varphi_R)}{\delta(\varphi_M - \varphi_R)} = 78.3 \tag{5.3}$$

and it was used in a long-term measurement to obtain a corrected interferometer output

$$\Psi_{\text{corr}} = (\varphi_M - \varphi_R) - 78.3 \cdot (\varphi_F - \varphi_R). \tag{5.4}$$

The spectral sensitivity achieved in this measurement is shown in Figure 5.7. Except for the peaks around 1 mHz, which were caused by environmental temperature fluctuations, the measured phase is clearly dominated by the free-running laser frequency noise with a $1/f$ linear spectral density. The second curve shows a noise projection of the phase sensitive to laser frequency noise ($\varphi_M - \varphi_R$) into the measurement phase ($\varphi_M - \varphi_R$), done with the measured coupling factor $\frac{1}{78.3}$. The fact that this scaling brings the curve to the level of the main interferometric result ($\varphi_M - \varphi_R$) confirms the validity of the coupling factor from Equation (5.3). Finally, the third curve is the corrected phase Ψ_{corr}, whose sensitivity is clearly improved but still remains above the specification of $10\,\text{pm}/\sqrt{\text{Hz}}$ at 1 mHz.

Although theoretically both strategies (stabilisation and subtraction) are equivalent, the result shown in Figure 5.7, where the correction of the frequency induced phase noise does not work below a certain level has been measured repeatedly and the best performances of the interferometer and phasemeter system shown in this work are usually measured with an active stabilisation. This is in accordance with the experience from other experiments: it is difficult to obtain more than one order of magnitude of noise reduction by such a subtraction method, and it is always better to actively remove the noise by a suitable stabilisation, if possible.

Another use of the frequency coupling coefficients in the different interferometers is the extraction of information about the armlength mismatch in the different interferometers. These coefficients were determined in the AEI laboratory for the EM OB with the results

$$\frac{\delta(\varphi_F - \varphi_R)}{\delta(\varphi_1 - \varphi_R)} = 48.91 \qquad \frac{\delta(\varphi_F - \varphi_R)}{\delta(\varphi_{12} - \varphi_R)} = 26.61 \tag{5.5}$$
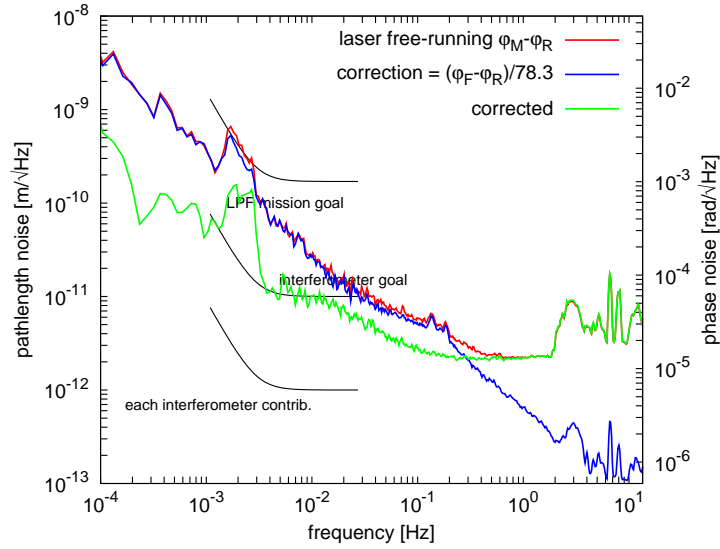
Figure 5.7: Interferometer performance achieved with frequency noise subtraction, measured in Glasgow in collaboration with the IGR LTP team.

Using the known armlength difference of 38 cm in the frequency interferometer, the armlength differences in the other interferometers were computed as

$$\Delta s_1 = \frac{38\,\text{cm}}{48.91} = 7.8\,\text{mm}, \qquad \Delta s_{12} = \frac{38\,\text{cm}}{26.61} = 14.3\,\text{mm}. \tag{5.6}$$

These armlength differences were found to be caused mainly by the missing optical windows in the experimental setup at AEI, and are in reasonable agreement with calculations from the Optocad model shown in Figure 2.10. On the other hand, this confirms the accuracy of the 38 cm intentional armlength mismatch implemented for the frequency interferometer. This 38 cm will be used in Section 5.3.2 to compute the absolute frequency stability achieved with the active stabilisation.

It is also interesting to note that in the same way as the implementation of this procedure in the laboratory delivered information about the missing optical windows, it can be used during the LTP mission to measure the absolute position of the test masses. The accuracy of these results could be increased in two different ways. One option is a detailed measurement of the modulation efficiency of the laser, so that instead of the ratios presented in Equations (5.3) and (5.5), that are affected by the uncertainty in the intentional mismatch, the direct pathlength mismatch could be obtained. However, the modulation efficiency of the laser may be subject to changes during the mission time. A better alternative would be the exact determination of the 38 cm mismatch, as this will remain stable during the mission. To this end, a laser of known actuator efficiency could be used or a laser simultaneously connected to the LTP interferometer and an independent wavemeter (e.g Burleigh Wavemeter WA-1500). Any of these procedures could be performed with the final LTP interferometry assembly previous to launch.

5.3.2. Active laser frequency stabilisation

The implementation of the laser frequency stabilisation in the AEI laboratories with the EM OB was done with an analog servo consisting of two input channels for the photodiode signals of the frequency and reference interferometers PDF and PDR, shown in Figure B.2. The phase difference between the photodiode signals was detected with an analog multiplier and low-passed filtered to suppress the heterodyne frequency and its harmonics. This error signal was converted into two feedback signals: one for the PZT-based fast laser frequency actuator and a second for a slower outer loop that acted the laser crystal temperature. This split actuation scheme has been commonly used in the frequency stabilisation of NPRO lasers [44, 45].

Figure 5.8 shows the open loop gain measured after the stabilisation was implemented. It shows a unity gain frequency (UGF) of 9 Hz and a 1/f increase towards low frequencies, which indicates an expected noise suppression factor of about 10^4 at a millihertz.
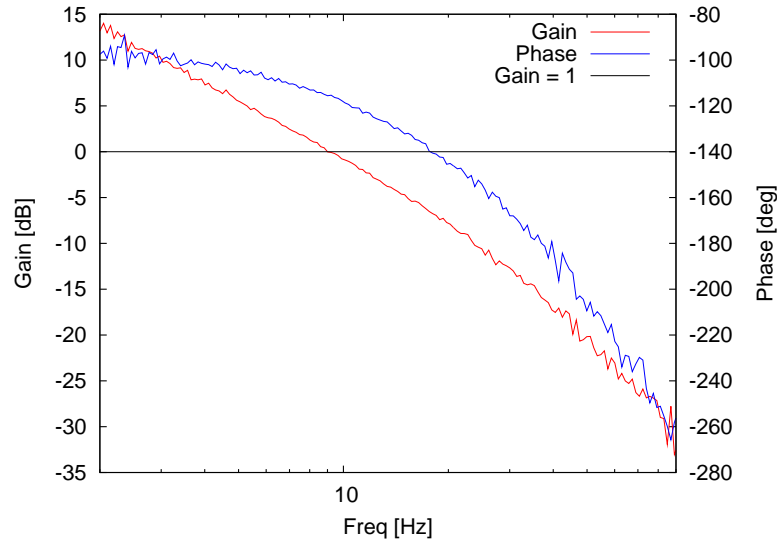
Figure 5.8: Open loop gain of the frequency stabilisation. Unity gain frequency at 9 Hz.

The following Figure 5.9 shows a comparison of the free-running frequency noise, the required stability for LTP and the achieved stability with the control loop presented above. The LTP interferometry does not deliver direct measurements of the laser frequency noise, so that the noise levels labelled "derived" have to be considered as upper limits. The following paragraphs discuss in detail the extensive information shown in this figure.

The curve labelled "free-running measured" is an independent measurement of the free-running frequency noise of the laser head from Tesat "Smart2 engineering model breadboard" at the AEI laboratories. It was performed by locking the laser under study to an ultra stable cavity via a Pound-Drever-Hall stabilisation [46] and recording the actuator signal. The trace shows the frequency fluctuations of the beat note, which is dominated by the frequency noise of the free-running laser. It shows the 1/f spectrum

57
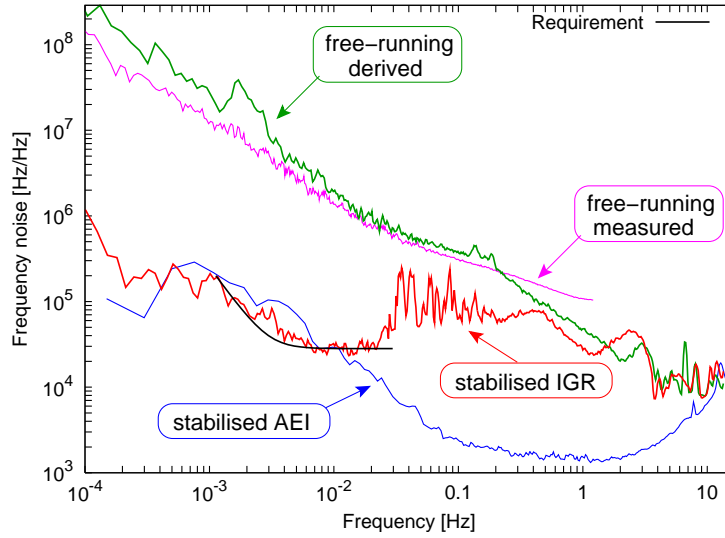
Figure 5.9: Comparison of the free-running laser frequency stability and the residual frequency noise with active stabilisation.

with $10\,\mathrm{MHz}/\sqrt{\mathrm{Hz}}$ at $1\,\mathrm{mHz}$ typical for a NPRO laser. From this curve and the "requirement" curve at $28\,\mathrm{kHz}/\sqrt{\mathrm{Hz}}$, a required loop gain of 100 at $3\,\mathrm{mHz}$ can be predicted, which should be easily achieved considering the open loop gain shown in Figure 5.8.

The curve labelled "free-running derived" has been derived from the interferometric data $\varphi_F - \varphi_R$ measured in Glasgow with free-running laser. The data from the trace labelled "laser free-running" in Figure 5.7 have been inserted in Equation (5.2) using $\Delta L = 30\,\mathrm{cm}$ [27]. It shows a reasonably good agreement with the independently measured one except for the temperature driven peaks at about $1\,\mathrm{mHz}$, taking into account that it was measured with different lasers in different environments.

The two curves labelled "stabilised AEI" and "stabilised IGR" show the stabilised frequency noise measured in Hannover and Glasgow, respectively. The data are acquired as the phase difference $\varphi_R - \varphi_F$ during a long-term run with active frequency stabilisation and converted to frequency noise using Equation (5.2) with the armlength mismatch $\Delta L = 30\,\mathrm{cm}$ for Glasgow and $\Delta L = 38\,\mathrm{cm}$ for Hannover. This substitution in Equation (5.2) can be written as:

$$\widetilde{\delta\nu}_{\mathrm{stab}} = \frac{c}{2\pi\Delta L}\,(\widetilde{\varphi_R - \varphi_F})_{\mathrm{stab}}. \tag{5.7}$$

These stabilised measurements can be considered as out-of-loop measurements because the stabilisations were performed with a different phase measurement system than the LTP-like phasemeter: the analog servo discussed before was used in Hannover and a zero-crossing based phasemeter [27] plus an analog servo was used in Glasgow. It can be seen that the achieved stability does not fully comply with the requirement in any of the implementations, although it has to be kept in mind that this rather stringent

requirement allocates only $1\,\mathrm{pm}\sqrt{\mathrm{Hz}}$ at $1\,\mathrm{mHz}$ and considers pathlength mismatch of $1\,\mathrm{cm}$ for the measurement interferometer.

In order to see whether the residual frequency noise shown in Figure 5.9 dominates the measured pathlength stability $(\varphi_\mathrm{M}-\varphi_\mathrm{R})$ in any of the two setups, this pathlength stability is plotted together with the projected pathlength noise for the Glasgow measurement in Figure 5.10 and for the Hannover measurement in Figure 5.11. The projected pathlength noise in each figure was calculated using the coupling coefficients measured previously in Glasgow and Hannover, respectively. This way, the curve labelled "residual fluctuations" in Figure 5.10 was calculated as

$$(\widetilde{\varphi_\mathrm{M}-\varphi_\mathrm{R}})_\mathrm{res} = \frac{1}{78.3} \times (\widetilde{\varphi_\mathrm{F}-\varphi_\mathrm{R}})_\mathrm{stab} \tag{5.8}$$

and equivalently for the measurement with the Hannover prototype shown in Figure 5.11.
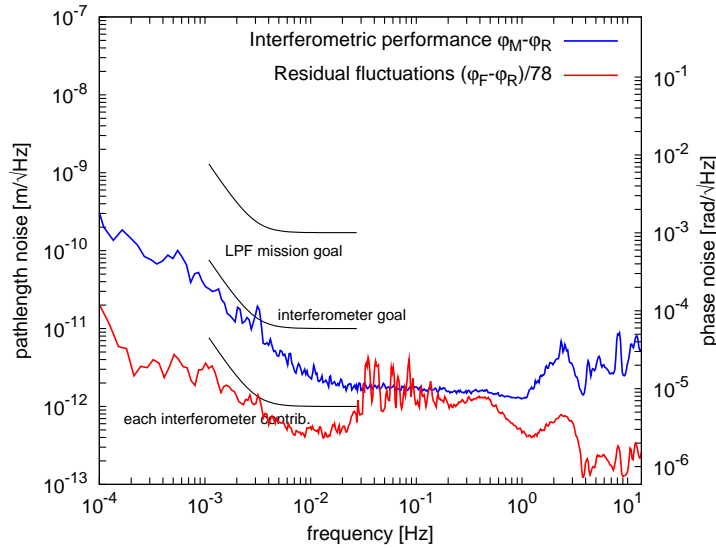
Figure 5.10: Measured pathlength stability and the projected pathlength noise from the remaining residual frequency noise. Measured at IGR with the Glasgow OB prototype.

It can be seen that the residual frequency fluctuations do not dominate the measured performance in the LTP relevant frequency range between 3 and $30\,\mathrm{mHz}$ of any of the two interferometer and phasemeter systems.

This result has been confirmed by fitting the stabilised frequency induced pathlength noise and subtracting the fitted contribution from the main interferometric channel [28]. No improvement of the measurement performance was achieved with the subtraction, indicating that the dominating noise source was not the laser frequency.
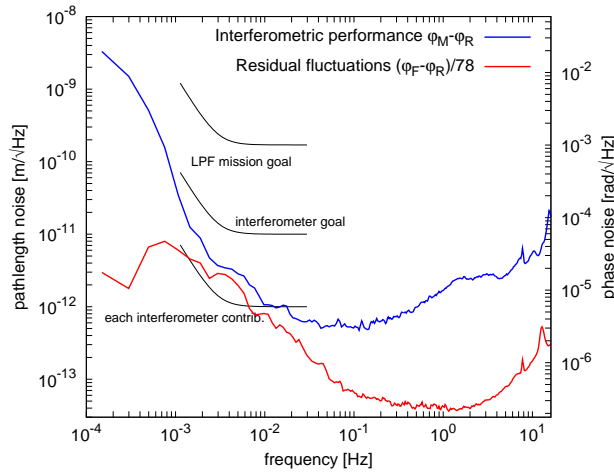
Figure 5.11: Measured pathlength stability and the projected pathlength noise from the remaining residual frequency noise. Measured at AEI with the LTP EM OB.

5.3.3. Scientific output for LTP and LISA

As mentioned in the previous sections, the additional scientific outputs that can be obtained from the frequency stabilisation hardware on-board LTP are the absolute position of the test masses and the on-orbit free-running frequency noise of the laser. Several calibration procedures are foreseen in the experiment master plan [38, 43] to extract this information.

It is also interesting to consider the implementation of the stabilisation strategy presented here as an alternative prestabilisation for LISA, the baseline of which now assumes a Pound-Drever-Hall [46] system with a cavity that is bonded onto the optical bench [10, 2]. Two main considerations are: the intrinsic stability limitations of such a strategy assuming a perfect implementation, and the actual bandwidth limitations that will be imposed by the hardware available on-board LISA. Regarding the achievable stability, both stabilisations are governed by Equation 5.1: the achievable frequency stability is ultimately limited by the relative pathlength fluctuations of the optical components used. The prestabilisation is based in the transfer of the relative stability of a bonded cavity to the laser frequency. In the case of the LTP-like frequency stabilisation, the relative stability of the bonded components that are part of an interferometer are transferred to the laser, so that the achievable stability is comparable, in particular if the cavity components are to be bonded on the LISA optical bench, and the relevant pathlengths are both of order 30 to 50 cm.

The bandwidth limitation of the LTP-like stabilisation with analog electronics presented here is caused by the low heterodyne frequency: the phase detector output has to be low-pass filtered in order to suppress components at f_{het} and harmonics, thus reducing the achievable bandwidth to values well below $f_{\mathrm{het}} = 1.6\,\mathrm{kHz}$. The limitation of the achieved stability measured in Figure 5.9 will be explained in Section 5.5.

In the digital implementation foreseen for LTP, the main limitation of the performance is the update rate of the phasemeter and the back-end calculations. All these delays sum to up to 25 ms in LTP, with a resulting UGF of about 3 Hz. A faster phasemeter with higher update rate will be available for LISA for the implementation of techniques such as arm-locking, so that the expected bandwidth there should not limit the performance.

The advantage of this technique would be the absence of a special locking point, which causes in the actual baseline the necessity of an steerable element in the ultra-stable cavity [10, 2].

5.4. Free-beam implementation of the OPD stabilisation

5.4.1. Requirement and implementation

The OPD stabilisation is the principal mitigation strategy for the noise source associated to the non-linearities of the LTP interferometric readout [28]. As explained in Chapter 2, the environmental pathlength noise that affects all four interferometric phases φ_R, φ_1, φ_{12} and φ_F does not cancel completely in the main interferometric results φ_1-φ_R and φ_{12}-φ_R, so that it has to be stabilised to a level of $5.9 \, \mathrm{mrad}/\sqrt{\mathrm{Hz}}$ at 1 mHz [47]. This pathlength noise is caused by the common non-stable parts of the interferometer outside the optical bench, mainly the single mode fibres between the modulation bench and the optical bench.

In the experimental setup at AEI with the EM OB, φ_R is used as the error signal of a stabilisation that actuates with analog electronics a PZT-mounted mirror in the modulation bench, as can be seen in Figure 2.13. In LTP, the stabilisation will be run digitally on the DMU at 100 Hz update rate using the result of φ_R calculated by the phasemeter back-end. In our laboratory the stabilisation was implemented with an analog servo very similar to the one used for the frequency stabilisation explained in Section 5.3, whose layout is shown in Figure B.2. The only difference with respect to the frequency stabilisation is that instead of locking the phase difference between φ_R and φ_F, the OPD stabilises the phase difference between the interferometric reference phase φ_R and the electric reference phase φ_{el}, which is the reference phase for all the measured phases, derived from the master clock[2].

The open loop gain shown in Figure 5.12 was measured once the stabilisation was implemented. It shows a unity gain frequency (UGF) of 60 Hz and the gain increases as 1/f to low frequencies.

---

[2]Note that the value of φ_R acquired by the phasemeter is already measured with respect to φ_{el}, as this is the phase of the phasemeter sampling clock which is derived from the LTP master clock. On the contrary, the analog servo presented here works by measuring the phase difference between two input signals at f_{het}, so that one input channel has to be fed with an electric signal at f_{het} of phase φ_{el}.
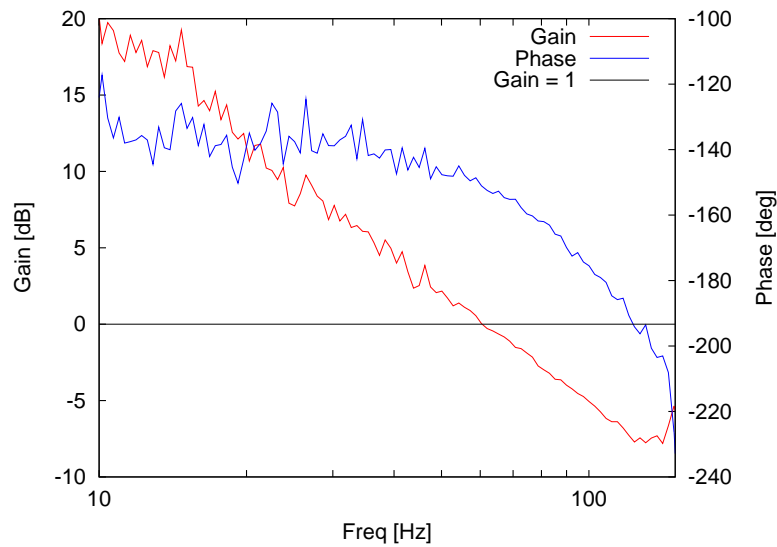
Figure 5.12: Open loop gain of the OPD stabilisation. Unity gain frequency at 60 Hz.

5.4.2. Environmental phase noise and stabilisation performance

Figure 5.13 shows a comparison in the time domain between the free-running and stabilised OPD fluctuations measured in the AEI laboratory. The amplitude of the free-running fluctuations is in the order of tens of radians, several orders of magnitude higher than the stabilised ones, which vary by a few ten millirad.
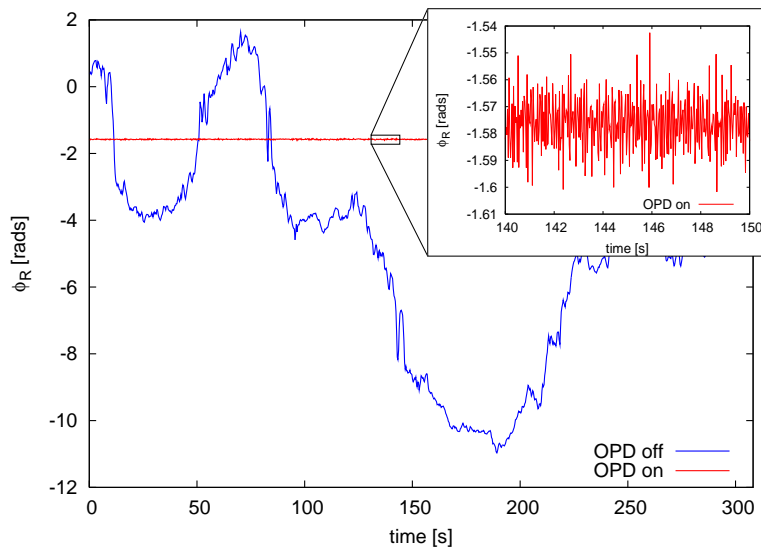
Figure 5.13: Time series of OPD fluctuations measured at AEI-Hannover.

Figure 5.14 shows the linear spectral density of the free-running OPD fluctuations mea-

sured during two different investigation campaigns[3]. The green curve was measured in the TNO[4] laboratory in Delft during the environmental qualification of the OB EM [31] and the red one at the AEI laboratory. The lowest curve labelled "Out-of-loop OPD fluctuations φ_R AEI" shows an out-of-loop measurement of the stabilised OPD fluctuations, measured as the raw phase φ_R during a long rung with active OPD stabilisation.

The stabilised fluctuations can be considered as an out-of-loop measurement because they were measured with the phasemeter, whereas the OPD stabilisation is implemented with the analog loop described in Section 5.4.1. The definition of "out-of-loop" measurement is not always easy, as it has to measure *exactly the same* magnitude fluctuations as the stabilisation sensor but it cannot use *the same* sensor. In this sense it can be argued that the measurement of φ_R performed by the phasemeter uses the same photodiode and preamplifier as the analog servo. Following this argumentation line, the phase of the X1 interferometer φ_1 is also plotted in Figure 5.14 as the curve labelled "Out-of-loop OPD fluctuations φ_1 AEI" and shows the same noise level as φ_R. This confirms that any of them is a valid representation of the residual environmental fluctuations left by the OPD stabilisation, that are clearly below the required $5.9 \, \mathrm{mrad}/\sqrt{\mathrm{Hz}}$.

The comparison between the free-running and the stabilised noise shows that the high noise suppression of several orders of magnitude at $1 \, \mathrm{mHz}$ is met. Furthermore, the fact that the residual stabilised noise remains well below the requirement indicate that this is not limitting the performance of the phasemeter and interferometer system.
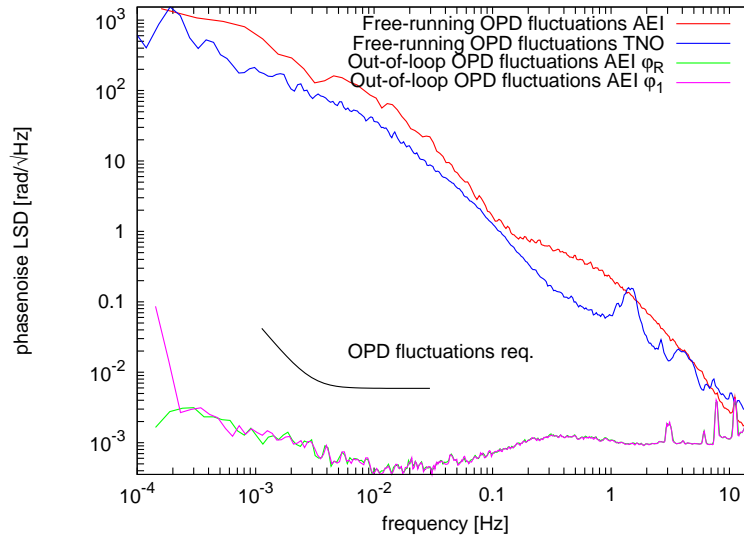
Figure 5.14: Free-running OPD fluctuations measured at AEI-Hannover and TNO and out-of-loop measurement of the stabilised fluctuations, that comply with the requirement.

---

[3]The curves presented in Figure 5.14 are the spectral density of the reference phase φ_R and contain the environmental noise of interferometric components that are not ultra-stable. These curves should not be confused with the performance of the interferometer given by the subtraction $\varphi_R - \varphi_1$ (see Figure 5.15) in which the remaining environmental fluctuations are cancelled.

[4]TNO: Netherlands Organisation for Applied Scientific Research

As a final confirmation of the sufficient noise suppression achieved by the OPD sta-
bilisation, a comparison of the sensitivity of the interferometer and phasemeter system
with and without the OPD stabilisation is shown in Figure 5.15. For the lowest curve
showing the best performance, in addition to the OPD also other stabilisations such as
the amplitude stabilisation presented in Section 5.2 were implemented, as well as other
improvements in the test set-up (faster phasemeter, better vacuum and more stable lab-
oratory environment) with respect to the curve showing the performance without OPD
stabilisation.
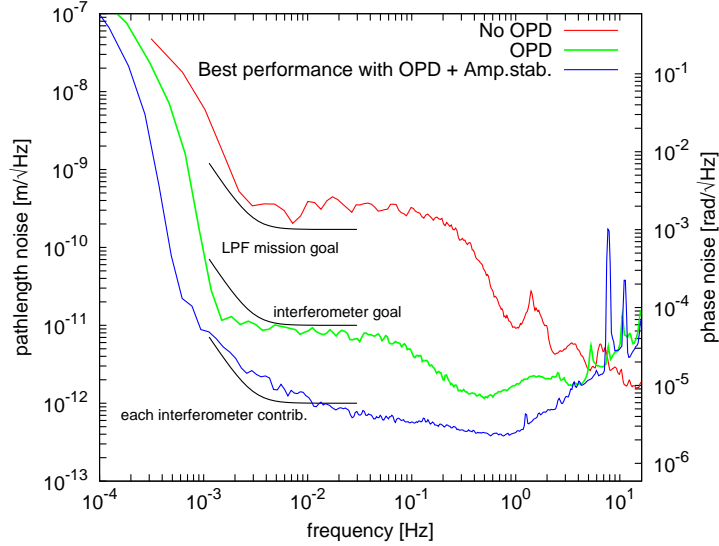
Figure 5.15: Performance comparison with and without OPD stabilisation.

5.4.3. Implementation on-board LTP

Interesting for the implementation of the actuator on-board LTP are the required position
fluctuations, velocity and acceleration fluctuations of the OPD actuator, as this will be
the only moving part of the whole optical metrology system. From the free-running raw
phase linear spectral density $\widetilde{\varphi_R}$ shown in Figure 5.14, the position fluctuations of the
OPD actuator $\widetilde{x}(f)$ can be obtained as

$$\widetilde{x}(f) = \frac{\lambda}{2\pi}\widetilde{\varphi_R}(f). \tag{5.9}$$

The velocity fluctuations $\widetilde{v}(f)$ and acceleration fluctuations $\widetilde{a}(f)$ can be obtained by
successive derivation, i.e. multiplication with s in the Fourier frequency domain:

$$\widetilde{v}(f) = s\,\widetilde{x}(f) \qquad\qquad \widetilde{a}(f) = s\,\widetilde{v}(f) = s^2\widetilde{x}(f). \tag{5.10}$$

The fluctuations for these three quantities are plotted in Figures 5.16, 5.18 and 5.20,
respectively. In order to know the total dynamic range required from the actuator in

terms of displacement, velocity and acceleration, the rms integrate of of each of the three quantities discussed before has to be performed. These three rms integrates are shown in Figures 5.17, 5.19 and 5.21, respectively. They are calculated as the square root of the integration of the square of the corresponding quantity over the frequency, as shown in Equation (5.11) for $x_{\mathrm{rms}}(f)$:

$$x_{\mathrm{rms}}(f_2) = \left(\int_{f_1}^{f_2} \mathrm{d}f \, \tilde{x}^2(f) \right)^{\frac{1}{2}}. \tag{5.11}$$
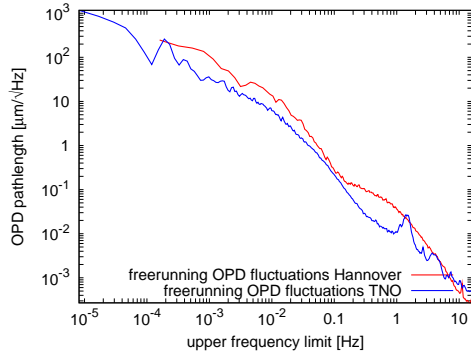
Figure 5.16: Estimated displacement noise caused by the OPD actuator.
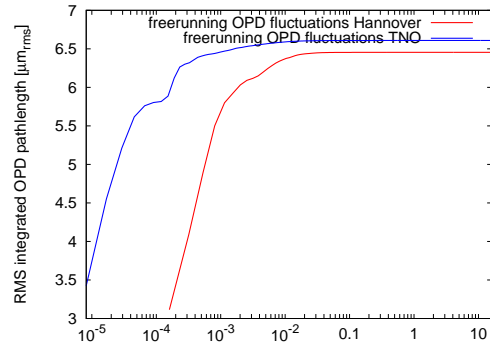
Figure 5.17: RMS-integrated displacement noise caused by the OPD actuator.
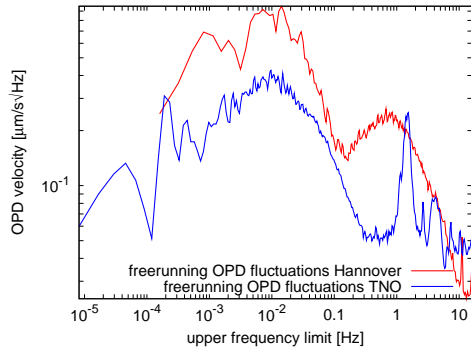
Figure 5.18: Estimated velocity noise caused by the OPD actuator.
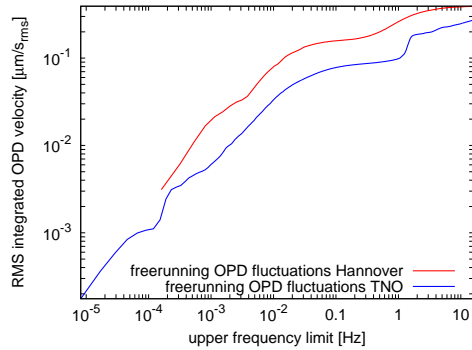
Figure 5.19: RMS-integrated velocity noise caused by the OPD actuator.

From the representation of the rms integrated displacement fluctuations it can be seen that the necessary range for the OPD actuator is given by $\approx 7\,\mu\mathrm{m}_{\mathrm{rms}}$. This has to be considered as an upper limit, as the environmental fluctuations measured on-board LTP are expected to be much smaller than in the two laboratory environments shown in Figure 5.16.

It is also important to discuss the main consequences of the digital implementation of this stabilisation on-board LTP. It is clear that the high UGF of almost 60 Hz presented
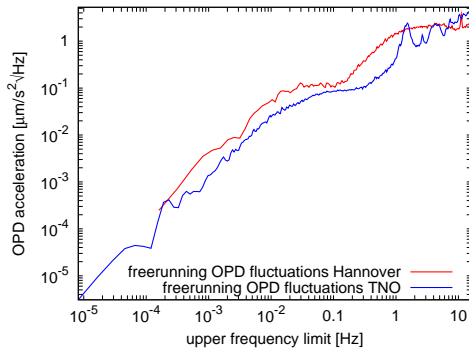
Figure 5.20: Estimated acceleration noise caused by the OPD actuator.
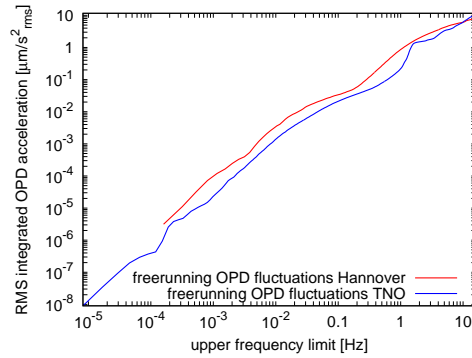
Figure 5.21: RMS-integrated acceleration noise caused by the OPD actuator.

in Figure 5.12 is not achievable with the implementation of the phasemeter (update rate 100 Hz) and back-end processing on-board LTP. Taking into account the different factors such as processing and data transfer between different elements of the LTP optical metrology system, delays in the control loop of up to 25 ms seem realistic [48].

For this purpose, simulations of more aggressive controller designs than the one presented in Figure 5.12 have been done [47] in order to achieve similar gain and noise suppression at low frequencies. For example, by using a $1/f^2$ slope from very low frequencies until 0.3 Hz an OLG shape with sufficient gain can be obtained. Figure 5.22 shows such an open loop gain, assuming a delay of 30 ms in addition to the transfer function of the filter mentioned before. This consideration is also valid for the implementation of the frequency stabilisation, but the lower noise suppression that can be inferred from the measured free-running fluctuations in Figure 5.9 make this concern less critical than for the OPD.

Finally, the scientific output of the measurement of the free-running and stabilised OPD fluctuations on-orbit has to be considered. These OPD fluctuations will be the most accurate measurement of the pathlength noise of single-mode fibres in a quiet space environment and as such will be extremely useful for LISA, where such fibres are essential elements in the baseline architecture. On ground, this phase noise is dominated by environmental influences (such as thermal, seismic or pressure variations) as shown in Figure 5.14. On orbit, these fluctuations should be much smaller, but no reliable estimate of their magnitude and power spectrum is known. Measurement procedures are foreseen in the experiment master plan to gather this important data.

5.5. Noise suppression limitation of the OPD and frequency stabilisation

In the investigations of the OPD and frequency stabilisations presented before it was found that the final sensitivity of the interferometer and phasemeter system presented in
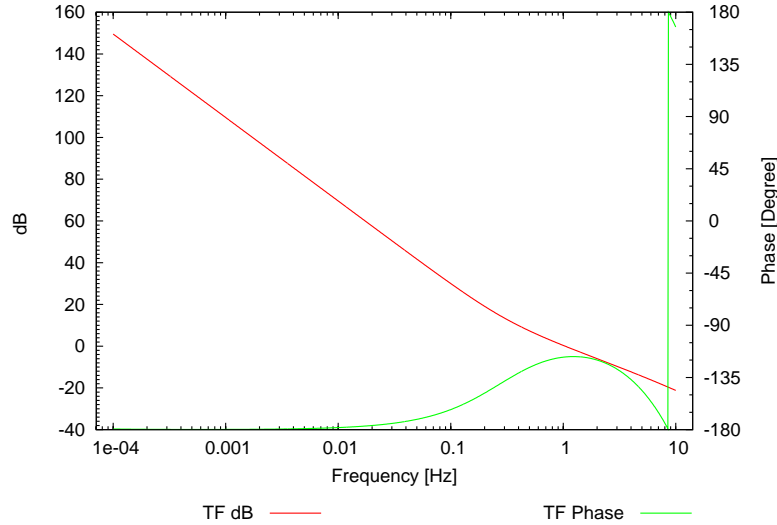
Figure 5.22: Example of an open-loop gain curve for the OPD stabilisation. It achieves enough gain at low frequencies despite the 30 ms delay that has been included in the model.

Figure 5.15 was not limited by residual OPD or frequency fluctuations. It is nevertheless important to know what is actually limiting the performance of these implementations, as they will limit the interferometric sensitivity when the other noise sources have been reduced. These limits are also interesting for potential other applications of the interferometric concept employed in LTP.

The best way to understand the limitations of the implementations is a comparison between the free-running and the stabilised fluctuations of the raw error signals. This is shown in Figure 5.23, where the linear spectral density of the error signals for the OPD stabilisation φ_R and for the frequency stabilisation $\varphi_F - \varphi_R$ are plotted in the free-running and stabilised state.

We can see how both stabilised fluctuations increase at low frequencies until they achieve a comparable level, which indicates that both are limited by the same factor. Specially the stabilised frequency fluctuations show a clear 1/f frequency response below 0.1 Hz. This 1/f noise limits the performance of both stabilisations in the relevant low frequency range, and because of their similar noise level, it is most probably caused by the analog electronics of the servos described in Section 5.3.2 and 5.4.1 which are used for both stabilisations.

This noise level of $\approx 1\,\mathrm{mrad}/\sqrt{\mathrm{Hz}}$ at $1\,\mathrm{mHz}$ is not a concern for the OPD but begins to be harmful for the frequency stabilisation due to its larger coupling factor: both noise sources couple linearly in the phase readout (if the OPD is locked) but with different coupling factors. It is $\approx 1/1000$ for the OPD (as discussed in Chapter 2) and 1/49 or 1/27 for the implementation of the frequency stabilisation discussed here, which is realistic for LTP. This makes the interferometer more sensitive to frequency noise.
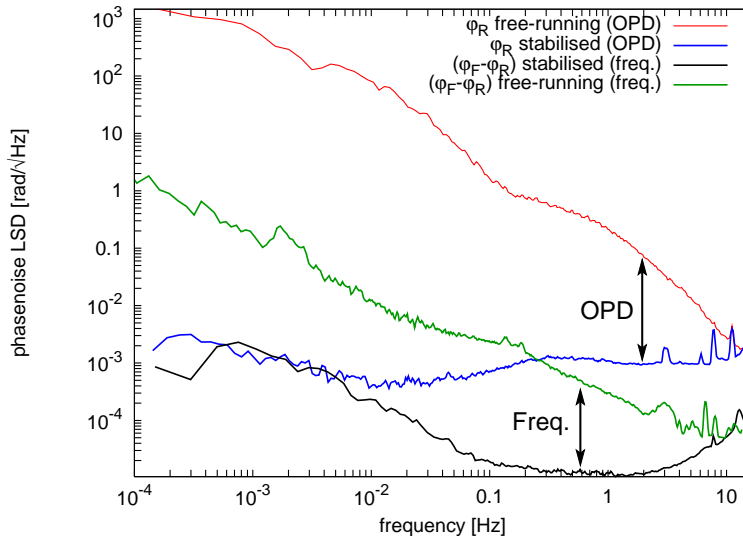
Figure 5.23: Comparison of the fluctuations of the error signals for the frequency and the OPD stabilisation both free-running and stabilised. In the low frequency range, a 1/f noise source limits the performance of both stabilisations.

The different spectral shape of the stabilised fluctuations can be explained by the different free-running fluctuations that each stabilisation has to cope with: the error signal for the OPD φ_R contains environmental fluctuations that are not present in the error signal of the frequency stabilisation $\varphi_F - \varphi_R$, so that the former are much larger, as can be seen in Figure 5.23. This way, the 1/f excess noise shows up more clearly in the stabilised frequency fluctuations, whose intrinsic magnitude would be otherwise much smaller. Note also that the 1/f noise floor common to both stabilised error signals cannot be real pathlength noise: this pathlength noise level of $1\,mrad/\sqrt{\mathrm{Hz}}$ could easily occur outside the optical bench and explain the OPD fluctuations, but not the frequency fluctuations. In order to be responsible for the measured frequency fluctuations, this hypothetical pathlength noise would have to occur on the ultra stable optical bench and would thus be present in the main interferometric performance in Figure 5.15, which is not the case.

This kind of low frequency 1/f noise is a well-known issue of analog electronics, which were chosen for our laboratory implementation due to their simplicity and the comparatively low demanding requirements for LTP. Even though they do not limit the performance of our laboratory demonstration, they will be digitally implemented on LTP. The limitations then will be the update rate and processing delays, as explained in Section 5.4.3.

Finally, a brief summary of the current limitations of our laboratory demonstration of the LTP interferometry can be done following the performance shown in Figure 5.15 and dividing the spectrum in 3 separate frequency ranges:

high frequency range (f > 1 Hz**):** the performance is limited by mechanic perturbations of the structure supporting the EM OB inside the vacuum tank shown in Figure 2.13, mainly driven by the vacuum pumps. This can be seen from the sharp resonances,

which change with any modification of the OB mechanical settling. This frequency range is not relevant, as it is outside the LTP frequency range and these kind of perturbations are by no means expected in the LTP environment.

medium frequency range ($10\,\mathrm{mHz} < \mathrm{f} < 1\,\mathrm{Hz}$**):** the performance is limited by specific phase measurement noise and not by pathlength noise. The main noise source would be the effective digitalisation noise, which takes into account not only the nominal digitalisation noise of the phasemeter but also the dynamic range of the photodiode signals, affected by the interferometric contrast and alignment. In this sense, this is the frequency range of most variable performance but at the same time the most sensitive, well below the specifications.

low frequency range ($f < 10\,\mathrm{mHz}$**):** this frequency range is limited by temperature driven pathlength fluctuations on the optical bench. This kind of low frequency pathlength noise was already reported [27] in the monolithic Glasgow optical bench and can be seen in the performance shown in Figure 5.10. The coupling is even more critical in our experimental set-up, which follows the realistic LTP optical layout and uses dummy mirrors acting as test masses. These adjustable mirrors are set on metallic mounts that make the interferometer more sensitive to temperature changes. The best strategy to perform realistic long-term tests at the required sensitivity has been the passive stabilisation of the environmental conditions around the optical bench described in Chapter 2 which allowed the temperature stability of $\approx 10^{-4}\,\mathrm{K}/\sqrt{\mathrm{Hz}}$ at $1\,\mathrm{mHz}$ shown in Figure 7.23.

5.6. Fibre-coupled implementation of the OPD stabilisation

When the necessity for an OPD stabilisation was discovered, several designs for an OPD actuator were studied. A fibre-coupled OPD actuator was reported by the IGR LTP group [27]. This stabilisation was based on a heating wire wound around a fibre segment and was used during the noise investigations campaign that the LTP teams of AEI and IGR conducted in Glasgow [26], as described in Section 5.3. In this campaign the AEI phasemeter was tested for the first time with a monolithic optical bench —the Glasgow prototype— and the first performance curve below the $10\,\mathrm{pm}/\sqrt{\mathrm{Hz}}$ specification was measured, as shown in Figure 2.17.

Already during the campaign it became clear that a temperature based actuator would be too slow for the requirements of the OPD stabilisation, as shown in Figure 5.24, where the best performance during the measurement campaign with heater and with a free-beam PZT implementation of the OPD stabilisation are compared.

This motivated the investigations presented in this chapter on a fibre-coupled phase actuator with higher bandwidth than a system based of temperature actuation and space qualifiability in mind.
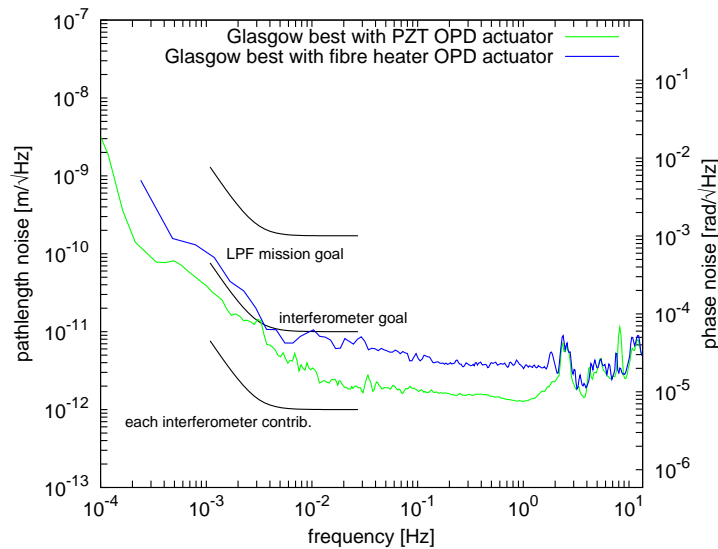
Figure 5.24: Interferometric performance measured with the Glasgow OB prototype with two different OPD implementations: free-beam and fibre-coupled.

5.6.1. Requirements

The requirements for the fibre-coupled OPD actuator derive from the tests performed with the free-beam configuration and can be summarised as follows:

- **Dynamic range:** It must be possible to change the optical pathlength by about $30\,\mu$m.
- **Bandwidth:** The requirement calls for $20\,$Hz actuator bandwidth. This is sufficient for a loop bandwidth of a few Hz, which will be actually limited by phasemeter delays as discussed in Section 5.4 and stated in [47].
- **Spurious effects:** It is also important to investigate whether any other property of the laser beam apart from the optical pathlength is modified by the actuator. Although we could measure such effects as polarisation change thanks to our very sensitive equipment, the effects are small and of no practical impact for LTP.

5.6.2. Description of the actuator

Three actuators as the one shown in the right part of Figure 5.25 were assembled. Each consisted of a single-mode, polarisation-maintaining optical fibre wound and glued around a PZT using epoxy adhesive. The ceramic ring PZT was a cylinder of about $10\,$cm outer diameter, $9\,$cm inner diameter and $3\,$cm height, as can be seen on the left part of Figure 5.25. It had a nominal capacitance of $22\,$nF.

The principle of operation of the actuator is as follows: due to its piezoelectric nature, changes in the potential difference between the inner and outer surfaces of the ring cause
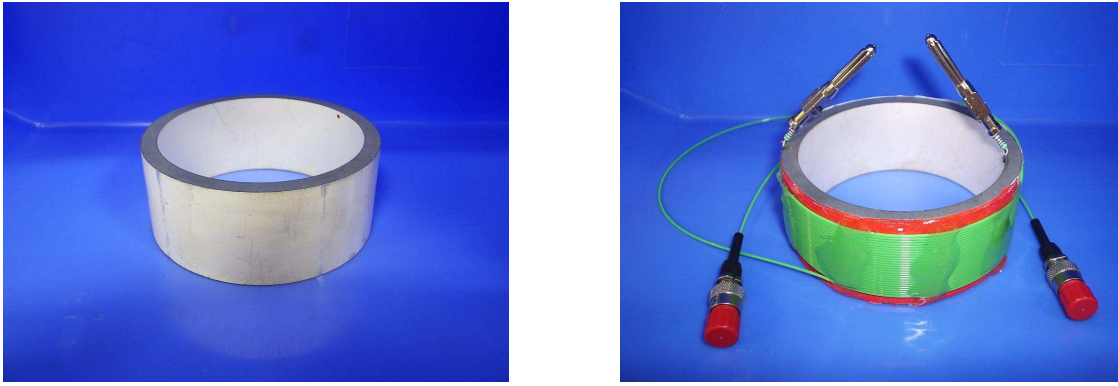
Figure 5.25: Naked piezoelectric ring (left) and assembled actuator prototype (right) with an optical fibre glued around the PZT ring.

structural expansion. This stretches the optical fibre, thus changing the optical path-length experienced by the light [49, 50].

In order to apply a potential difference to the PZT ring, one connector was soldered on each side, as well as a resistor of 50 kΩ to limit the current, as shown in Figure 5.25. This way, a control voltage could be applied from a voltage driver with a dynamical range of ± 400 V.

5.6.3. Efficiency and bandwidth

A homodyne Mach-Zehnder interferometer was built with one prototype actuator in one arm to test the efficiency of the actuator. Figure 5.26 shows the experimental set-up in the laboratory and a schematic representation of the actuator as part of the interferometer. The signal measured by a photodiode placed at one output port of the interferometer is
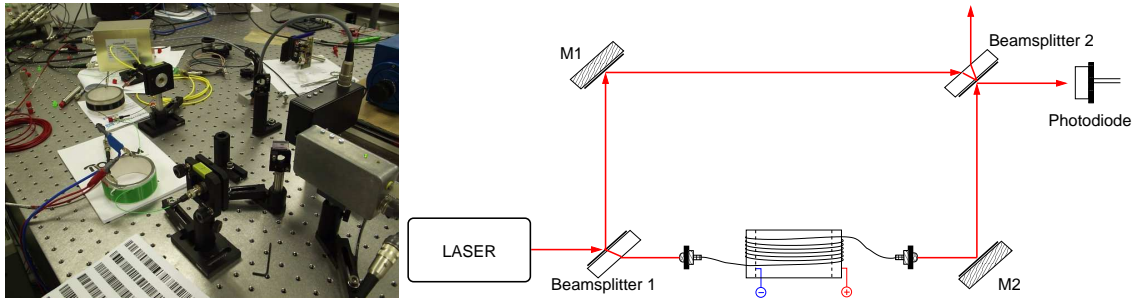
Figure 5.26: Table top homodyne interferometer to measure the efficiency and bandwidth of the actuator.

proportional to the light power and can be written as:

$$V_{\mathrm{PD}} = A(1 + C \cos(\frac{2\pi \Delta s}{\lambda}))$$ (5.12)

where C is the contrast of the interference, Δs the optical pathlength difference between the two arms of the interferometer, λ the wavelength of the laser (1064 nm in our case), A is the amplitude of the signal. By applying a ramp to the PZT actuator one can change the pathlength of the fibre. For a 1064 nm pathlength difference the intensity at the output of the interferometer will go through one full cycle (fringe). Figure 5.27 shows the result of such a measurement from which the efficiency of our actuator can be estimated as η=0.09 μm/V $_{\text{PZT}}$. From this efficiency and the dynamic range requirement of 30 μm mentioned in Section 5.6.1, a maximal actuation voltage V_{MAX} of

$$V_{\text{MAX}} = \frac{30 \,\mu\text{m}}{0.09 \,\mu\text{m}/\text{V}_{\text{PZT}}} \approx 330 V_{\text{pp}} \tag{5.13}$$

can be estimated. This assumes a fibre actuator of 7 m in one arm. This maximal voltage would be smaller in normal LTP operation, as one OPD actuator in each arm is foreseen.
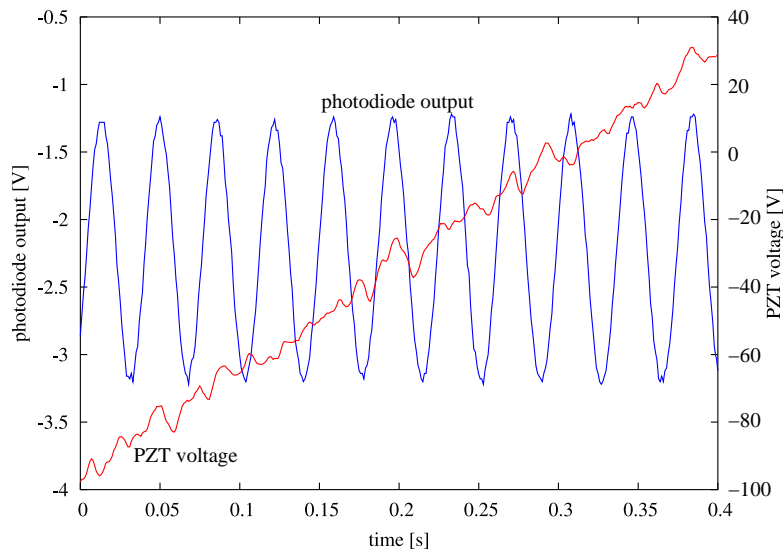
Figure 5.27: Efficiency of the actuator. Each fringe corresponds to $\lambda = 1064$ nm change in the pathlength.

As mentioned in Section 5.6.1, three different devices were built using PZT rings with identical properties to test the reproducibility of the assembly procedure. The properties of the fibres were also identical apart from the length: one of them was 4 m long and the other two 7 m. The glue used was also always the same but in different quantities, the shorter fibre being only glued with three strip-like contact surfaces and the longer fibres with more homogeneous glue distributions. Nevertheless, all three actuators behaved very similarly and showed a very comparable efficiency per meter of fibre. Using the whole range of the driver, the 4 m long fibre accomplished about 24 μm and the 7 m long about 43 μm pathlength change.

To measure the bandwidth of the actuator the homodyne interferometer was locked to

mid-fringe. This OPD stabilisation works in the same way as in the LTP interferometer except that no heterodyne phase detection has to be done, which simplified the test bench. It kept the interferometer output in the the linear region of the sinus function in Equation 5.12. This allowed the measurement of the transfer function with the experimental set-up shown in Figure 5.28: a perturbation signal was injected in the control loop with the analog electronic adder while a network analyser was used to measure the transfer function from feedback signal to error signal.
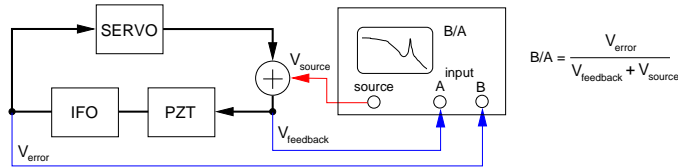
Figure 5.28: Experimental procedure for the measurement of the transfer function of one OPD actuator.

Although this measurement configuration showed a poor signal to noise ratio at low frequencies, it delivered directly the transfer function and was thus more reliable than only dividing by the injected perturbation. Figure 5.29 shows the measured transfer function together with a fit to the data done with LISO [4]. This fit allowed the quantification of the main characteristics of the function, which in this case were a simple pole at about 130 Hz and a complex pole at 15 kHz with a quality factor of Q = 356.
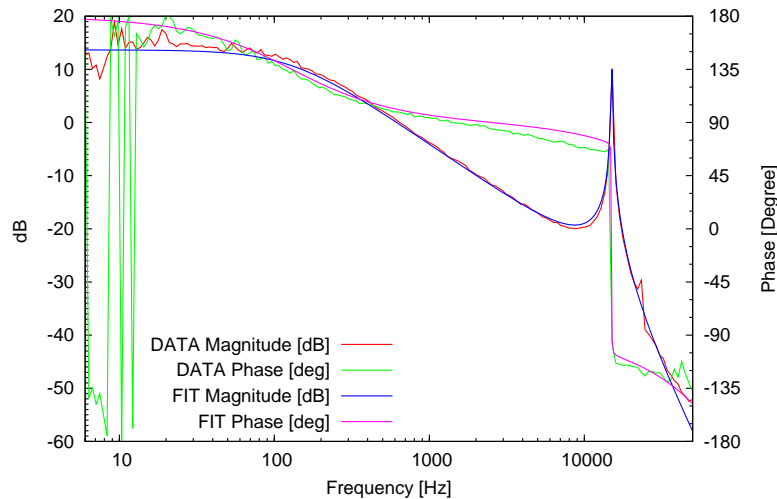
Figure 5.29: Actuator transfer function. The low pass behaviour is given by 22 nF internal capacitance of the PZT and the 50 kΩ serial resistance used to apply the voltage.

The first pole accounts for the low pass behaviour and has its origin in the RC combination of the internal capacitance of the PZT (22 nF) and the series resistor (50 kΩ). The nominal corner frequency of this RC element is 144 Hz, very similar to the measured 130 Hz. This means that this first pole is no fundamental limitation for the bandwidth of the actuator,

which is anyway already sufficient for the requirements of the OPD stabilisation. The complex pole accounts for the mechanical resonance of the PZT. This is far enough from the interesting frequency range of at most 20 Hz, so that its influence in the stabilisation can be easily suppressed by a proper servo design which lets the gain roll off strongly after the unity gain frequency.

5.6.4. Intrinsic amplitude modulation

For this measurement laser light of constant power was coupled into the fibre and directly measured with a photodiode at the output, without any interferometer as can be seen in Figure 5.30.
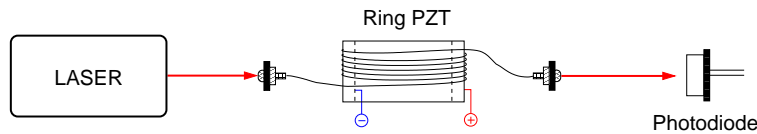
Figure 5.30: Configuration of a prototype to measure its transmittance shown in Figure 5.31.

The PZT voltage was ramped from rail to rail to check for a possible variation of the fibre transmission. The result of the measurement is plotted in Figure 5.31, with the time in the x-axis, the photodiode output on the left y-axis and the driver voltage on the right y-axis. The blue curve shows how the driver voltage was ramped over the whole dynamic range while the red curve shows no significant correlated variation of the photodiode output.
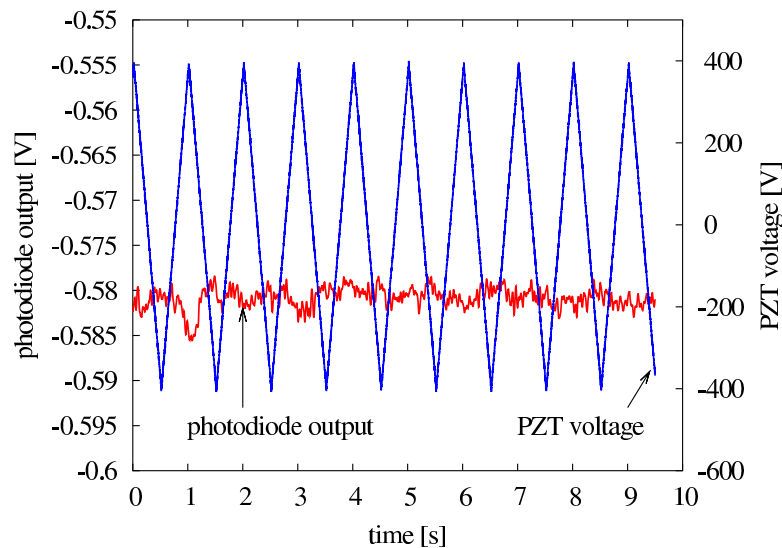
Figure 5.31: Transmittance of the fibre against control voltage applied to the PZT. No measurable influence.

5.6.5. Rotation of the polarisation plane and appearance of circular polarisation

The next issue to investigate was whether the stress induced in the fibre by the PZT changed the polarisation state of the propagating light. The direct consequence of a change in the polarisation would be a proportional variation of the light intensity injected into the optical bench due to the polarisers present just after the fibre injectors. This intensity variation could be then corrected by the amplitude stabilisation which is already foreseen but a quantification of the effect needed to be done.

For this purpose, the experimental setup shown in Figure 5.32 was implemented. In this set-up, the laser beam was transmitted through a polarising beam splitter (PBS1) before it was coupled into the actuator. Another PBS (PBS2), which can be rotated by means of a step motor was placed at the output. The angle of rotation can be very precisely determined [51] with a dedicated readout procedure based on a LED signal that is reflected off a reflectivity-modulated pattern on the polariser mount while it rotates. Each time the second PBS rotates by 180 degrees a minimum in the transmitted light occurs and its value would be zero in the ideal case of linearly polarised light.
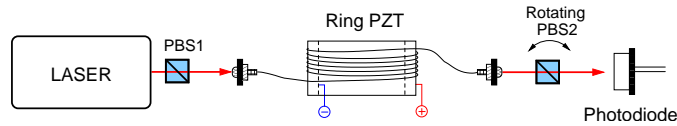
Figure 5.32: Experimental set-up for detection of changes in the polarisation state of light propagating through the OPD actuator. PBS2 rotates while the control voltage at the PZT is modulated.

By measuring the angle where these minima occur and their extinction ratio at different control voltages, we can derive the influence of the actuator on the polarisation state of the light: if the polarisation plane changes, the angle at which the minimum takes place will also change and appearance of circular polarisation will make the minima different from zero.

The result of such a measurement is shown in Figure 5.33, with the control voltage on the x-axis, the extinction ratio on the right y-axis and the rotation of the polarisation plane on the left y-axis.

There is a rotation of the polarisation plane of about 7 degrees along the 800 V dynamical range of the driver. This would cause a change of 1.5 % in the intensity injected in the LTP optical bench, which could be easily compensated by the foreseen amplitude stabilisation. Note that by using one of the 7 m long fibres in each arm, the requirement of 30 μm pathlength change would be fulfilled with less than half of the dynamical range of the used driver.

On the other hand, there is a strange behaviour of the extinction ratio, which seems to be better if voltage is applied than when not, contrarily to our expectations.
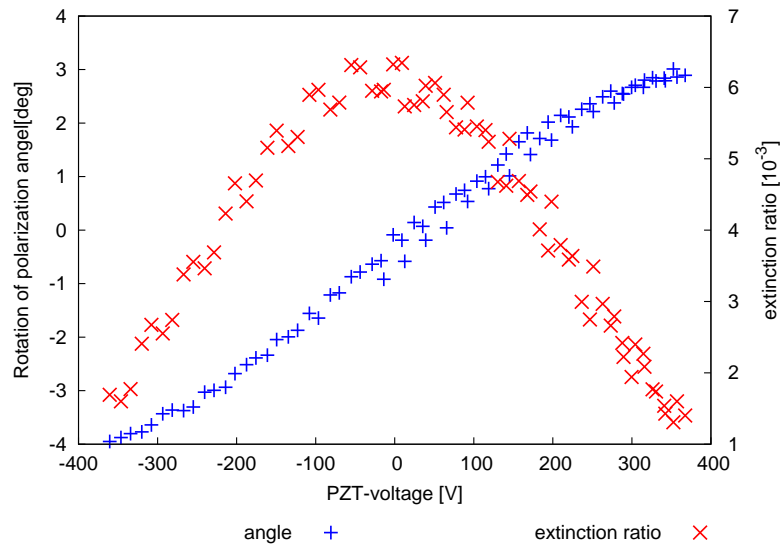
Figure 5.33: Rotation of the polarisation plane and appearance of circular polarisation at different control voltages.

An explanation for this can be found in the construction properties of the used fibres, which are worth being investigated due to their similarity to the ones planned for the use for LTP.

The principle of operation of the polarisation maintaining optical fibres is based on the intentional birefringence in the core of the fibre. The asymmetry of the core has its origin in the stress-inducing structures to be found in the cladding, and as can be seen in the section of a fibre shown in Figure 5.34, linear polarised light coupled into the slow axis of the fibre maintains its polarisation and is also insensitive to environmental stress.
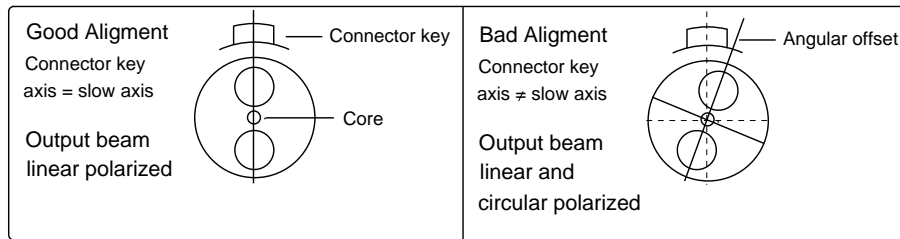
Figure 5.34: Section of a polarisation maintaining fibre. Light coupled into the slow axis of the fibre propagates optimally. Source: Schäfter+Kirchhof

To study the effect of an offset angle between the polarisation plane of the incoming light and the slow axes of the fibre, the experimental set-up shown in Figure 5.35 was implemented. It is a modification of the set-up shown in Figure 5.32: it includes a half wave plate (HWP) after the first polariser, which makes it possible to change the incoming polarisation plane without changing the transmitted amplitude or the beam position (which would in turn change the coupling efficiency), as a PBS would do. This way, it is

possible to independently change the polarisation plane and the incoming intensity.
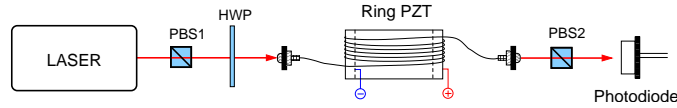
Figure 5.35: Experimental set-up to study the misaligning of the polarisation plane of incoming light and the slow axes of the fibre. Maintaining a fixed alignment configuration, variations in the transmittance of the fibre are monitored while the control voltage is modulated.

Figure 5.36 shows the fluctuations in the transmittance of the fibre, calculated as the changes in the output of the photodiode normalised to the mean intensity, while the control voltage was varied over its complete dynamic range. Although the control voltage is not plotted on the graph for the sake of clarity, it is clearly visible from the periodicity of the transmittance variations that the control voltage was driven with a triangular function of period 100 ms.
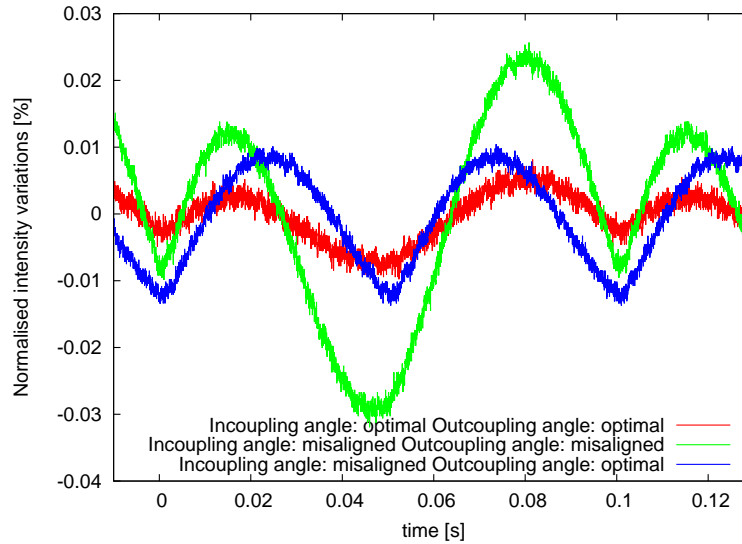
Figure 5.36: Normalised changes in the transmittance of the fibre as the control voltage is modulated for three different configurations of PBS1 and PBS2.

A careful analysis of the obtained data has to be done in order to come to valid conclusions:

- The first curve shows the optimal configuration in which the transmittance variations are minimal. The HWP makes the incoming polarisation plane parallel to the slow axes of the fibre and PBS2 is aligned with the out-coming polarisation.
- For the second curve, the HWP is slightly rotated so that the angular offset described in Figure 5.34 appeared and the fluctuations were maximal, because not only the incoming polarisation plane was misaligned with respect to the fibre, but also the out-coming polarisation plane was misaligned with respect to PBS2.
- For the third curve, PBS2 was intentionally misaligned with respect to the fibre so that it matched the polarisation angle of the out-coming light. This decreased the

fluctuations, but due to the persistent misalignment of the HWP, they were not as small as in the first curve.

The exact location of the minima with respect to the control voltage also changed in the different configurations, which explains the strange behaviour observed in Figure 5.33.

5.7. Conclusions

We have analysed the implementation of three stabilisation techniques and their influence on the final sensitivity of the LTP interferometry. The main noise source to be stabilised consists of the non-linearities detected at the interferometric output and caused by electromagnetic pick-up from the modulation electronics [28]. The influence of this non-linearities can be suppressed by stabilising the environmental pathlength difference fluctuations that affect all four LTP interferometers.

The implementation of the frequency and OPD stabilisation was analysed based on out-of-loop measurements of the residual stabilised fluctuations, which will be also available with the designed LPT data handling. These measurement show that the remaining OPD noise remains well below the specs. In the case of the frequency stabilisation, the achieved noise suppression is limited by low frequency noise of the analog electronics implementation of the stabilisation but does not influence the main interferometric readout.

The implementation of the amplitude stabilisation with high gain at the heterodyne frequency f_{het} reduces the observed amplitude modulation on each beam and improves thus the phase readout performance. The only eventual limitation of the technique is the acoustic delay in the AOM crystals that limits the loop bandwidth and gain.

The implementation of frequency noise subtraction as fall-back option in case of stabilisation failure was also presented. The inaccuracy in the determination of the calibration factors for the subtraction limits the achievable noise reduction, making thus the active stabilisation the preferred technique.

The implementation of these techniques on-board LTP will also help to gather essential information for LISA about the fluctuations under study: frequency and amplitude stability of the laser and pathlength stability of optical fibres.

Finally, a fall back option for a fibre-coupled actuator for the OPD stabilisation was presented. The observed unwanted effects on light properties, which have been measured under worse conditions than the ones expected for the LTP, could be easily compensated by the amplitude stabilisation present on the optical bench. Additionally, it was experimentally confirmed that when coupling a laser beam into polarisation maintaining fibres special care must be taken in aligning the polarisation plane of the light parallel to the slow axis of the fibre. A proper alignment ensures polarisation conservation and reduces the influence of mechanical stress in the beam propagation. This is of relevance for both LISA and LTP, as all the interferometric beams are brought to the optical bench via this kind of fibres.

Chapter 6.

Frequency stabilisation by locking to a LISA arm: first results on a hardware model

The traditional approach used in ground-based gravitational wave detectors to stabilise the laser frequency takes the average length of the interferometer arms as a reference (in particular, the power recycling cavity). The LISA arms are good candidates for this technique due to their exceptional stability in the relevant frequency range, but the round-trip travel time between two satellites of 33 s was long considered an insurmountable limitation. The control bandwidth of this kind of loop is typically limited to frequencies well below the inverse of this delay [52], but LISA requires noise suppression at frequencies up to several orders of magnitude higher. Some groups (first [53], confirmed by e.g. [54, 55]) have come up with the theoretical background and simulations of novel control schemes that achieve the necessary bandwidth and gain, which has been called "self-phase-locked delay interferometry" or more commonly "arm-locking".

This chapter presents the first experimental demonstration of this technique, using an electrical model of the system. The LISA laser was substituted by a voltage controlled oscillator (VCO), and a delay of $\tau = 1.6\,\mu s$ was implemented by 300 m of coaxial cable. Noise suppression was demonstrated at frequencies above $1/\tau$.

In order to investigate the oscillator behaviour independently from the control loop, the signal was directly sampled and processed to extract its phase. This way, the predicted noise suppression in the frequency domain was confirmed. In the time domain, a quasi-periodic, exponential decaying transient that was predicted to appear just after the lock acquisition [53, 56] was also experimentally confirmed. Furthermore, its initial amplitude was reduced when the loop was closed by ramping up the gain instead of abruptly switching it on. Finally, the actual limiting factor for the noise suppression that can be achieved in the implementation of this control scheme for LISA was identified.

6.1. Introduction

The optical pathlength fluctuations δs caused by position fluctuations of the LISA test masses are determined by the phase fluctuations $\delta\varphi_{\text{int}}$ of the beat note at the interferom-

eter output:

$$\delta\varphi_{\text{int}} = \frac{2\pi}{\lambda}\delta s. \tag{6.1}$$

As in any other interferometer, laser frequency fluctuations couple linearly in the phase through the static length difference between two LISA arms ΔL. This can be seen by writing the interferometric phase φ_{int} as the differential phase shift between two interferometer arms

$$\varphi_{\text{int}} = \frac{2\pi}{\lambda}\Delta L = \frac{2\pi\nu}{c}\Delta L \tag{6.2}$$

and studying the effect of frequency variations $\delta\nu$, assuming that they are slow and the armlength difference ΔL is static [2, 11]:

$$\delta\varphi_{\text{int}} = \frac{2\pi\Delta L}{c}\delta\nu. \tag{6.3}$$

With these conditions, a fluctuation of the laser frequency $\delta\nu$ causes an apparent pathlength noise δs given by:

$$\widetilde{\delta s} = \frac{\widetilde{\delta\nu}}{\nu}\Delta L. \tag{6.4}$$

LISA will need extraordinary laser frequency stability to detect position fluctuations in the range of picometres. In this chapter we analyse the baseline strategy to achieve the required frequency stability and demonstrate the principle of function of one of the necessary core technologies.

6.2. Laser frequency stability for LISA

The orbits of the LISA satellites have been carefully chosen to keep the arms as stable as possible in the measurement band, but armlength variations of up to $50000\,\text{km}$ [11] will still occur. These variations are caused by orbital mechanics in the solar system and have frequencies of a few per year, but no components in the LISA band. This quasi-static armlength mismatch will cause the coupling of laser frequency noise into the interferometric phase, as shown in Equation (6.4). Considering a noise allocation of $1\,\text{pm}/\sqrt{\text{Hz}}$ for the pathlength detection noise induced by frequency fluctuations, a very stringent frequency stability of $5.6 \cdot 10^{-6}\,\text{Hz}/\sqrt{\text{Hz}}$ is required, as can be deduced from Equation (6.4).

The current approach to achieve such a high noise suppression consists of a combination of three stabilisation techniques. Figure 6.1 depicts the resulting stability after the application of each technique: the upper curve shows the free-running noise of a space-qualified laser prototype as measured at the AEI laboratories, with a noise level of $10^7 \, \mathrm{Hz}/\sqrt{\mathrm{Hz}}$ at $1 \, \mathrm{mHz}$. As a typical simple approximation, the next curve below represents the noise level $10^4 \frac{\mathrm{Hz}}{\sqrt{\mathrm{Hz}}} \left[\frac{f}{1 \, \mathrm{Hz}} \right]^{-1}$. The third curve from the top is the remaining noise after applying a pre-stabilisation consisting in locking the laser frequency to an ultra-stable reference cavity [44] with the Pound-Drever-Hall [46] method. This technique is expected to achieve a flat noise level of $30 \, \mathrm{Hz}/\sqrt{\mathrm{Hz}}$ down to 3 mHz and increases as $1/f^2$ to lower frequencies. The fourth curve from the top represents the predicted noise level after the application of "arm-locking" [53, 57, 58, 59, 60], the technique discussed in this chapter. Finally, time-delay interferometry (TDI) [61, 62] is implemented to achieve the required $5.6 \cdot 10^{-6} \, \mathrm{Hz}/\sqrt{\mathrm{Hz}}$ stability level. It consists of a post-processing technique that cancels frequency induced phase noise by combining the phase output of different LISA arms delayed by travel times corresponding to armlength mismatch which has to be estimated with DNS[1] measurements of the satellite positions or from inter-spacecraft ranging information modulated on the laser beams. This way, LISA interferometric combinations are synthesised with a virtual armlength mismatch limited only by the accuracy of the estimated delays. Note that the cavity pre-stabilisation and arm-locking physically stabilise the laser frequency, while the stability achieved by TDI is a virtual quantity.
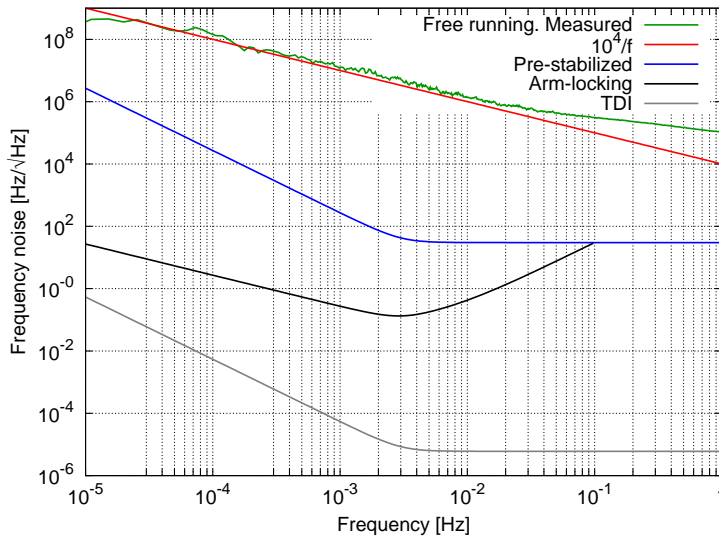
Figure 6.1: Frequency noise level required at each of the three stabilisation stages that will be combined to achieve the LISA goal. The two upper curves (green and red) are the measured and expected free-running level, respectively. Next one (blue) represents a pre-stabilised laser, then after using arm-locking (green) and TDI (magenta). Source for the requirements: EADS Astrium.

---

[1]The NASA Deep Space Network (DSN) is an international network of antennas that supports interplanetary spacecraft missions. It is planned that DSN will support LISA.

6.3. Arm-locking for LISA

The principle of arm-locking [58] is shown in Figure 6.2 with a simplified scheme of a LISA arm. A laser beam with frequency fluctuations is split into two paths: the "prompt" path goes directly to a photodetector. The "delayed" path is sent to a distant satellite[2] and comes back to the local photodetector after the round-trip time of $\tau = 33\,s$. The phase difference between both interfering laser φ_{int} is measured with a phasemeter. This way, φ_{int} is the output phase of a Mach-Zehnder *interferometer* with an armlength mismatch ΔL of twice a LISA arm ($10^7\,$km), thus extremely sensitive to frequency fluctuations, as stated in Equation (6.4). This sensitivity to frequency fluctuations makes φ_{int} an useful error signal for a frequency stabilisation, which can be transformed by a servo into a feedback signal and fed to the laser frequency control input.
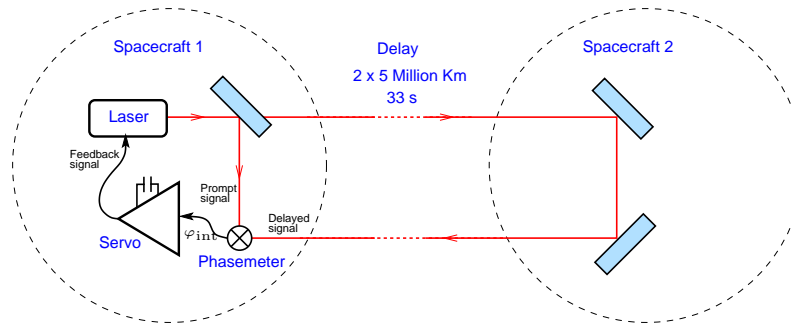
Figure 6.2: Simplified scheme of a LISA arm to illustrate the principle of operation of arm-locking.

In this sense, arm-locking can be understood as using an interferometer with a huge armlength difference (twice the LISA armlength) as "noise sensor interferometer" to stabilise the frequency noise, so that the latter does not affect the sensitivity of the "measurement interferometer", that has a much smaller pathlength mismatch (1% of the LISA arm). In our explanation the "sensor interferometer" is formed by a single LISA arm and the "measurement interferometer" is any LISA interferometric combination, e.g. the "Michelson" [61] combination formed by two adjacent arms. The same approach of a "noise sensor interferometer" and "measurement interferometer" is used in the LTP interferometry, as presented in Chapter 5, but the intentional armlength mismatch is only about 35 cm and the corresponding light travel time ($\approx 1\,$ns) does not influence the loop behaviour, since its bandwidth is limited by the update rate of the phasemeter to frequencies well below 100 Hz.

In early formulations of the LISA mission [2] the strategy for frequency stabilisation did not explicitly include an active stabilisation using one arm as a length reference for the laser frequency. It was assumed that the delay ($\tau = 33\,$s) caused by the round-trip travel time would limit the stabilisation bandwidth to frequencies well below $1/\tau \approx 30\,$mHz, while the relevant frequency at which significant noise reduction is needed goes up to

---

[2]The transponder function of the distant satellite (via an offset phase lock) is neglected in this simplified picture. It will be regarded as a perfect mirror that compensates for the power lost on the way.

1 Hz.

But as will be shown in this chapter, this limitation happens only in control loops without any split path, where a signal necessarily accumulates a pure delay τ^* after going once around the loop, as depicted in Figure 6.3. This is not the case of arm-locking, where the "detection" delay τ affects only the "delayed" path while the "prompt" path delivers current information of the oscillator noise.
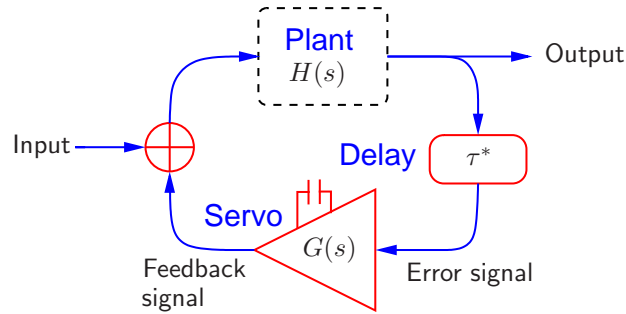
Figure 6.3: Conventional control loop. *As opposed to arm-locking*, in the absence of a split path every signal inside the loop accumulates a delay $\tau*$ after one cycle. This limits the control bandwidth frequencies well below $1/\tau^*$.

In LISA, the actual situation is as shown in Figure 6.4. The plant of the loop consists of an oscillator whose signal is split into two paths, the phase difference of which is measured. This phase constitutes the error signal to stabilise the oscillator frequency, just as in LISA. Of course, processing delays of the type τ^* can also be present in the system and will indeed limit the bandwidth to a fraction of $1/\tau^*$ as will be discussed later.
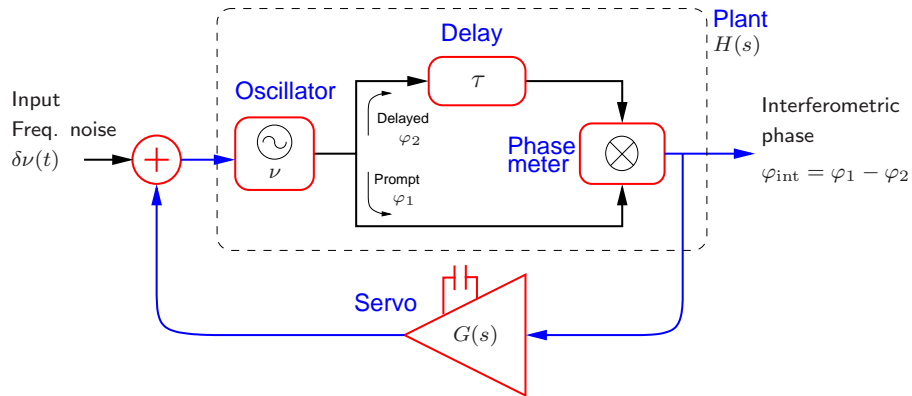
Figure 6.4: Functional scheme of arm-locking: the signal is split in two paths and only one of them contains the delay τ. The "prompt" (non-delayed) signal allows a stabilisation bandwidth higher than $1/\tau$.

Table 6.1: Correspondence between the LISA properties relevant for the experiment and our prototype

	LISA	Prototype
Oscillator	Laser	VCO
Delay τ	33 s	$1.6\,\mu$s
$1/\tau$	30 mHz	625 kHz
freq. range	0.1 mHz 1 Hz	2 kHz 20 MHz

6.4. Characterisation of the experimental simulation of arm-locking

6.4.1. Elements of the experimental setup

In order to test the characteristics of a control loop like arm-locking, an experimental simulation was implemented. Its main components and features are depicted in Figure 6.5 and summarised in Table 6.1. They can be described as follows:

Oscillator: Instead of a laser we use a VCO working at a nominal frequency of 72 MHz. It allows a hardware simulation of the control scheme without the complications of optical components. The VCO has also very low intrinsic noise, so that noise with a controlled amplitude and spectral shape can be introduced in the control loop via the adder depicted in Figure 6.5. In addition, the low frequency of the VCO allows to sample its signal directly and determine its phase noise independently of the control loop, as will be explained in section 6.5.

Delay: After being split, one of the signals is delayed by $1.6\,\mu$s with 300 m low-loss coaxial cable instead of the 33 s round-trip time between two LISA satellites. The frequency inverse of the delay is given by 625 kHz. One aim of the experiment presented here is to prove that this frequency does not limit the stabilisation bandwidth, as opposed to the type of loop shown in Figure 6.3.

Phasemeter: A mixer followed by a low-pass filter is used to measure the phase difference between the prompt and the delayed signal. The oscillating signals at the two input ports of the mixer are multiplied with each other, so that the resulting DC voltage is proportional to their phase difference (when the two inputs are nearly in quadrature) and the low pass filter suppresses the tones at 72 MHz and harmonics. An independent phasemeter was also implemented for the noise measurements presented in Section 6.5, where its principle of function will also be explained.

Relevant frequency range: The LISA measurement band, where significant frequency noise suppression is necessary, goes from 0.1 mHz to 1 Hz, encompassing 30 times the round-trip inverse frequency of 30 mHz. The corresponding frequency range for our prototype, where the frequency inverse to the delay is 630 kHz goes from 2 kHz to 20 MHz.
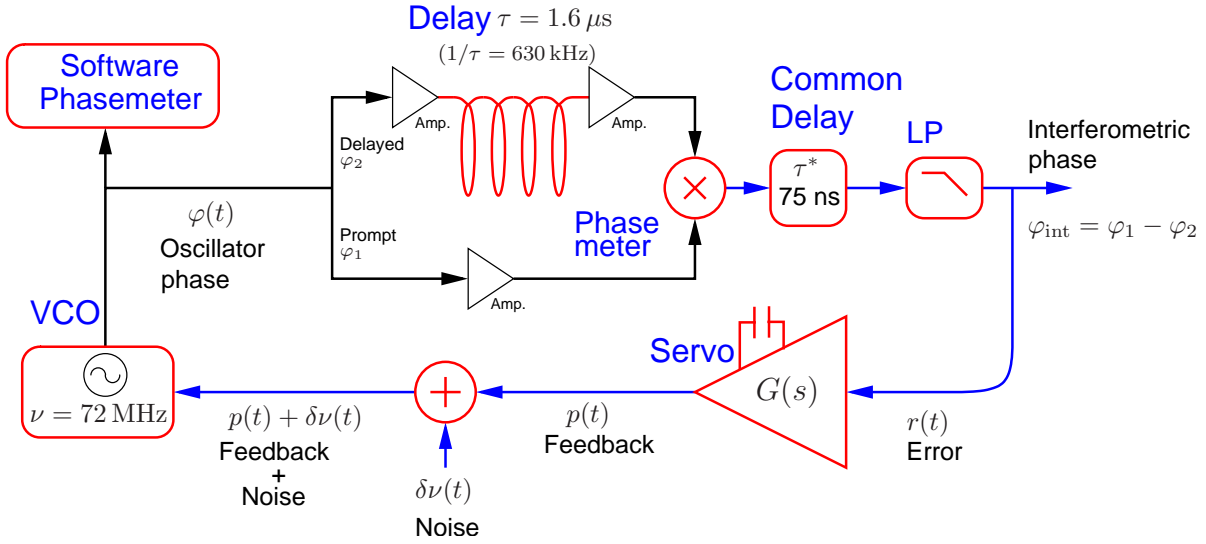
Figure 6.5: Detailed scheme of the table-top hardware simulation of arm-locking.

6.4.2. Notation: frequency, phase, Fourier frequency and interferometric phase

In this chapter, the words frequency and phase are used profusely and sometimes with very different meanings. Now that the main elements of LISA regarding laser frequency noise have been presented as well as their equivalents in our experimental demonstration, this section presents the distinctions between the different frequencies and phases that will be used from now on.

Fourier frequency: LISA will be sensitive to gravitational waves in a very specific frequency range, from $0.1\,\mathrm{mHz}$ to $1\,\mathrm{Hz}$. Consequently, the fluctuations of any magnitude or the performance of any stabilisation will be investigated in this Fourier frequency domain. The Fourier frequency will be expressed as f and measured in Hz or as the angular frequency $\omega = 2\pi f$ and measured in rad/s. Any function in the Fourier frequency domain will be written in capitals and its linear spectral density (LSD) will be indicated with a tilde [63].

Oscillator properties: the frequency of the LISA laser or the VCO will be called ν and its phase φ. The phase is the time integral of the frequency. In the Fourier frequency domain they are related by

$$\nu(\omega) = \mathrm{i}f\varphi(\omega) = \mathrm{i}\frac{\omega}{2\pi}\varphi(\omega). \tag{6.5}$$

The interferometric phase φ_{int} measures in general the difference between the two interferometric arms:

$$\varphi_{\mathrm{int}} = \frac{2\pi\nu}{c}\Delta L. \tag{6.6}$$

Fluctuations of the laser frequency ν couple linearly in the interferometric phase, the coupling factor being the static armlength mismatch.

85

Note that the derivation of the phase fluctuations φ_{int} does not lead to any meaningful frequency noise. If the fluctuations of the interferometric phase are dominated by pathlength fluctuations caused by e.g. the test masses, its derivation would result in an estimation of their velocity fluctuations. A second derivation would lead to the acceleration noise. An example of such a calculation can be seen in Figure 5.20.

In this sense, the frequency fluctuations of an oscillator contain the same information as its phase fluctuations. For example, from the requirements for $\widetilde{\delta\nu}(f)$ shown in Figure 6.1, the corresponding requirements for $\widetilde{\delta\varphi}(f)$ could be derived via integration.

6.4.3. Transfer function

Until now we have expressed the influence of frequency noise $\delta\nu$ in the interferometer output φ_{int} using the simplified formula of Equation (6.4), which only considers frequency fluctuations that are slow in comparison with τ. This approach is valid for implementations of the kind of LTP, where the light travel time of the armlength mismatch is negligible compared to the relevant Fourier frequencies, but not for LISA.

As can be seen in Figure 6.4, the ratio of change in the interferometer output divided by frequency noise input is given by the plant transfer function $H(\mathrm{i}\omega)$. In this section we will present the theoretical expression for this transfer function $H_{\text{theo}}(\mathrm{i}\omega)$ and compare it with measurements performed on our hardware model.

The transfer function of the plant without servo (see Figure 6.4), measured from the frequency fluctuations of the oscillator $2\pi\delta\nu$ (expressed in rad/s) to the phasemeter output φ_{int} (expressed in rad), can be written as

$$H_{\text{theo}}(\mathrm{i}\omega) = \frac{1 - \exp(-\mathrm{i}\omega\tau)}{\mathrm{i}\omega} = \tau\,\frac{\sin(\omega\tau/2)}{(\omega\tau/2)}\,\exp(-\mathrm{i}\omega\tau/2). \tag{6.7}$$

The left part of Figure 6.6 shows the Bode representations of $H_{\text{theo}}(\mathrm{i}\omega)$, with the frequency on the x-axes (on a logarithmic scale) and the magnitude (or gain) on the left y-axis in dB units and the phase in degrees in the right side y-axis. It is flat at low frequencies, in accordance with the linear coupling between laser frequency noise and interferometric phase readout indicated in Equation (6.4), and shows nulls at frequencies $1/\tau$ and harmonics, that at first sight may suggest that such a system cannot be stabilised with a bandwidth higher than $1/\tau$.

The right part of Figure 6.6 shows the Nyquist diagram of $H_{\text{theo}}(\mathrm{i}\omega)$, together with the data measured from the prototype. In the Nyquist representation, the transfer function is shown in a parametric plot in the complex plane with the frequency as the running parameter. The transfer function shows a spiral-like form, with one revolution every $625\,\text{kHz}$, which is $1/\tau\,\text{Hz}$ in our system. This representation will be studied more deeply in Section 6.4.4, where the importance of this graph will also become clear.

It is important to notice the discrepancy between the theoretical transfer function $H_{\text{theo}}(\mathrm{i}\omega)$, plotted as the black dashed line, and the measured data $H_{\text{meas}}(\mathrm{i}\omega)$, plotted as the con-
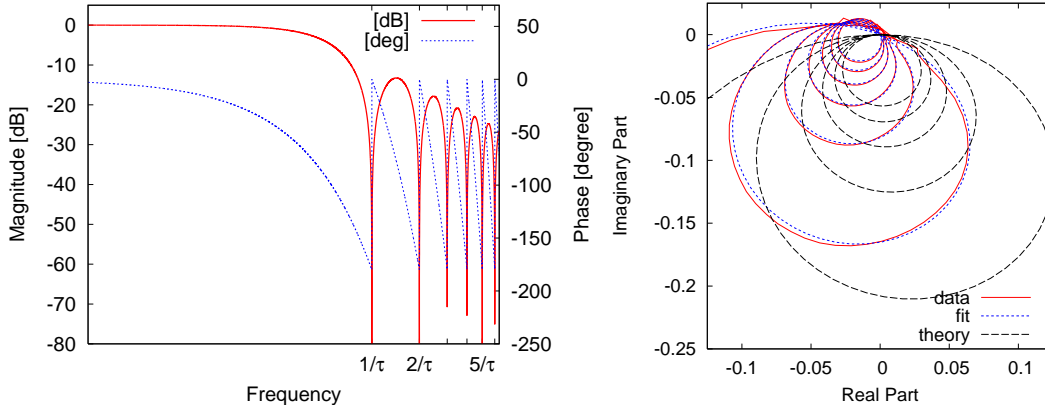
Figure 6.6: Transfer function of the plant. Left: Bode representation of the theoretical transfer function. The magnitude is given in units of τ. Right: Nyquist representation. The curve labelled "theory" represents the theoretical transfer function. The curve labelled "data" represents the one measured on the prototype and the curve labelled "fit" shows the model presented in Equation (6.8).

tinuous red line. To explain mathematically the difference between the two functions, a model has been fitted to the data that additionally includes an extra delay τ^* of 75 ns. This delay τ^* accounts for the finite reaction time of the VCO, the short interferometer arm and the phasemeter. The total effect is modelled by one single delay τ^* at the phasemeter output. This type of pure delay was already mentioned in Section 6.3 and is shown in Figure 6.5. Its importance as a limitation of the stabilisation bandwidth will be discussed in Section 6.4.4. The model also includes additional poles at ω_1, ω_3 and a zero at ω_2 for the non-ideal frequency response of the different components and is given by:

$$H_{\text{fit}}(i\omega) = \tau \frac{\sin(\omega\tau/2)}{(\omega\tau/2)}\exp(-i\omega\tau/2)\exp(-i\omega\tau^*)\left(\frac{1}{1+\frac{i\omega}{\omega_1}}\right)\left(1+\frac{i\omega}{\omega_2}\right)\left(\frac{1}{1+\frac{i\omega}{\omega_3}}\right) \quad (6.8)$$

$$= H_{\text{theo}}\exp(-i\omega\tau^*)\,p(i\omega, 530\,\text{kHz})\,z(i\omega, 830\,\text{kHz})\,p(i\omega, 12\,\text{MHz})$$

with

$$p(i\omega, f_{\text{p}}) = \left(\frac{1}{1+\frac{i\omega}{2\pi f_{\text{p}}}}\right)$$

and

$$z(i\omega, f_{\text{z}}) = \left(1+\frac{i\omega}{2\pi f_{\text{z}}}\right).$$

6.4.4. Performance and stability: Open loop gain

The open loop gain (OLG) is defined as the product of the transfer functions of the different subsystems that constitute the loop. As can be seen in Figure 6.7, the only elements of the control loop described in this chapter are the plant and the servo with transfer functions $H(\mathrm{i}\omega)$ and $G(\mathrm{i}\omega)$, respectively. The OLG can thus be written as

$$OLG(\mathrm{i}\omega) = H(\mathrm{i}\omega)\,G(\mathrm{i}\omega). \tag{6.9}$$

Figure 6.7 shows the experimental configuration used to measure the OLG once the loop was closed and stably locked. The frequency response between the signals $P + \delta\nu$ "Feedback+Noise" and P "Feedback" was evaluated with a network analyser while a sinusoidal perturbation was introduced in the system via the adder.

This way, the OLG was measured as

$$OLG = \frac{P}{P + \delta\nu} \tag{6.10}$$

The same experimental setup was used to measure the transfer function shown in Figure 6.6, with the only difference that the frequency response was measured between different signals:

$$H_{\mathrm{meas}} = \frac{R}{P + \delta\nu} \tag{6.11}$$

A more detailed description of this procedure can be found in [45].
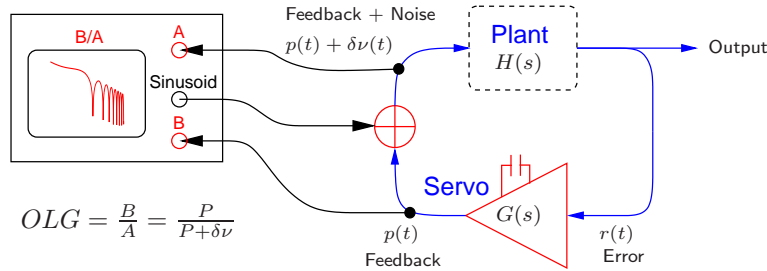
Figure 6.7: Experimental setup for measuring the open loop gain (OLG) of the control loop.

Figure 6.8 shows the measured OLG in the Bode representation. The gain increases towards low frequencies, achieving values near 40 dB at the beginning of the relevant frequency range. The highest frequency where the magnitude of the gain crosses unity —the so-called unity gain frequency (UGF)— is about 3.5 MHz, distinctly above the frequency inverse of the delay 625 kHz.
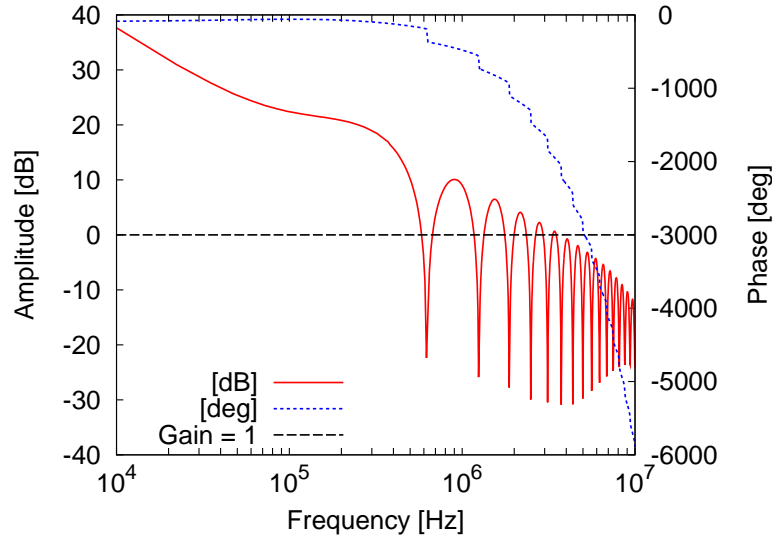
Figure 6.8: Bode representation of the measured OLG.

We will use the measured OLG from Figure 6.8 to study two of the most important properties of the control loop: its *performance* in terms of noise reduction and its *stability*. The noise reduction achieved by the loop at a given Fourier frequency $|C(i\omega)|$ can be defined as the ratio between the LSD of the phase of the oscillator when the stabilisation is working (oscillator "locked") and when not (oscillator "free-running"). Because of the relationship between the phase and frequency noise of the oscillator explained in Section 6.4.2, the frequency noise can be also used to calculate this ratio:

$$|C(i\omega)| = \frac{\widetilde{\varphi}_{\text{locked}(\omega)}}{\widetilde{\varphi}_{\text{freerunning}(\omega)}} = \frac{\widetilde{\nu}_{\text{locked}(\omega)}}{\widetilde{\nu}_{\text{freerunning}(\omega)}} \tag{6.12}$$

On the other hand, the noise reduction can also be expressed in terms of the OLG as:

$$|C(i\omega)| = \frac{1}{|1 + OLG(i\omega)|} = \frac{1}{|1 + G(i\omega)H(i\omega)|}. \tag{6.13}$$

In this section we analyse the loop noise suppression and stability based on the expression 6.13, which uses the OLG measurement presented before. In Section 6.5 we will validate the conclusions obtained here evaluating expression 6.12 with independent measurements of the oscillator phase.

Equation (6.13) indicates that the noise suppression at a given Fourier frequency increases with the gain of the OLG. Consequently, the aim of the controller design is to maximise the gain over the frequency range of interest. Unfortunately, the gain cannot be increased

indefinitely without compromising the stability of the control loop. In particular, when the denominator in Equation (6.13) becomes smaller than one, noise gets amplified instead of reduced and endangers the loop stability. This noise amplification becomes maximal for OLG values near -1 (magnitude 1 and phase -180ï¿½), which leads to the following stability criteria:

- the highest UGF has to take place at frequencies where the phase of the OLG is above the $-180°$ limit.

Actually, a general rule of good practice in servo design is to have the UGF at a frequency where the phase is about $45°$ above the limit. The OLG shown in Figure 6.8 seems to contradict the previous stability criteria, especially in the frequency range above $1/\tau$, where gains higher than unity and phases below $-180°$ occur. But this apparent contradiction can be understood by studying the Nyquist representation of the OLG shown in Figure 6.9. Each point of the graph represents a frequency value, the x-coordinate given by the real part of the OLG at this frequency and the y-coordinate by its complex part.
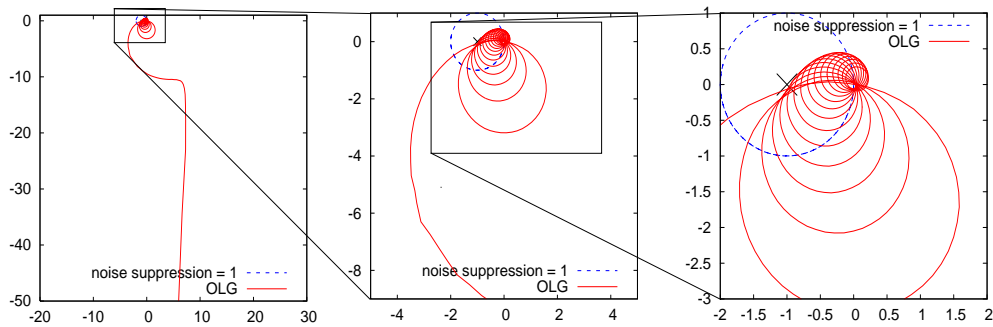
Figure 6.9: Nyquist representation of the measured Open Loop Gain, useful for a direct interpretation of the stability criteria: the system becomes unstable if the OLG (continuous red line) encircles the the point (-1,0), marked with a cross.

The Nyquist representation of the OLG in Figure 6.9 allows to make a simple geometrical interpretation of the noise suppression and stability of the loop described by Equation (6.13), which is reproduced here:

$$C(\mathrm{i}\omega) = \frac{1}{|1 + OLG(\mathrm{i}\omega)|}. \tag{7.13}$$

noise suppression: the circle with centre (-1,0) and radius 1 (blue dashed line in Figure 6.9) divides the complex plane in two regions. OLG values outside the circle correspond to noise suppression, as they make the term $|1 + OLG(\mathrm{i}\omega)|$, the denominator of Equation (6.13), bigger than one. On the contrary, if at any given frequency ω_x the value of $OLG(\mathrm{i}\omega_\mathrm{x})$ is inside this circle, noise enhancement occurs because the denominator of Equation (6.13) is smaller than one.

stability: The loop becomes unstable if the OLG has gain higher than one and phase below $-180°$. In the Nyquist representation, this occurs if the OLG encircles the point (-1,0), that has been marked in Figure 6.9 with a cross.

Applying these considerations to the OLG in Figure 6.9 it is clear that such a system is stable, as the point (-1,0) is not encircled. A transition to the unstable regime occurs, for example, if the overall gain is increased, as this would make the curve "homogeneously grow" with respect to the origin and thus encircle the point (-1,0). This transition has been verified by the author with the measurement setup depicted in Figure 6.7, as it delivers a continuous monitoring of the OLG.

Apart from being used to predict stable configurations for systems with this kind of transfer function [53] and to optimise the servo design, the Nyquist representation shows very clearly that the limiting factor for the achievable gain and bandwidth is the "clock-wise rotation" of the spiral-like gain curve. This rotation is caused by the extra phase lag τ^* found in the measured transfer function of the plant $H(i\omega)$ from Figure 6.6 in Section 6.4.3.

We can conclude that this additional pure delay τ^* limits the stabilisation bandwidth and gain. Its origin has been found in processing delays in the short interferometer arm and further electronics. The modelling of this local delay τ^* and its minimisation should be consequently taken into account in the final implementation of arm-locking for LISA.

6.4.5. Servo

The servo frequency response $G(i\omega)$ is presented in Figure 6.10, with the magnitude on the left hand side of the figure and the phase on the right hand side. The measurement procedure for this transfer function is very similar to the one described for the OLG in Figure 6.7, with the only difference that the servo transfer function was obtained as the frequency response between the feedback signal $v(t)$ and the error signal $r(t)$. The spikes that can be seen at frequencies multiple of $1/\tau$ are not part of the servo transfer function itself but are caused by the low SNR of this measurement procedure at those frequencies.

Together with the measured transfer function, Figure 6.10 also shows the following model for $G(i\omega)$ that was fit to the data via LISO [4]:

$$
\begin{aligned}
G(i\omega) = \left(\frac{K}{i\omega}\right) &\times z(i\omega, 100\,\text{kHz}) \times \\
&z(i\omega, 106.6\,\text{kHz}) \times p(i\omega, 172.4\,\text{kHz}) \times \\
&z(i\omega, 843.7\,\text{kHz}) \times p(i\omega, 1.8\,\text{MHz}).
\end{aligned}
\tag{6.14}
$$

The low frequency range of the servo response shown in Figure 6.10 is described by the first line of Equation (6.14): a 1/f decay from DC to approximately 100 kHz with a gain factor K $= 9 \times 10^4$. To higher frequencies, the next terms show a series of alternating poles and zeros that result in a frequency response approaching $f^{0.3}$ between 200 kHz and 1 MHz.

The spacing ratio between poles and zeros can be varied to obtain frequency responses with different non-integer exponents, allowing the design of this type of frequency responses out of simpler "pole and zero" blocks [53]. The circuit topology of the servo pre-

sented in this section together with a deeper insight on this type of frequency response can be found in [42]. The detailed schematics of the servo are shown in Figure B.5.

The starting point for such a servo design was presented in [53], but the formalism presented there (and in other publications discussing arm-locking) considers the frequency actuator as part of the controller rather than part of the plant: they assume actuation on laser phase (using e.g. an EOM) and here we assume actuation on the laser frequency (e.g. on the laser PZT). This corresponds to taking a factor of $1/f$ from the transfer function presented here, which remains then flat to high frequencies, and allocating it to the servo frequency response, which would then become $f^{-0.7}$ instead of the $f^{0.3}$ presented here. In any case, the system OLG remains unaffected which makes both formalisms equivalent.
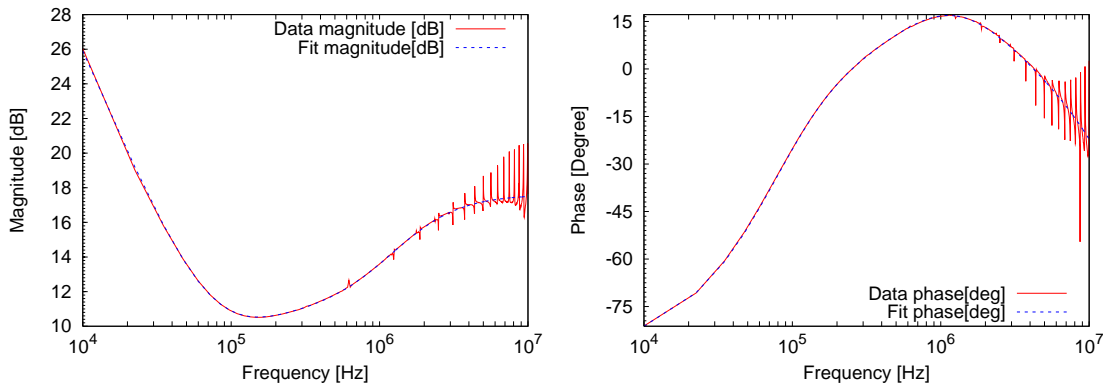
Figure 6.10: Frequency response of the servo used and a fit to the measured data.

6.5. Independent analysis of loop performance by external readout of the oscillator's phase

One of the advantages of the arm-locking experiment presented here is the relatively low frequency of the signal from the VCO (72 MHz) compared to that of a laser (282 THz). This makes it simpler to sample the oscillator signal directly and perform a phase readout with respect to the sampling clock, which is assumed noise free here. This phasemeter, as will be explained in Section 6.5.1, delivers a time-series of the oscillator phase $\varphi(t)$ without intervention of the control loop, so that we have available an "out-of-loop" measurement to investigate the performance of the stabilisation and validate the conclusions of section 6.4.4.

The phasemeter output will be analysed in the time domain (Section 6.5.3) to observe the locking procedure and the remaining temporal structure of the phase noise and in the frequency domain (Section 6.5.2) by comparing the spectral density (LSD) of the oscillator phase noise with and without stabilisation.

6.5.1. Phasemeter

The phase readout explained in this section is based on the same algorithm as the LTP phasemeter (see Chapter 2 and [20, 21, 64]), but the present implementation is applied to a signal of frequency $72\,\text{MHz}$ instead of $1.6\,\text{kHz}$.

The different processing stages of the phasemeter can be explained, referring to the scheme in Figure 6.11, as follows:

1. A sample of the oscillator signal

$$v_{\text{osc}}(t) = A\sin(2\pi\nu t + \varphi) \tag{6.15}$$

   is fed to the phasemeter. In the first stage it is sampled at a rate f_{sam} with an analog-to-digital converter.

2. In the next block a single-bin discrete Fourier transform (SBDFT) is performed on N digitised samples, labelled as v_{osc}^n with n running from $0 \ldots N-1$. A SBDFT can be understood as a Fourier transformation in which only one Fourier result —also called bin— corresponding to the oscillator frequency is calculated. This way we obtain the complex amplitude of the oscillator signal at the frequency ν as

$$\Re(V_{\text{osc}}(\nu)) = \frac{1}{N} \sum_{n=0}^{N-1} v_{\text{osc}}^n \cdot \cos\left(2\pi\nu\frac{n}{f_{\text{samp}}}\right), \tag{6.16}$$

   and

$$\Im(V_{\text{osc}}(\nu)) = \frac{1}{N} \sum_{n=0}^{N-1} v_{\text{osc}}^n \cdot \sin\left(2\pi\nu\frac{n}{f_{\text{samp}}}\right). \tag{6.17}$$

   In this stage, the time series v_{osc}^n, that was sampled at a frequency f_{sam} is reduced to the complex amplitude $V_{\text{osc}}(\nu)$ at a lower rate f_{ph}, given by

$$f_{\text{ph}} = \frac{f_{\text{sam}}}{N}. \tag{6.18}$$

3. Finally, the phase of the complex amplitude is calculated as

$$\varphi(t) = \arctan\left(\frac{\Im(V_{\text{osc}}(\nu))}{\Re(V_{\text{osc}}(\nu))}\right). \tag{6.19}$$

   The actual software implementation is more complicated: first, the used arctan routine determines the quadrant of the complex plane containing the amplitude, so that its output range goes from $-\pi$ to π and second, a phasetracking algorithm [21] removes jumps in the obtained phase time series by appropriately adding an integer number of 2π.

The phasemeter processing described before was implemented with two different data acquisition systems. An "Infiniium" oscilloscope with a sampling frequency $f_{\text{samp}} = 2\,\text{GHz}$ and 8 bits resolution was used with $N = 28$ to calculate the phase at a high rate of
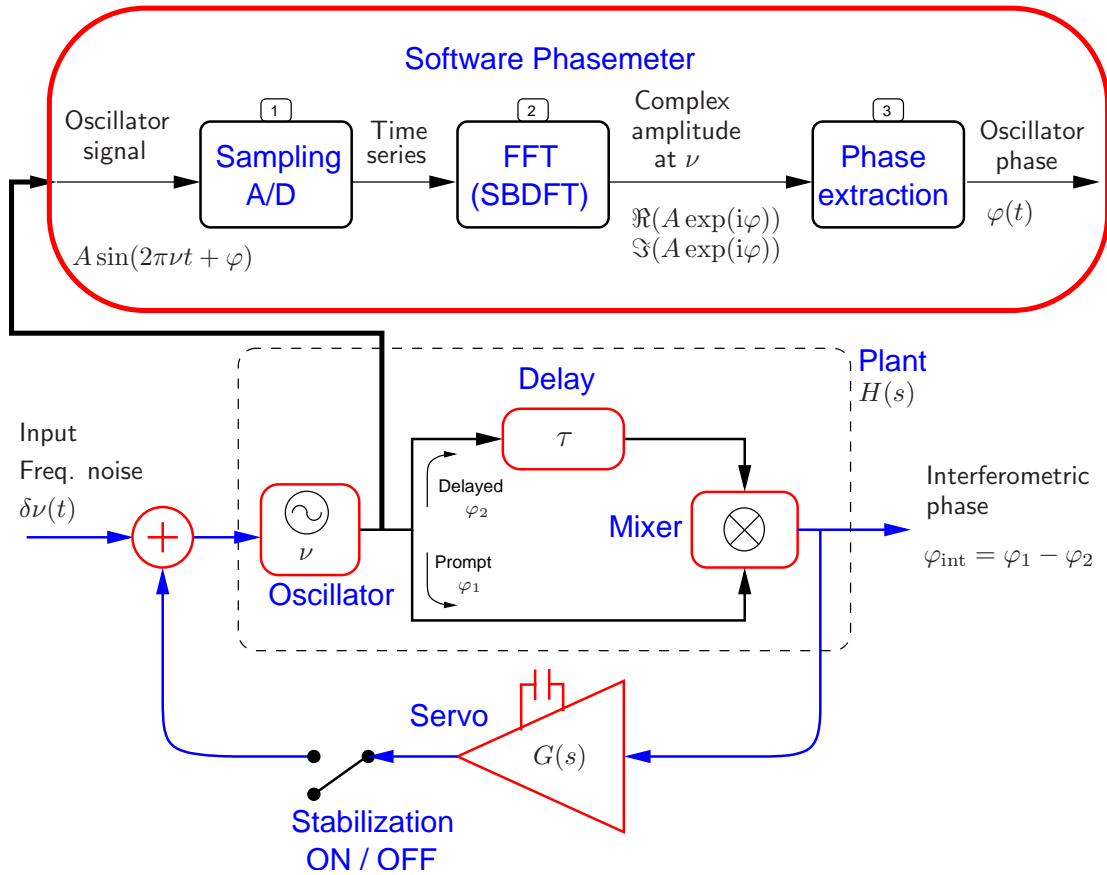
Figure 6.11: Experimental setup with detailed scheme of the phasemeter. Based on a Single bin discrete Fourier Transform (SBDFT), it delivers a time series of the oscillator's phase $\varphi(t)$ that allows the analysis of the stabilisation characteristics.

$f_{\mathrm{ph}} \approx 70\,\mathrm{MHz}$. This corresponds to one phase estimation per period of the VCO, the maximum practically possible output rate. This way the spectral content of the phase could be analysed up to high frequencies. The data shown in Figure 6.12 were measured with this configuration.

In order to sample with a higher resolution for the time domain investigations, a second sampling system "Ultrafast UF4021" with $f_{\mathrm{samp}} = 20\,\mathrm{MHz}$ and 14 bits was used. Due to the relatively low sampling frequency with respect to the $72\,\mathrm{MHz}$ of the VCO, it was necessary to down-mix the VCO frequency to $5\,\mathrm{MHz}$ with an external oscillator with negligible noise in comparison to the frequency noise artificially introduced for the investigations. This way, with $N = 4$, a phase rate of $f_{\mathrm{ph}} = 5\,\mathrm{MHz}$ was obtained. Typical examples for time series of the oscillator's phase obtained with this setup can be seen in Figures 6.13 and 6.14 from Section 6.5.3, where the time-domain analysis will be performed.

6.5.2. Frequency domain: noise suppression
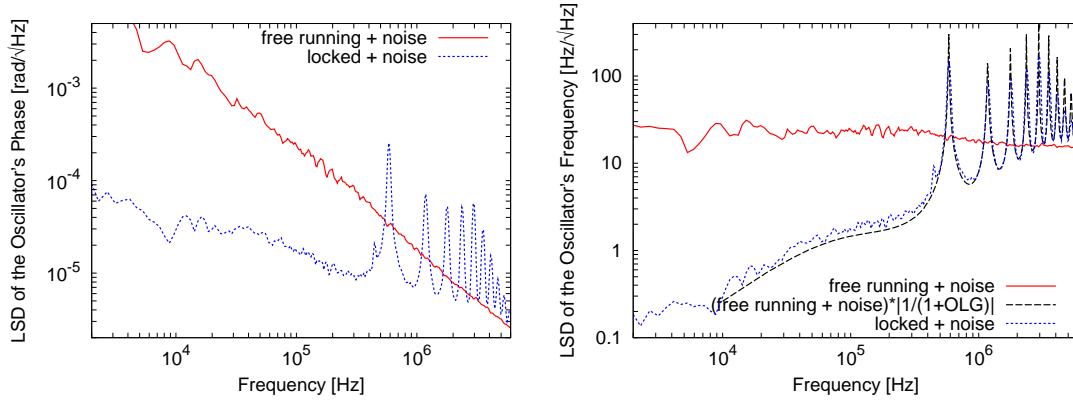
Figure 6.12: Linear spectral density (LSD) of the oscillator's phase (left) and frequency (right). The solid curves show the oscillator in "free-running" mode and the dotted ones refer to the stabilised state. The dashed curve on the right shows the frequency noise suppression predicted by the measured OLG (Section 6.4.4).

In order to study the spectral content of the oscillator phase, a time-series of the phasemeter output $\varphi(t)$ was stored and its linear spectral density (LSD) $\widetilde{\varphi(f)}$ calculated with `lpsd` [65]. Figure 6.11 shows the measurement setup, where the following two important features are to be noted: first, white frequency noise $\delta\nu(t)$ was intentionally added to the oscillator signal via its frequency modulation input. Second, a loop switch was used to select between the states oscillator "locked" (stabilisation ON) or "free-running" (stabilisation OFF).

With this setup, two different runs were taken for each given noise spectral shape, one with the oscillator locked and one free-running. The left part of Figure 6.12 shows the results of two such measurements. The ratio between the LSD of the oscillator phase when it is free running (continuous blue curve) and when it is locked (dotted black curve) gives the noise suppression of the loop, as stated in Equation (6.12). From the LSD of the phase it is straight-forward to compute the LSD of the oscillator frequency, by just multiplying with the Fourier frequency:

$$\widetilde{\nu}(f) = f\widetilde{\varphi}(f). \tag{6.20}$$

The result is plotted in the right graph of Figure 6.12 and shows the expected flat spectrum for the free running frequency noise, corresponding to the white noise $\widetilde{\delta\nu}(f)$ added at the frequency modulation input of the VCO, whereas the free-running phase noise on the left has the typical $1/f$ spectrum resulting from the integration of the white frequency noise. Although frequency or phase noise are equivalent representations of the oscillator noise, the frequency is usually employed (as in Figure 6.1) to define the noise requirements, because it couples linearly into the interferometric phase readout.

Two important features can be distinguished in Figure 6.12:

- There are frequencies higher than $1/\tau$ at which the stabilised noise level is below the free running noise, confirming noise suppression at those frequencies.
- we can compare the noise suppression which has been measured here independently from the stabilisation signals with the noise suppression function $C(\mathrm{i}\omega)$ predicted from the measured OLG. To this end, the disturbance sensitivity function

$$\widetilde{\delta\nu}(\mathrm{i}\omega)C(\mathrm{i}\omega) = \frac{\widetilde{\delta\nu}(\mathrm{i}\omega)}{|1 + OLG(\mathrm{i}\omega)|} \tag{6.21}$$

is plotted superimposed to the frequency noise curve, where $\widetilde{\delta\nu}(\mathrm{i}\omega)$ is the LSD of the introduced frequency noise and $OLG(\mathrm{i}\omega)$ is the measured OLG presented in Section 6.4.4. The good agreement between the two curves confirms the predicted noise suppression.

The measurements presented here independently confirm the noise suppression predicted in Section 6.4.4 that was based on closed loop measurements of the OLG. Also the predicted noise enhancement in the vicinity of $1/\tau$ and harmonics has been confirmed. This noise enhancement is however not worrisome, as it occurs at frequencies where the LISA sensitivity to gravitational waves is also diminished because of the constellation antenna pattern. Besides more sophisticated arm-locking configurations [60, 66] —e.g. using the mean length of two arms— do not show this noise enhancement.

6.5.3. Time domain

The time evolution of the oscillator's phase during lock acquisition is analysed here. For all the figures of this subsection, the controller is turned on at $t = 0$ and the time axis is measured in units of τ.

For a proper analysis of the lock acquisition, two additional features were implemented in the switching block presented in Figure 6.11. First, its bouncing[3] was suppressed with a Schmitt-trigger based circuit, shown in Figure B.6. More importantly, after the switching itself, the controller gain can be modified with an external signal using a voltage controlled amplifier.

This way the loop can be locked *abruptly*, going from free-running to full controller gain instantaneously, or *gradually* by slowly increasing the controller gain. For the solid curves of the runs presented in Figures 6.13 and 6.14 the gain of the controller was turned on abruptly, whereas for the dashed ones the gain was ramped up linearly during approximately $16\,\mu\mathrm{s}\,(10\,\tau)$.

Figure 6.13 shows the time evolution of the oscillator phase during two such lock acquisitions while white frequency noise is being added to the oscillator signal as described in

---

[3]After mechanically changing the state of a switch, its electrical response goes back and forth during several milliseconds before it reliably settles in the commanded state. Until then, the switch is said to be bouncing.

Section 6.5. As predicted in [53] and [56], a pseudo-periodic transient can be observed just after the lock acquisition, whose initial amplitude is smaller when the gain is ramped up as opposed to the case of abrupt switching.
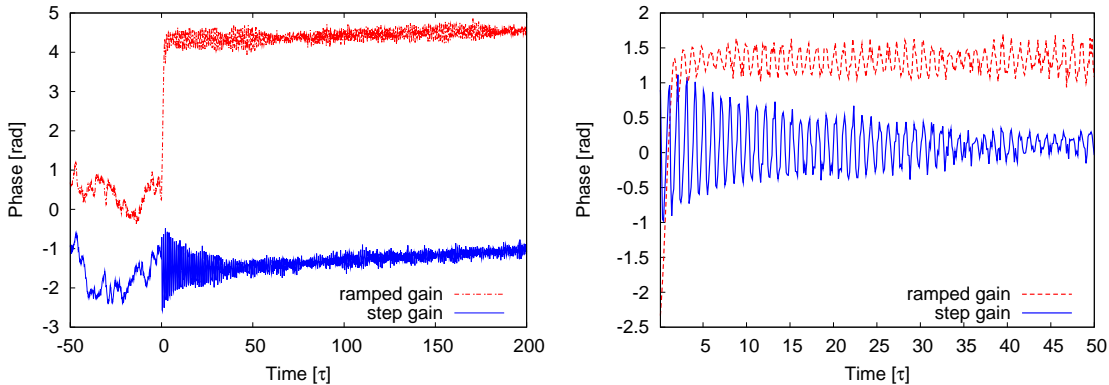
Figure 6.13: Lock acquisition as white frequency noise is being added into the system. The initial amplitude of the transient is smaller when the gain is ramped up than when turned on abruptly. Left: General overview before and after the lock. Right: detailed view just after the lock.

The remaining noise at a time $t = 200\tau$ after the lock acquisition is shown in the graph on the left in Figure 6.14. In this time scale, any initial transient has already decayed and only the stationary response of the stabilised system is present. It does not show pure periodic repetition of the same time segment but a structure typical for pseudo-harmonic narrow-band noise. This corresponds to the spectral content of the stabilised noise shown in Figure 6.12, where narrow band peaks occur at frequencies that are multiples of $1/\tau$.

A different feature of the controller design is its remarkable robustness, which can be seen in the right part of Figure 6.14: $1/f$ noise is injected instead of white noise and the system locks at once despite the strong perturbations that drive the phase of the oscillator over several hundreds of radians before the stabilisation is turned on. In this graph, the difference between the two switching procedures is difficult to appreciate due to the large scale of the noise previous to the lock acquisition.

6.6. Discussion and outlook

Arm-locking (see [53]) detects frequency fluctuations of a LISA laser by measuring the phase difference between the prompt laser signal and a delayed ($\tau = 33\,s$) version of itself that has been reflected on a remote LISA satellite. In the hardware model presented here, the phase subtraction takes place between the signal from a VCO and a second version of itself that is delayed by $\tau = 1.6\,\mu s$. Frequency fluctuations of the VCO show up in our phase difference in the same way as frequency fluctuations of the laser do in the LISA configuration, which allowed us to implement a frequency stabilisation for the VCO based on the one described in [53]. Although it takes place in a different frequency range due
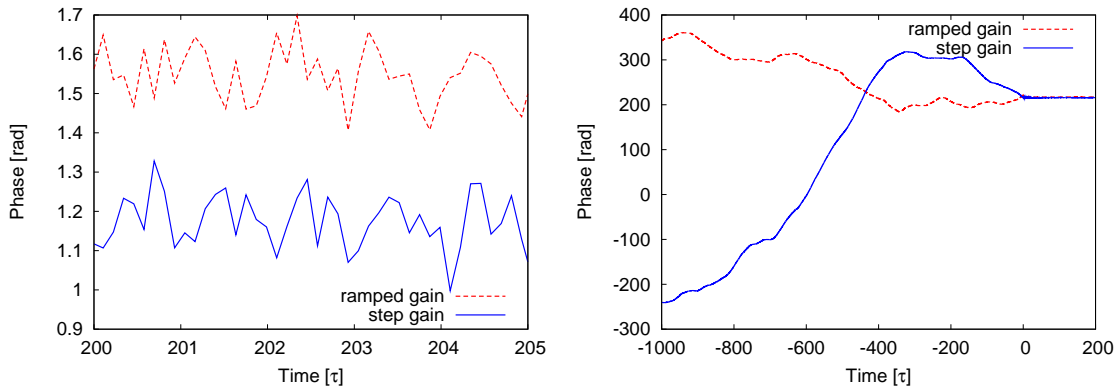
Figure 6.14: Left: Detailed view of the time series shown in Figure 6.13. It begins $200\,\tau$ after locking. Right: Lock acquisition in the presence of $1/f$ noise

to the comparatively small delay of $1.6\,\mu$s, it permits the experimental confirmation of the main features of arm-locking.

First of all, the highest UGF of this kind of stabilisation is not limited to values far below $1/\tau$, as was traditionally assumed (see [52]). This can be seen from the measured OLG (Figure 6.8 and 6.9) and from the noise plots (Figure 6.12), in which frequency noise reduction takes place at frequencies above $625\,$kHz $(1/\tau)$ and the highest UGF appears at about $3.5\,$MHz.

Actually, the performance of our loop is only limited by the spurious delay $\tau^* = 75\,$ns present at the output of the phasemeter. This delay τ^* limits the bandwidth and gain of the servo as discussed in section 6.4.4. Such delays appear frequently in the experimental realisation of a phasemeter and therefore care must be taken to minimise them in the implementation of this technique on-board LISA.

The frequency noise of the oscillator gets reduced when the stabilisation is turned on, as can be seen in Figure 6.12 for the frequency domain and Figure 6.13 and 6.14 for the time domain. This noise reduction is also in agreement with the predicted performance that was derived from the measured OLG (Figure 6.12). Our hardware model of arm-locking demonstrates that the $33\,$s delay present in LISA does not represent a fundamental limitation in the performance of the stabilisation. Arm-locking is now in the LISA baseline and meanwhile experimental setups have been realised in which the laser phase has been physically delayed with a several km long optical fibre [57, 67, 58] or by digital means [59, 68, 69].

Although the aim of the investigations presented in this chapter was to prove the principle of function of the most basic arm-locking implementation, more sophisticated ones are under study, going from the simple use of the mean value of two arms as sensor to so-called "feed-forward" or "dual arm-locking" [60, 66].

Chapter 7.

Optical window noise investigations

In LISA Pathfinder and LISA the position fluctuations of drag free test masses will be determined interferometrically to picometre precision. To this end, laser light is brought to interference with a reference beam on an ultra-stable optical bench after being reflected at the test mass, which needs to be in an ultra-high vacuum. The present baseline for both missions includes a separate vacuum enclosure for each test mass, so that the sensing laser beam has to pass through an optical window. This window is therefore a transmissive element in the interferometer and its associated pathlength fluctuations, which are potentially significant, are the subject of the investigations presented in this chapter.

We have selected an athermal glass that should minimise the thermally induced pathlength changes. To investigate the instabilities caused by the mechanical environment when the glass is part of the vacuum tank, samples of this athermal glass have been mounted in optical window assembly prototypes (from now on optical window prototypes or just optical windows).

The pathlength sensitivity to both temperature fluctuations and temperature gradients has been measured with a dedicated interferometer. We have also analysed the long-term stability of the LISA Technology Package (LTP) interferometer when an optical window is present in the beam path. Finally, glass samples have been irradiated with high energy protons and the resulting optical absorption in the glass has been measured. Some specific results of the investigations presented here can be found in [70, 71, 72].

7.1. Introduction

The effects of an optical window in the interferometric path are equivalent for LISA Pathfinder and LISA, but the requirements on pathlength stability are more stringent for LISA. The considerations in this chapter will be held as general as possible in order to serve for any interferometric design that includes optical windows. To make concrete numerical estimations, the Pathfinder design parameters will be used, which in most cases are valid for LISA as well. For the experimental determination of pathlength fluctuations, the LISA Technology Package (LTP) interferometric readout described in Chapter 2 will

be used for two reasons: it offers the possibility of measuring long-term pathlength stabilities of the order of pm/$\sqrt{\text{Hz}}$ in the mHz frequency range and it is representative for the LTP design.

7.2. Optical glass geometrical properties

The basic geometrical properties of the optical windows can be derived from the LTP set-up: Figure 7.1 shows the LTP core assembly, with each test mass inside its vacuum tank and the optical bench between them, holding the optical components that form the four LTP interferometers. The laser beam travels back and forth through the optical windows into these vacuum tanks to be reflected at the test masses, as can be seen in the schematic layout of one LTP interferometer in Figure 7.2.
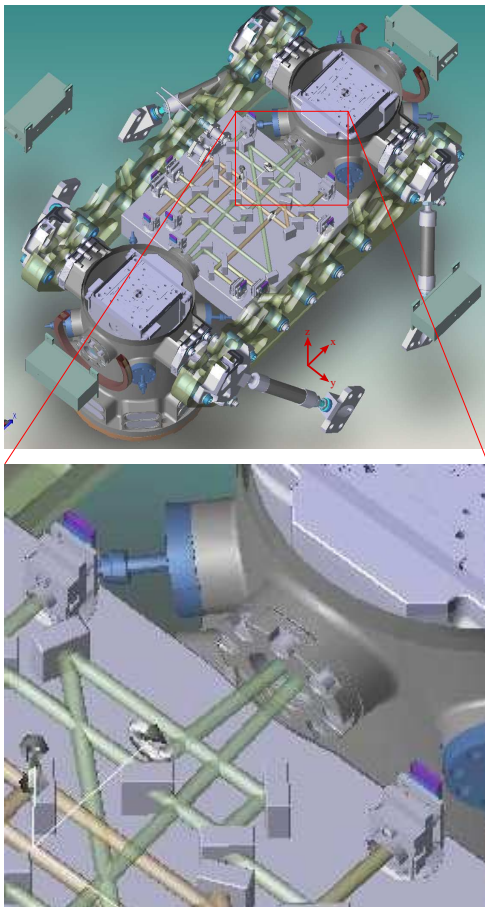
Figure 7.1: CAD drawing showing a sectional view of the LTP core assembly and a detailed view of one optical window situation. Drawings provided by EADS Astrium.
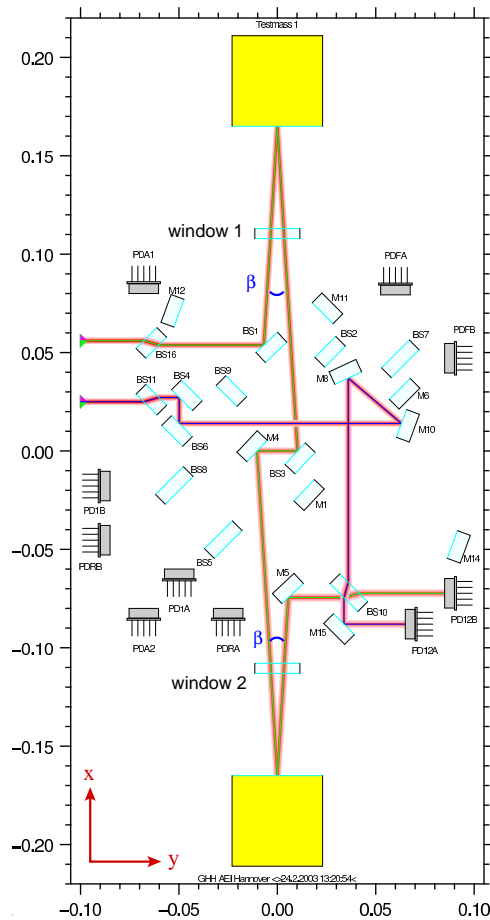
Figure 7.2: Optocad model of one LTP interferometer on the optical bench, where the measurement beam goes through two optical windows.

The necessary aperture for the windows d can be estimated as

$$d = 2\,x \tan\left(\frac{\beta}{2}\right) + k \cdot 2w, \tag{7.1}$$

where β is twice the incidence angle in the interferometric plane as shown in Figure 7.2, w the beam radius and x the distance between optical window and test mass. Each curve in Figure 7.3 shows the aperture d necessary to avoid beam clipping with a safety factor k of 4 and 5 respectively. For a typical distance of $x \approx 60\,\mathrm{mm}$ a window diameter of $d \approx 20\,\mathrm{mm}$ would be more than sufficient, but a glass diameter of $d = 30\,\mathrm{mm}$ has been selected for LTP to account for the space necessary to mount the glass onto the vacuum tank.
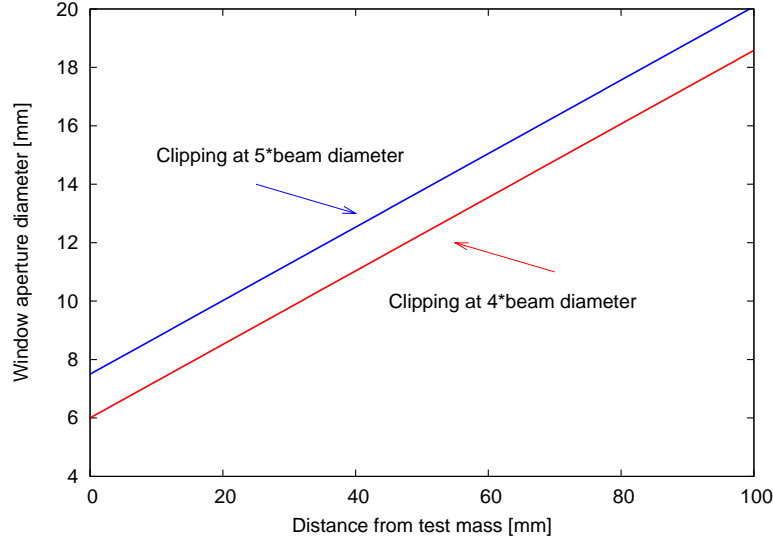
Figure 7.3: Optical window diameter required to avoid beam clipping in dependence of the distance between optical window and test mass, given a half incidence angle $\beta = 3.6°$ and beam diameter 2w = 1.5 mm, as in the LTP layout (Figure 7.2).

The thickness of the window will be $L = 6\,\mathrm{mm}$, comparable to other optical components. To minimise ghost reflections in the optical plane and stray-light in general, a tilt in the vertical direction of $\theta = 2.5°$ is foreseen between the optical window and the incident beam (see Figure 7.4), as well as an anti-reflection coating on both sides of the glass. The possibility of adding a conductive ITO coating on the inner side (facing the test mass) is under investigation. These parameters will be used in the calculations of Section 7.3, as well as other general assumptions, such as the laser wavelength $\lambda = 1064\,\mathrm{nm}$ and double pass of the laser beam through the glass.

7.3. Mechanisms that influence the window optical pathlength

The optical window is considered as a transmissive element in an interferometer as shown in Figure 7.4, where the laser beam impinges on a parallel plate of length L and refractive

index n with an incident angle θ. The pathlength difference at the interferometer output s is given by:

$$s = s_0 - a + nl. \tag{7.2}$$

In this expression s_0 is the optical pathlength difference of the interferometer as if it would not contain any window. When the window is introduced, s_0 decreases by a and increases by the optical pathlength of the window $n \cdot l$. Note that s_0 does not depend on the window properties and has only been introduced as reference length. In both LISA Pathfinder and LISA the detected variable will be the optical phase, which is related to the optical pathlength by

$$\varphi = \frac{2\pi}{\lambda} s. \tag{7.3}$$

Both variables are equivalent and the optical pathlength is typically used to derive requirements for the interferometry, whereas the phase formalism is more convenient to analyse experimental data, as shown in Section 7.4 and 7.5.
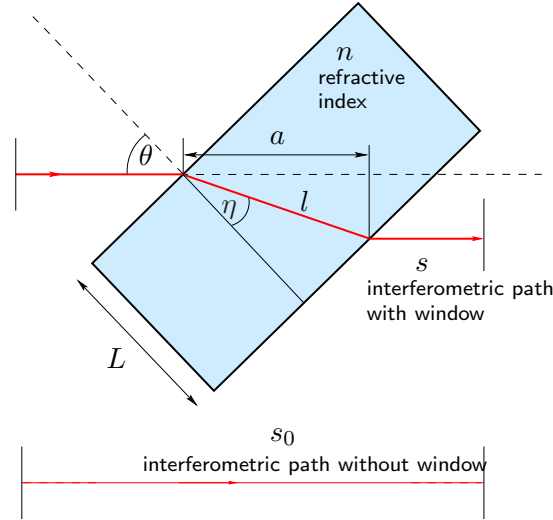
Figure 7.4: Optical window as transmissive element inside an interferometer. The optical window modifies the original interferometric path s_0 by $n \cdot l - a$.

The influence of the parameters *temperature, stress, mechanical motion* and *mechanical tilt* on s will be considered separately in this section. Assuming linearity in the coupling of the parameters into the pathlength and no dependence of the coupling coefficient with Fourier frequency, we can write for each parameter p_i individually:

$$\widetilde{\delta s_i} = \frac{\mathrm{d}s}{\mathrm{d}p_i} \widetilde{\delta p_i}. \tag{7.4}$$

Reformulating for $\widetilde{\delta p_i}$:

$$\widetilde{\delta p_i} = \left(\frac{\mathrm{d}s}{\mathrm{d}p_i} \right)^{-1} \widetilde{\delta s_i}. \tag{7.5}$$

This way, if the determination of the coupling coefficient $\frac{\mathrm{d}s}{\mathrm{d}p_\mathrm{i}}$ is possible, it can be used to estimate the permissible fluctuations of the parameter $\widetilde{\delta p_\mathrm{i}}$ that will cause a given pathlength noise level δs_i relevant for LISA, for example $1\,\mathrm{pm}/\sqrt{\mathrm{Hz}}$. As these coupling coefficients make use of the physical properties of the optical window, they constitute the criteria for selection of materials, assembly procedures and identification of critical parameters.

7.3.1. Temperature

In order to describe the temperature-driven pathlength fluctuations, the tilt of the window with respect to the incoming beam θ will be neglected. This assumption, as can be seen in Figure 7.4, implies

$$\theta \approx 0 \Rightarrow a \approx l \approx L, \tag{7.6}$$

which yields the following simplified description of the optical pathlength:

$$s = s_0 + L\left(n - 1\right). \tag{7.7}$$

The coupling coefficient between pathlength and temperature is calculated as the following derivative:

$$\frac{\mathrm{d}s}{\mathrm{d}T} = \frac{\mathrm{d}s_0}{\mathrm{d}T} + (n-1)\frac{\mathrm{d}L}{\mathrm{d}T} + L\frac{\mathrm{d}n}{\mathrm{d}T}. \tag{7.8}$$

Introducing the linear expansion coefficient $\alpha = \frac{\mathrm{d}L}{L\mathrm{d}T}$, a characteristic property of each material, and taking into account that original interferometric pathlength s_0 is not affected by the window temperature ($\frac{\mathrm{d}s_0}{\mathrm{d}T} = 0$) we obtain

$$\frac{\mathrm{d}s}{\mathrm{d}T} = L\left(\frac{\mathrm{d}n}{\mathrm{d}T} + (n-1)\alpha\right). \tag{7.9}$$

The important figure of merit

$$\mathrm{d}n/\mathrm{d}T + (n-1)\alpha. \tag{7.10}$$

was used as criteria in a market survey for the selection of an athermal glass, which identified the *OHARA S-PHM52* as the best candidate. Its characteristics are shown in Appendix A.1 together with the evaluation method for its figure of merit, which yields:

$$\frac{1}{L}\frac{\mathrm{d}s}{\mathrm{d}T} = \left(\frac{\mathrm{d}n}{\mathrm{d}T} + (n-1)\alpha\right) = 0.59\,\mathrm{ppm/K}. \tag{7.11}$$

Of all glass types offered by OHARA and Schott, this figure of merit ($0.6\,\mathrm{ppm/K}$ for S-PHM52) is the smallest one for the effect considered here. For a comparison, many

standard optical glasses have a figure of merit one order of magnitude higher, for example 5.31 ppm/K for BK7 or 8.32 ppm/K for fused silica.

We can estimate the temperature stability in the glass corresponding to pathlength fluctuations of $1\,\mathrm{pm}/\sqrt{\mathrm{Hz}}$ in double pass:

$$\widetilde{\delta T} = \frac{\widetilde{\delta s}}{2L\left(\frac{\mathrm{d}n}{\mathrm{d}T} + (n-1)\alpha\right)} = 1.4 \cdot 10^{-4}\,\mathrm{K}/\sqrt{\mathrm{Hz}} \tag{7.12}$$

It is also important to express the coupling between temperature and pathlength in terms of phase in single pass, to compare with the experimental results in Section 7.4.7

$$\frac{\mathrm{d}\varphi}{\mathrm{d}T} = \frac{2\pi}{\lambda}\frac{\mathrm{d}s}{\mathrm{d}T} = \frac{2\pi}{\lambda}L\left(\frac{\mathrm{d}n}{\mathrm{d}T} + (n-1)\alpha\right) = 21\,\mathrm{mrad/K}. \tag{7.13}$$

7.3.2. Mechanical shift perpendicular to the optical axis

Mechanical motion of the optical window in a given direction z perpendicular to the optical axis x can change the optical pathlength s in the presence of non-parallelism, as can be seen in Figure 7.5.
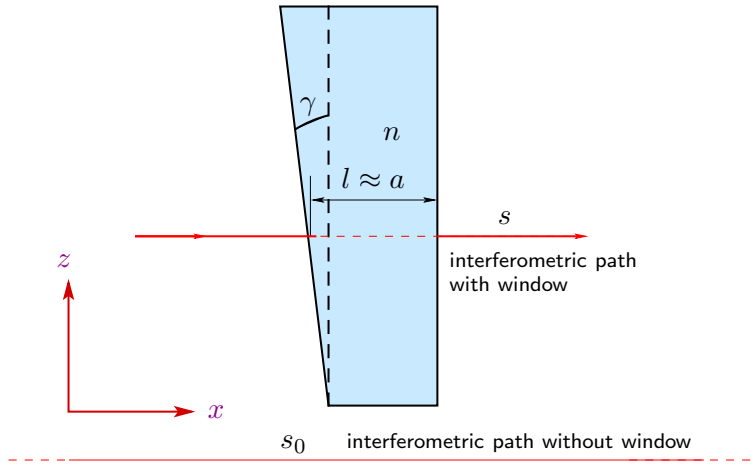
Figure 7.5: Optical window as transmissive element inside an interferometer under normal incidence and in presence of non-parallelism.

The incident angle θ will be neglected again and in turn we will introduce γ as the angle between the two optical surfaces of the window. The non-parallelism γ will be also considered small, so that we can write

$$\begin{aligned} \theta &\approx 0 \Rightarrow a \approx l \approx L \\ \gamma &\approx 0 \Rightarrow l \approx \gamma z \end{aligned} \tag{7.14}$$

and the optical pathlength s becomes:

$$s = s_0 + l(n-1) = s_0 + \gamma z(n-1). \tag{7.15}$$

The derivative of s with respect to z

$$\frac{\mathrm{d}s}{\mathrm{d}z} = \gamma(n-1) \tag{7.16}$$

allows the estimation of the maximum allowable mechanical fluctuations.

Taking the usual noise budget of $1\,\mathrm{pm}/\sqrt{\mathrm{Hz}}$ and an assumed typical non-parallelism of $\gamma \approx 30''$ we obtain

$$\widetilde{\delta z} = \frac{\widetilde{\delta s}}{\gamma 2(n-1)} = 5.7\,\mathrm{nm}/\sqrt{\mathrm{Hz}} \tag{7.17}$$

for double pass through an optical window made out of OHARA glass.

7.3.3. Mechanical tilt

The general situation depicted in Section 7.3 and Figure 7.4 will be considered here. Applying Snell's law together with geometrical considerations on Figure 7.4 we can write:

$$\begin{aligned} n &= \frac{\sin \theta}{\sin \eta}, \\ l &= \frac{d}{\cos \eta}, \\ a &= l \cos(\theta - \eta). \end{aligned} \tag{7.18}$$

By substituting the previous equations into the general form of s given by Equation (7.2) we can find an expression for s in dependence only of the desired parameters L, n, and the tilt angle θ:

$$s = s_0 - a + nl = s_0 + L\left(\sqrt{\frac{\cos 2\theta + 2n^2 - 1}{2}} - \cos \theta\right). \tag{7.19}$$

Its derivative is given by

$$\frac{\mathrm{d}s}{\mathrm{d}\theta} = L\left(\sin \theta - \frac{\sin 2\theta}{\sqrt{2(\cos 2\theta + 2n^2 - 1)}}\right) \tag{7.20}$$

and allows an estimation of the maximal tilt fluctuations of the optical window, width $L = 6\,\mathrm{mm}$, under static tilt angle $\theta = 2.5°$ in order to induce $1\,\mathrm{pm}/\sqrt{\mathrm{Hz}}$ pathlength fluctuations in double pass:

$$\widetilde{\delta z} = \frac{\widetilde{\delta s}}{L\left(\sin \theta - \frac{\sin 2\theta}{\sqrt{2(\cos 2\theta + 2n^2 - 1)}}\right)} = 5.1\,\mathrm{nrad}/\sqrt{\mathrm{Hz}} \tag{7.21}$$

7.3.4. Stress

In a similar way as when the effects of temperature fluctuations were considered in Section 7.3.1, the tilt angle of the optical window θ will be neglected here, thus yielding an optical pathlength s in the simple form of Equation (7.7). In order to assess the stress experienced by the optical glass, it is important to consider its mechanical environment. Figure 7.6 shows a schematic cross section of the glass assembled to the vacuum tank with a metallic cover tightened by bolts. A ring-shaped sealing structure on each side constitutes the interface between the glass and the metallic parts, so that any external tensile or compressive stress σ will be ultimately applied by these sealing rings.
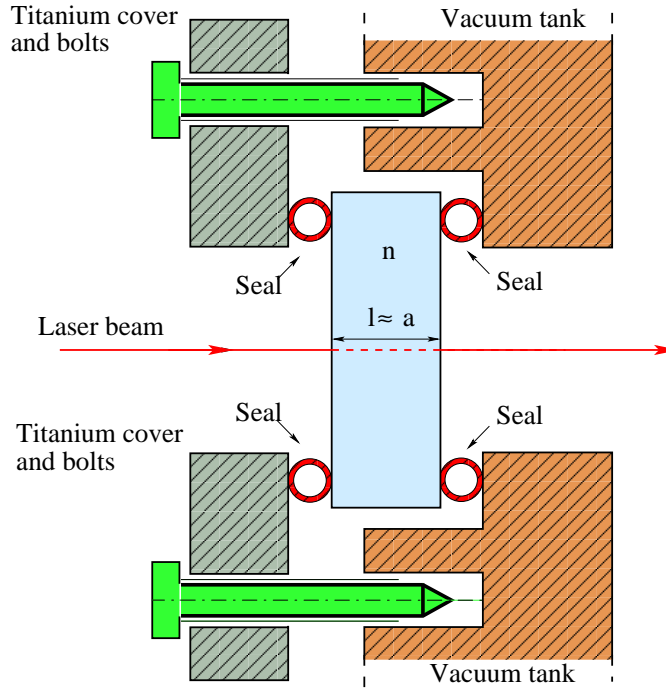
Figure 7.6: Sectional view of the mechanical assembly of the optical window on a vacuum tank (see Figure 7.9 for a 3D explosion view). Stress induced by the bolts to ensure leak-proof vacuum is ultimately applied to the optical window by the sealing rings.

The derivative of the pathlength s with respect to the stress σ is given by

$$\frac{\mathrm{d}s}{\mathrm{d}\sigma} = L\left(\frac{(n-1)}{Y} + \frac{\mathrm{d}n}{\mathrm{d}\sigma}\right), \tag{7.22}$$

where the Young modulus of the glass $Y = \frac{L\mathrm{d}\sigma}{\mathrm{d}L}$ has been introduced.

Equation (7.22) describes the influence of stress in the optical pathlength s as the sum of two contributions, one affecting the length of the glass and one affecting its refracting index, in a similar fashion as Equation (7.9) describes the influence of temperature (Section 7.3.1). There, it was possible to select the key parameters to minimise the relevant figure of merit and select an "athermal" glass.

Unfortunately, that approach is not feasible here: first, the knowledge of the relevant optical coefficient $\frac{\mathrm{d}n}{\mathrm{d}\sigma}$ is very limited, as will be explained below. Second, the mechanical environment of the assembled optical glass plays a key role in the effective stress fluctuations, and not only the intrinsic properties of the glass. This allows only to consider each term in Equation (7.22) separately in order to qualitatively estimate the influence of stress on the optical pathlength s under the assumption of the glass samples consisting of $L = 6\,\mathrm{mm}$ of athermal glass OHARA S-PHM52.

The first term of Equation (7.22), which describes length changes induced by changes in the Young modulus, assumes a perfectly homogeneous linear stress and no interaction between the sample under study and its surrounding materials. The validity of this model has therefore to be compared with experimental data. Keeping in mind such a strong simplification, we can still make a qualitative estimation of the stress fluctuations that would cause pathlength noise of $1\,\mathrm{pm}/\sqrt{\mathrm{Hz}}$ in double pass, given a Young's Modulus $Y = 71.5\,\mathrm{GPa}$:

$$\widetilde{\delta\sigma} = \frac{\widetilde{\delta s}\,Y}{2L} \approx 6\,\mathrm{Pa}/\sqrt{\mathrm{Hz}}. \tag{7.23}$$

This effect is expected to be approximately independent of the glass selection, as no strong variations are expected between the values of Young modulus of two different glasses.

The term $\frac{\mathrm{d}n}{\mathrm{d}\sigma}$ refers to the absolute change in the refractive index n caused by stress on the glass and has to be distinguished from the photoelastic constant β, which takes only the appearance of birefringence in the glass under stress into account, that is

$$\beta = \frac{n_\parallel(\sigma) - n_\perp(\sigma)}{\sigma} \neq \frac{\mathrm{d}n}{\mathrm{d}\sigma} = \frac{n(\sigma) - n(0)}{\sigma}. \tag{7.24}$$

Birrefringency is usually the only effect treated in the literature (e.g. [73]) when referring to stress in optical glass and not the absolute change in the pathlength $\frac{\mathrm{d}n}{\mathrm{d}\sigma}$, so that β is typically the only available parameter (also listed in Appendix A.1). Although it is stated in the literature (e.g. [74]) that no relationship can be established a priori between β and $\frac{\mathrm{d}n}{\mathrm{d}\sigma}$, both coefficients range in the same order of magnitude, so that the photoelastic constant of the OHARA glass $\beta = 1.0 \frac{\mathrm{nm}}{\mathrm{cm}\cdot 10^5\,\mathrm{Pa}}$ can be used to make an order-of-magnitude estimation of the permissible stress fluctuations that would induce $1\,\mathrm{pm}/\sqrt{\mathrm{Hz}}$ pathlength noise:

$$\widetilde{\delta\sigma} = \frac{\widetilde{\delta s}}{2\beta\,L} \approx 80\,\mathrm{Pa}/\sqrt{\mathrm{Hz}}. \tag{7.25}$$

The stress variations considered in this section are mainly due to differential expansion between the glass and its surroundings when exposed to temperature changes. They are mostly related to the difference between the linear thermal expansion coefficients of

glass and Titanium α_{Gl} and α_{Ti}. In order to minimise this effect, the glass was selected to have a thermal expansion coefficient $\alpha_{Gl} = 10.1\,\text{ppm/K}$ similar to the one of the titanium alloy usually employed in space science. This alloy (Ti-6Al-4V) contains 6 % in mass of aluminium and 4 % Vanadium [75] and has a thermal expansion coefficient $\alpha_{Ti} = 8.6\,\text{ppm/K}$.

The influence of the mismatch between the two expansion coefficients is difficult to estimate: as shown in Figure 7.6, the stress affecting the glass is actually applied by the sealing ring, typically made out of aluminium or silver. There is also a pre-load to guarantee the sealing applied by the titanium bolts on the cap and subsequently on the glass.

7.3.5. Conclusion

The estimations presented in Section 7.3 raise the concern that environmental fluctuations on the optical window may limit the interferometer sensitivity at a level above the LISA Pathfinder and LISA requirements.

Several effects that require a more experimental approach were identified:

- Dependence between the stress fluctuations and assembly procedure on the tank.
- Lack of information about the critical stress coupling coefficients such as $\frac{dn}{d\sigma}$.
- Coupling of thermal fluctuations into stress fluctuations due to differential material expansion.

It was therefore decided to manufacture breadboard prototypes of assembled optical windows to characterise their thermal and mechanical response as transmissive elements of an interferometer.

7.4. Interferometric characterisation

The investigations presented in this section aim to measure the response of the optical window to changes in temperature and its associated stress variations. In order to reproduce the mechanical environment of the glass, prototypes of the assembly of the glass on the vacuum tank were manufactured. They were placed as transmissive element in an optical bench to study the fluctuations of the optical path as function of external temperature changes.

The temperature measurements presented along this section and the analysis of the data were performed in collaboration with researchers from IEEC, Spain, the institution providing the diagnostics items for LTP. In particular, their low-noise front-end electronics (FEE) for temperature monitoring were used and experience was gained in the simultaneous analysis of phase and temperature readouts.

7.4.1. Glass samples

Samples of the athermal glass OHARA S-PHM52 were used to manufacture the optical window prototypes. The approximate composition of the athermal glass is listed in Table 7.1 and its technical properties are shown in Figure A.1. The properties of the glass samples acquired by AEI can be seen in Table 7.2.

Table 7.1: Approximate chemical composition of the athermal glass Ohara S-PHM52.

Chemical component	Weight in %
B_2O_3	2...10
CaO	2...10
BaO	30...40
ZnO	0...2
Sb_2O_3	0...2
WO_3	0...2
P_2O_5	40...50

Table 7.2: Properties of the glass samples used in the assembly of optical window prototypes.

Property	Value	Remark
material	S-PHM52	Fine annealed
diameter	$30 + 0 - 0.2\,\text{mm}$	
thickness	$6 \pm 0.1\,\text{mm}$	
parallelism	30"	
surface	$\lambda/2$ (at 633nm)	On the inner 20 mm diameter.
		Limited by degradation of the material
		in the presence of most usual polishing agents.
polish	60/40 scratch and dig	On the inner 20 mm diameter.

Some samples were coated with an anti-reflection coating on both sides, in order to study the influence of the stress induced by the coating on the glass and the possible darkening of the coating when exposed to high energy radiation. Both issues will be addressed later in this chapter.

7.4.2. Interferometric characterisation of the naked glass samples

Before the proper characterisation of the assembly prototypes, a preliminary investigation of the temperature influence in the optical pathlength of the naked glass was done. This characterisation was by no means as thorough as the one undertaken for the assembled

prototypes that will be presented in Section 7.4.6, but was useful to test the experimental set-up with respect to the theoretical prediction of Section 7.3.1.

Figure 7.8 shows a sample of athermal glass as transmissive element of an interferometer. The Kapton heaters attached to the glass were used to apply temperature steps to the glass while the evolution of the temperature was monitored with temperature sensors. At the same time, the output phase of the interferometer containing the window was measured. Figure 7.8 shows the result of a measurement run in which the glass temperature is relaxing after a heat pulse.
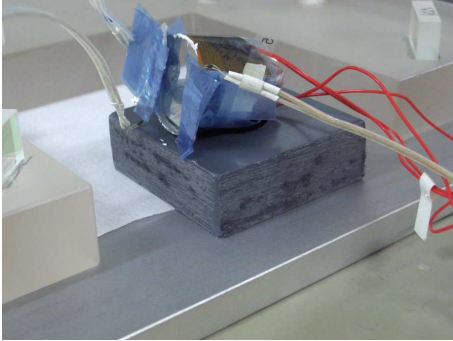
Figure 7.7: Optical window as interface between the optical bench and the vacuum enclosure containing the test mass.
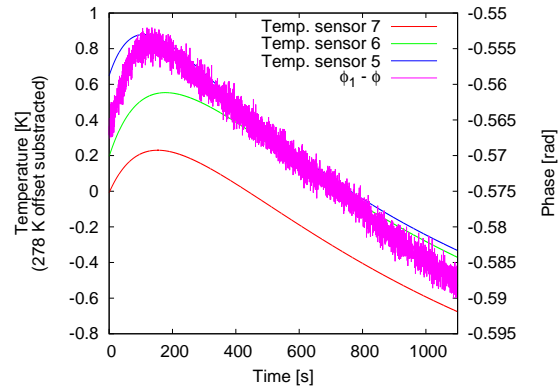
Figure 7.8: Pathlength evolution during a controlled temperature change in a naked glass sample.

Assuming a simple linear dependency between phase and temperature, a rough estimation of the coupling coefficient $\frac{\mathrm{d}\varphi}{\mathrm{d}T}$ can be made by inspection:

$$\frac{\mathrm{d}\varphi}{\mathrm{d}T} = \frac{0.045}{1.8} = 25\,\mathrm{mrad/K}. \tag{7.26}$$

Although this value represents only a rough estimate of the temperature influence on the optical pathlength of the naked glass, it is in good agreement with the $21\,\mathrm{mrad/K}$ calculated in Equation (7.13) in Section 7.3.1.

7.4.3. Assembly of prototypes

Three optical window prototypes were assembled by Carlo Gavazzi Space (CGS).

Each optical window prototype [76] is composed of the following items, listed as they appear in Figure 7.9 from right lo left:

- CF 40 Flange
- sealing ring
- sample of athermal glass Ohara S-PHM52
- sealing ring
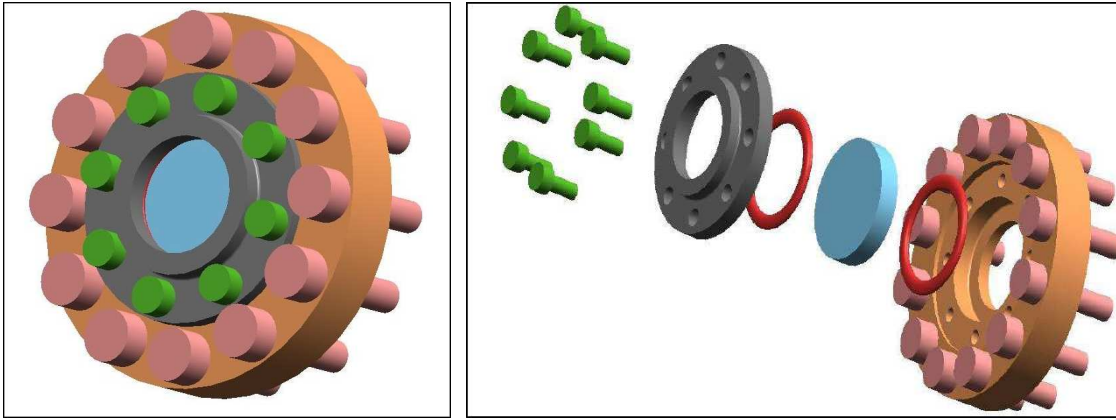
Figure 7.9: CAD drawing of an optical window prototype and its explosion view. Drawings provided by Carlo Gavacci Space

- titanium cover
- titanium bolts

The sealing is realized by 2 *helicoflex seals*: these are metallic rings (e.g. Silver or Aluminium) that deform under a certain compressing load to assure the sealing of the tank. To achieve this compressive load, the external titanium cover are fasten to the CF40 flange with eight M4 titanium bolts tightened with a prescribed torque. A CAD drawing of such a prototype and a picture of it after assembly can be seen in Figures 7.9 and 7.10, respectively.

The two main features of the realized design are as follows:

Each prototype reproduces the *mechanical* interfaces and environment of an optical window on a LISA-like vacuum tank, represented schematically in Figure 7.6. This allows to test the vacuum sealing of the assembly, as reported in [77] in combination with environmental tests such as shaking and thermal cycling.

At the same time the relatively small prototypes can be placed as transmissive elements in an optical bench to measure their interferometric response as described in Section 7.4.7 and investigate any effects in their long-term stability (e.g induced by the environmental testing) as described in Section 7.5.

7.4.4. Experimental set-up

Four temperature sensors with negative temperature coefficient (NTC) were placed on the optical window prototypes, two on the titanium and two on the glass, as shown in Figure 7.10. This way, information regarding the spatial temperature distribution on each material (glass or titanium) is obtained.

One big Kapton heater was attached to each side of the prototype, as shown in Figure 7.11. A smaller heater was attached to the glass to vary its temperature independently from
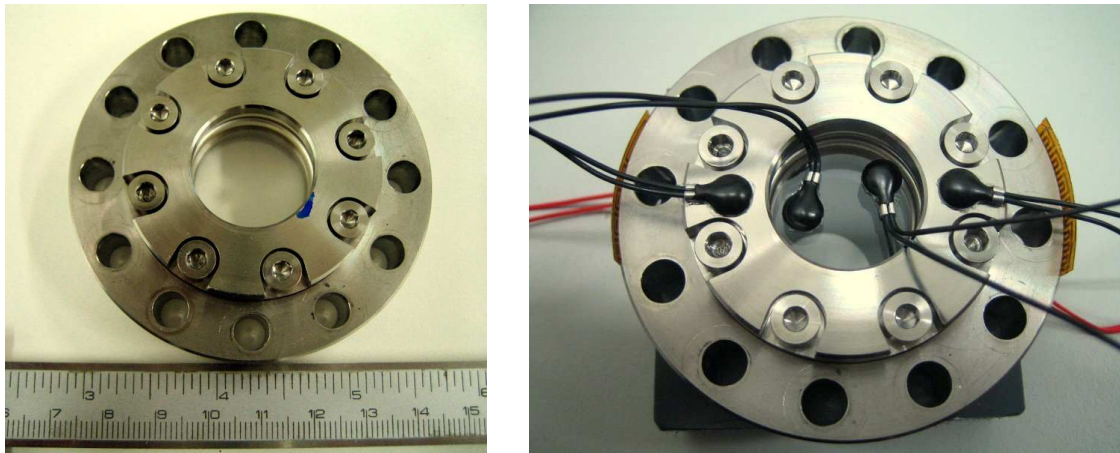
Figure 7.10: Left: Optical window assembly prototype as delivered by CGS. Right: Prototype with four NTC temperature sensors and two heaters attached.
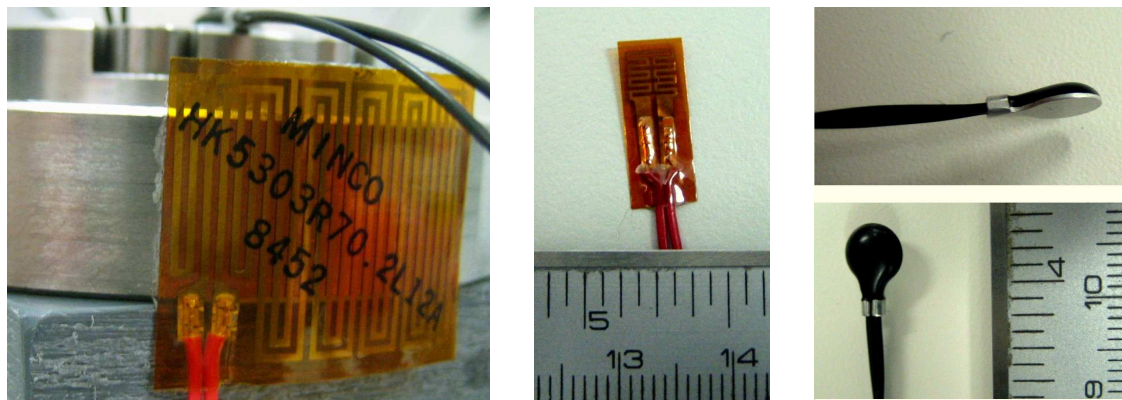
Figure 7.11: Left:Kapton heater attached to optical window prototype with adhesive transfer tape. Centre: small kapton heater. Right: NTC temperature sensors.

the titanium only for control purposes. Acrylic transfer tape (described below) was used to fix the sensors and heaters. The exact characteristics of the thermal elements used are:

- Sensor: BetaTherm G10K4D853 Glass Encapsulated NTC Thermistor (10 kΩ nominal resistance). Engineering models of the LTP temperature sensors.
- Heaters: MINCO HK5303R70.2L12A (70.2 Ω)
- Adhesive Transfer Tape: 3M 966 tape with acrylic adhesive 100

Experience from past test campaigns in which different, non-representative optical window prototypes were tested showed that special care has to be taken to avoid effects of radiation and to assure proper thermal contact between the heaters, the test body and the sensors. This improves accuracy and reproducibility between tests performed on different prototypes. For the measurements presented here, thermal contact was ensured in the following ways:

Use of acrylic transfer tape (recommended by ESA), which is specially designed for mechanical stability and thermal contact. It also presents a very low level of outgassing.

Use of flexible kapton heaters (recommended by EADS Astrium and ESA), which adapt perfectly to flat and curved surfaces and also have very low outgassing.

Use of NTC sensors (see Figure 7.11) designed with a glass encapsulation on one face to insulate them from any external influence. The other flat metallic face allows them to be mounted with large contact surface on a flat test body.

To minimise the effects of thermal radiation during the measurements, the heaters were covered with aluminium tape avoiding direct contact with the heating surface as shown in Figure 7.12, and the prepared prototype was covered with a brass box with a hole for the laser beam (not shown in Figure 7.12 for clarity).
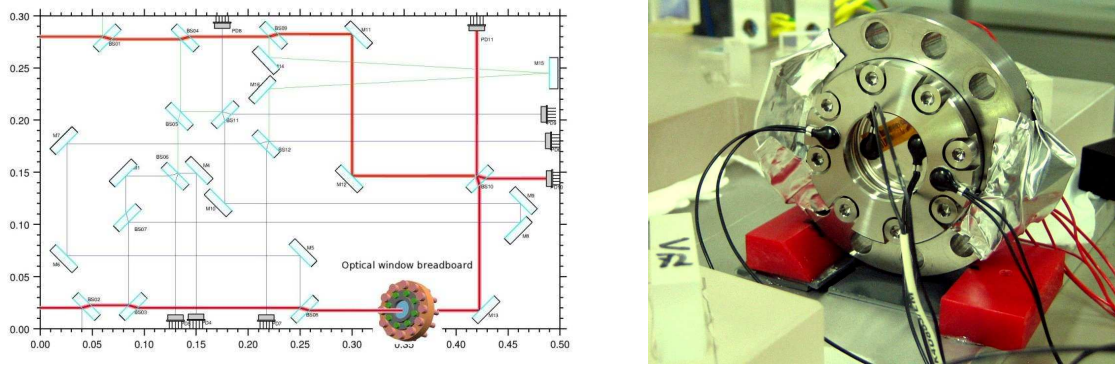
Figure 7.12: Left: schematic of the interferometric layout used to characterise the OW breadboards. Right: Breadboard positioned as transmissive element of the dedicated optical bench inside a vacuum chamber.

Temperature readout was done with a breadboard prototype of the LTP front-end electronics for temperature measurements, described in [78]. The temperature sensitivity of $10^{-5}\,\mathrm{K}/\sqrt{\mathrm{Hz}}$ at $1\,\mathrm{mHz}$ required for LTP has been recently demonstrated with a version of these electronics in combination with the NTC sensors mentioned before.

The breadboards were mounted inside a vacuum tank on a dedicated ultra-stable optical bench, similar to the LTP EM optical bench. It was specifically designed to test optical components in transmission and reflection and a detailed description of it can be found in [79]. Figure 7.12 shows an OptoCAD scheme of its optical layout with a window prototype as transmissive element and an actual picture of the set-up.

The readout of the interferometer phase takes place in the same set-up as with the LTP interferometer described in Chapter 2. All the components used for the LTP interferometry were used here with exception of the LTP EM optical bench: Laser, modulation bench and electronics, phasemeter and phasemeter back-end processing.

7.4.5. Temperature measurements

Heat pulses were applied to the optical window via the lateral heaters described in Section 7.4.4. The duration and intensity of the pulses was varied and the heaters were used both alternatively and simultaneously. The evolution of the temperature during two of these pulses can be seen in Figure 7.13 and is described below. The temperature change induced by each heat pulse was measured by the temperature sensor closest to the heater, allowing the estimation of the heat capacity of the prototypes. Several values of the heat capacity for different heating times and powers are shown in Table 7.3. These values are in agreement with the specific heat capacity of Titanium for a typical prototype mass of ≈ 200 g and are reproducible on all three breadboards, thus showing the validity of the measurement principle. The invariance of the heat capacity with respect to heating power or time shows that the system behaves linearly, which will be of great use when modelling the interferometric response of the window.

Table 7.3: Estimation of the heat capacity of OW prototypes to heat pulses.

Time [s]	Δ T[K] P = 2 W	Δ T[K] P = 1W	Heat capacity [J/K] P = 1 W	Heat capacity [J/K] P = 2 W
10	0.22	0.11	90.9	90.9
50	1.1	0.54	90.9	92.6
100	2.1	1.1	95.2	90.9

7.4.6. Phase measurements

The evolution of the window optical pathlength along with temperature variations can be seen in Figure 7.13.

The phase φ shown here was measured with the LTP-like phase readout described in Chapter 2, and its correspondence with the interferometric optical pathlength s, presented in Section 7.3, is given by

$$\varphi = \frac{2\pi s}{\lambda}. \tag{7.27}$$

The pathlength behaviour is clearly correlated to temperature variations in the optical window. Each pulse causes a rapid temperature increase around the heater which later relaxes as the temperature homogenises. A fast transient followed by a relaxation is also observed in the phase. The similarity between the profile of temperature and phase suggests a linear dependence between them. This was reproducible with all three optical window prototypes for a wide range of power and duration of the heating pulses. Typical values for temperature and phase increases for different heating configurations are shown in Table 7.4 and Figure 7.14.
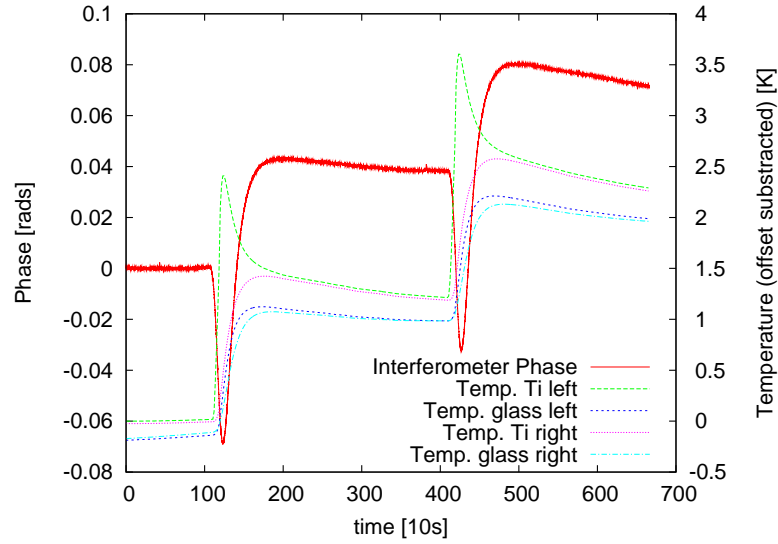
Figure 7.13: Optical window phase response to a heat pulse of 2W applied on a side heater.
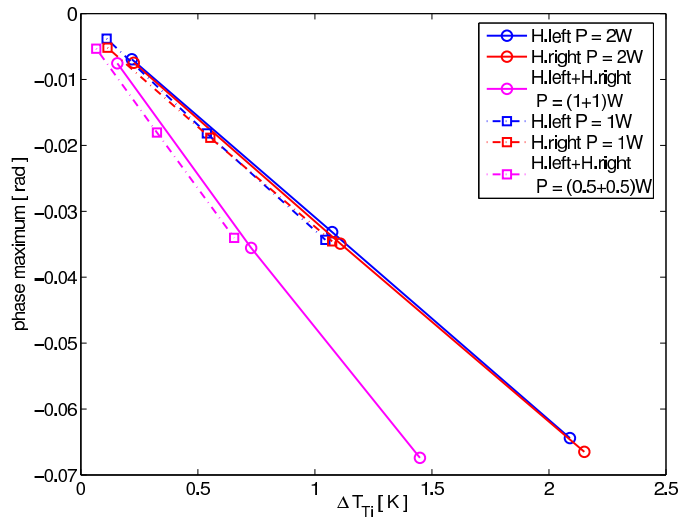
Figure 7.14: Relation between titanium temperature and phase peak values, extracted from Table 7.4.

Table 7.4: Thermal and optical response for different heating pulses. Phase maxima and ΔT_{Ti} values correspond to the peak values of phase and titanium temperature for different runs. Temperature peaks correspond to the sensor closest to the heater when heating on one side and average of both sensors when heating on both sides.

Heater	Power [W]	Heating time [s]	phase maximum [rad]	ΔT_{Ti} [K]
H.left	2	10	-0.007	0.218
	2	50	-0.033	1.074
	2	100	-0.064	2.090
	1	10	-0.004	0.110
	1	50	-0.018	0.539
	1	100	-0.034	1.045
H.right	2	10	-0.007	0.218
	2	50	-0.035	1.070
	2	100	-0.066	2.090
	1	10	-0.005	0.114
	1	50	-0.019	0.553
	1	100	-0.035	1.074
H.left+H.right	1+1	10	-0.008	0.156
	1+1	50	-0.036	0.730
	1+1	100	-0.067	1.450
	0.1+0.1	1000	-0.016	0.584
	0.5+0.5	10	-0.005	0.066
	0.5+0.5	50	-0.018	0.325
	0.5+0.5	100	-0.034	0.655
	0.05+0.05	1000	-0.015	0.696

The measured phase increase for each temperature step shown in Table 7.4 and plotted in Figure 7.14 constitute a first attempt to model the relationship between phase and temperature, as there is a clear linear dependence between the maximum increase in temperature near the heater used and the maximum increase in phase. Although it delivers a valid estimation for the order of magnitude of the effect, this relationship depends on the heating scheme, as it takes only the temperature near the active heater(s) into account. This is evident from the different slopes in Figure 7.14 for heating with one heater and with two heaters. This indicates the necessity for a more complex model that includes every temperature readout for each run and the complete evolution of the system instead of only the peak values of temperature and phase. Such a model is presented in the next section.

7.4.7. Optical window model

In order to investigate the influence of the temperature on the optical pathlength φ, the following model is proposed:

$$\phi = p_0 + p_1 \cdot t + p_2 \cdot \frac{T_{\mathrm{Ti_L}} + T_{\mathrm{Ti_R}}}{2} + p_3 \cdot \frac{T_{\mathrm{Gl_L}} + T_{\mathrm{Gl_R}}}{2} \tag{7.28}$$

where
$T_{\mathrm{Ti_L}}$ is the temperature on the left titanium sensor,
$T_{\mathrm{Ti_R}}$ the temperature on the right titanium sensor,
$T_{\mathrm{Gl_L}}$ the temperature on the left glass sensor,
$T_{\mathrm{Gl_R}}$ the temperature on the right glass sensor,
p_0, p_1 the fit coefficients of an initial value and a linear trend,
p_2: the fit coefficient between phase and mean temperature on the titanium, and
p_3: the fit coefficient between phase and mean temperature on the glass.

The first two terms of the model account for linear drifts in the phase. They need to be included in the model because such a linear fit only produces reasonable results if most of the RMS of the measured quantity (phase in our case) is explained by the model, even if these contributions are not interesting. The second two terms represent the mean temperature in the titanium and the glass, so that their associated fit coefficients p_2 and p_3 are the most interesting results. The validity of the model was tested on several runs where different heating configurations were applied to two optical breadboards: different heat powers (1 W and 2 W) were applied during various durations (10 s, 50 s and 100 s) on right and left heaters. It was possible to reproduce the phase behaviour for each run of the data set, and two examples of the fit performance are shown in Figures 7.15 and 7.16. The application of this model to each of the runs listed in Table 7.4 yields one set of parameters p_2 and p_3, allowing the estimation of the mean values $\bar{p}_2$ and $\bar{p}_3$ listed in Table 7.5.

Apart from the expression shown in Equation (7.28), several other terms were proposed to model the data to include temperature gradients of the type $p_4 (T_{\mathrm{Ti_L}} - T_{\mathrm{Ti_R}})$ among others, but the best description of the data was achieved with the model presented here.

Coupling coefficient	Value [mrad/K]	Correspondence
$\bar{p}_2$	(-70 ± 4)	titanium temperature
$\bar{p}_3$	(91 ± 15)	glass temperature

Table 7.5: Average value of the model coefficients for the study of the complete set of runs.

The different signs of the coupling coefficients p_2 and p_3 indicate that a temperature change in the titanium has the opposite effect of a temperature change in the glass. The contribution of the glass can be interpreted as a pure thermal expansion of the material and has been confirmed by directly changing its temperature with the small kapton heater shown in Figure 7.11.
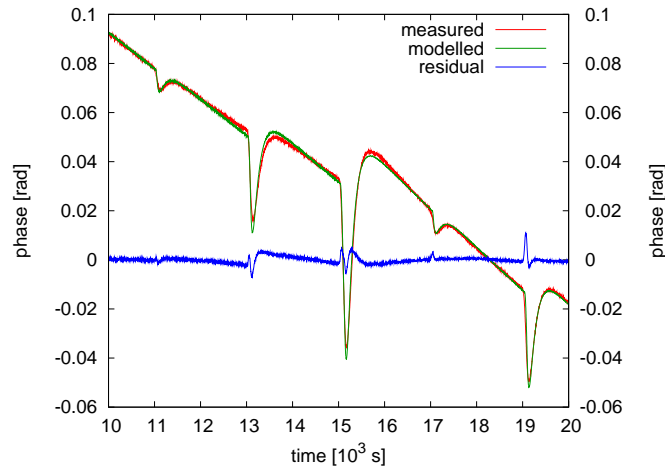
Figure 7.15: The model from equation 7.28 is used to fit a long run that includes heat pulses of different power and duration. Measured, fitted and residual phase are shown.
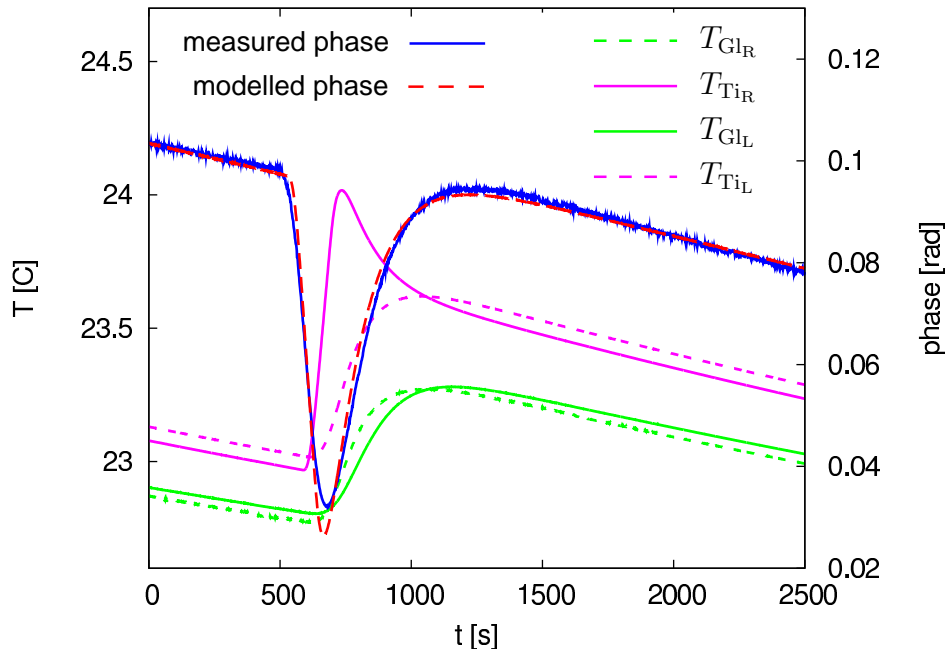
Figure 7.16: Detail of the behaviour of the system during one pulse of 2 W during 100 s applied on a side heater. The measured and fitted phase are shown together with the temperature readouts.

118

The coupling coefficient of glass temperature $p_3 = 90\,\mathrm{mrad/K}$ has to be compared with the prediction for the naked glass of $21\,\mathrm{mrad/K}$ from Equation (7.13) or the measurement of $25\,\mathrm{mrad/K}$ presented in Section 7.4.2. There has to be a different effect that accounts for the difference between 25 and $90\,\mathrm{mrad/K}$. This effect has to be considered as the influence of rather homogeneous temperature distribution in the whole prototype, as the heat has to go first through the titanium. In this sense, the extra influence must originate from stress caused by the different thermal expansion coefficient of the two bodies.

On the other hand, the contribution from the titanium described by p_2 is more complicated. As explained in Section 7.4.3, the metallic part of the prototype is actually made of three different materials (titanium body, bolts and helicoflex seals) with different expansion coefficients. When the temperature increases in a non homogeneous way, the sealing pre-load applied by the helicoflex on the optical glass (see Figure 7.6) also increases, reducing the window optical pathlength.

7.4.8. Conclusion

The thermally induced pathlength variations in the LTP interferometry are to be deduced from the coefficients obtained with the fit procedure. The direct approach of adding the coefficients p_2 and p_3 would lead to a general coupling coefficient of approximately $20\,\mathrm{mrad/K}$, but this would implicitly assume a perfectly homogeneous temperature distribution in the glass and the surrounding materials. This assumption is probably meaningful for frequencies near DC, but cannot hold for arbitrarily high frequencies. Taking this into account, a more conservative approach will be followed, consisting in adding both coefficients quadratically as if the effects were independent. This way, the general influence of the optical window temperature in the readout phase can be regarded to account for $\approx 114\,\mathrm{mrad/K}$. If we consider the optical layout of the shown in Figure 7.2, where the laser beam passes four times through an optical window this coefficient becomes $\approx 400\,\mathrm{mrad/K}$.

Using this coupling coefficient to estimate the required thermal stability so that the induced pathlength fluctuations remain below $1\,\mathrm{pm}/\sqrt{\mathrm{Hz}}$ (approx. $6\,\mu\mathrm{rad}/\sqrt{\mathrm{Hz}}$) results in $1 \times 10^{-5}\mathrm{K}/\sqrt{\mathrm{Hz}}$.

This constitutes a conservative upper-limit estimate of the effects of temperature change in the optical window pathlength, as the heating contributions in LTP are expected to be more homogeneous than the ones tested in the laboratory, thus reducing the stress related contribution.

Further development in the design of the optical window assembly to reduce the stress related contribution could be:

- Selection of the opto-mechanical glass properties to minimise the response to external stress. This is difficult to achieve due to the lack of information of the parameters that are critical for this effect, as explained in Section 7.3.4.

- Substitution of the external helicoflex seal shown in Figure 7.9 and 7.6 by a stress absorbing material such as UHV compatible rubber, as only the internal helicoflex ring acts as seal between the optical window and the vacuum enclosure.

7.5. Long-term stability

The long-term behaviour of the optical window was tested with the engineering model of the LTP interferometer, equipment and phase readout described in Chapter 2. The aim of the measurement was to investigate a possible degradation of the interferometric readout performance when the optical window is present in the beam path by any effect not mentioned in Section 7.3. These could be related to stress in the anti-reflection (AR) coating of the glass or to settling mechanisms between the different materials after the mechanical stress previous to the science phase of the mission (launch, orbit transfer,...). Also the appearance of stray-light or ghost reflections in the beam path cannot be completely discarded. To investigate this effects, the final LTP configuration was reproduced as closely as possible, including environmental testing of the prototypes.

No investigations of the optical window aperture in combination with test mass jitter were performed. This is because the risk of beam clipping at the aperture of the optical window is very small in comparison with the hole in the test mass electrode housing. Investigations of the effect of the electrode housing in combination with test mass jitter, for which the static dummy mirrors used here were replaced by steerable piezo-mounted ones were done after this work [80].

7.5.1. Set-up

As shown in Figure 7.17, one prototype at a time was attached to the side of the OB plate in front of the dummy mirror that acted as TM2, thus becoming a transmissive element in the LTP interferometer X12. This way the readout of the TM1 position fluctuations by the interferometer X1 was an independent indicator of the interferometric performance.

7.5.2. Initial results

The performance measured with the configuration described before can be seen in Figure 7.18. No influence of the optical window can be detected in the readout of the position fluctuations of the X12 interferometer. The sensitivity presented here is comparable to the best performance achieved with this system.

7.5.3. Influence of coatings and environmental tests

Several modifications were done to the optical window prototypes and the test set-up in order to study the influence of the optical window on the interferometric performance
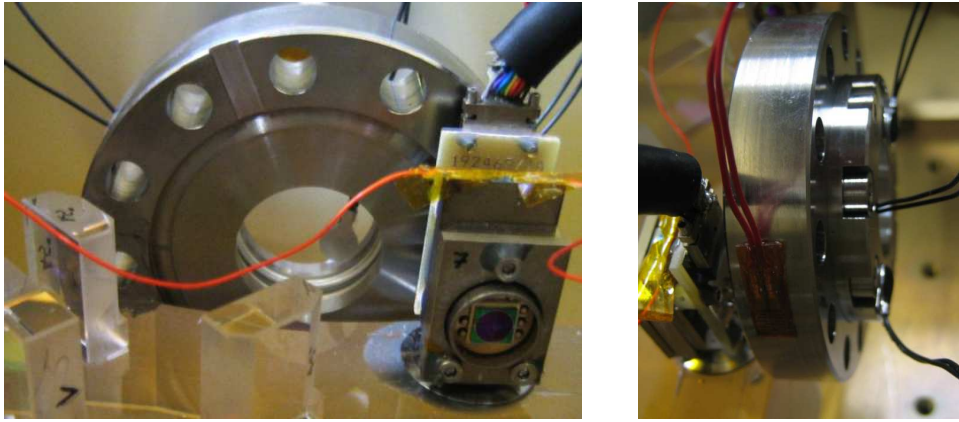
Figure 7.17: Front and side view of the OW breadboard attached (glued) to the Engineering Model of the LTP optical bench.

under conditions as similar as possible to those expected in LTP.

- AR coated glass: three new optical window breadboards were assembled using the Ohara glass with a dielectric anti-reflection (AR) coating.
- The new three samples (SN1, SN2 and SN3) went through various environmental tests:
  - SN1: assembly and leak test
  - SN2: random vibration and thermal cycling before being leak tested
  - SN3: bake-out and leak test.
- Modification of the experimental set-up: a wedged spacer made of steel was included between the optical bench plate and the window to avoid normal incidence of the beam on the glass by realizing a tilt angel of 2.5° similar to the LTP design (see Figure 7.19).

Several performance measurements were done with each optical window sample after they had been attached to the optical bench via the wedged spacer. As shown in Figures 7.20, 7.21 and 7.22 (one per optical window breadboard), no degradation of the performance was detected in the interferometer X12 with respect to X1. Each figure shows the performance of the X12 interferometer (where a optical window prototype was placed in front of the dummy mirror acting as test mass) and the performance of the X1 interferometer (where no optical window is present). There is also a third curve showing the best performance measured with the EM for comparison.

7.5.4. Experimental determination of temperature influence

In section 7.4 it was described how temperature variations were applied to the different optical window prototypes while the optical pathlength was monitored. Those measurements were used to model the noise contribution of temperature fluctuations in the LTP interferometric sensitivity. In a different experiment presented in Section 7.5, each optical
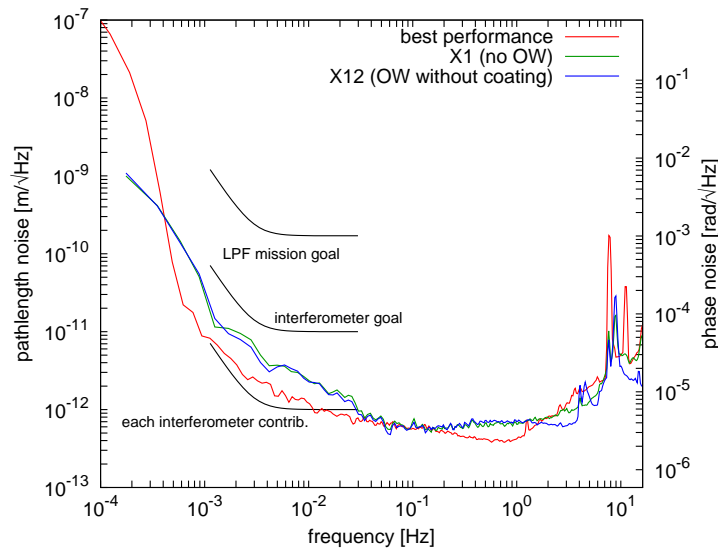
Figure 7.18: Sensitivity of the LTP interferometer and phasemeter system with a non coated optical window prototype in interferometer X12. Red: best performance. Green: performance of the X1 interferometer (without optical window). Blue: Performance of the X12 interferometer (with optical window).

window prototype was placed on the LTP EM OB and the long-term sensitivity of the interferometric system was characterised. The environmental temperature fluctuations were simultaneously monitored with NTC sensors attached to the OW prototype an the optical bench. The ones attached to the OW can be seen in Figure 7.17.

In this section the model mentioned earlier will be used to make a noise projection of the environmental temperature fluctuations on the measured stability. This way we will corroborate the validity of the upper limits deduced from the model in Section 7.4.7 and investigate under which conditions the interferometric stability is limited by environmental temperature fluctuations.

Environmental temperature fluctuations

Several temperature sensors were attached to the optical window prototypes and to the engineering model optical bench during the performance measurements shown in Section 7.5, as can be seen in Figure 7.17. The aim of these sensors was to monitor the environmental temperature during each long run.

The result is shown in Figure 7.23 as the following five temperature fluctuations: the upper curve, labelled "laboratory" shows the environmental temperature fluctuations outside the vacuum tank. The next curve labelled "OW" represents the temperature fluctuations on the optical window during the performance measurement shown in Figure 7.18, and similarly for the curve labelled "OB" referring to the optical bench. These two curves were measured with the LTP sensors and readout electronics used in Section 7.4.4. The
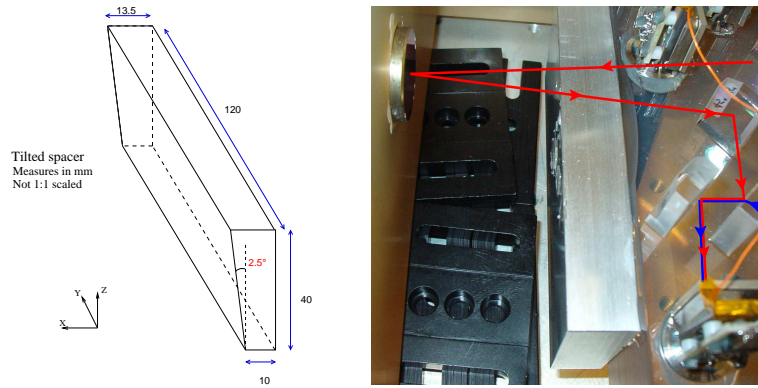
Figure 7.19: Left: Design of the tilted spacer. Right: spacer glued to the OB.

ratio between the temperature fluctuations outside the vacuum tank and the ones on the optical bench shows a strong temperature isolation of almost four orders of magnitude in the relevant frequency range. This results in the necessary temperature stability for the interferometric tests of $10^{-4}\mathrm{K}/\sqrt{\mathrm{Hz}}$ at $1\,\mathrm{mHz}$.

Finally, the last two curves show the sensitivity of the temperature acquisition system: the curve labelled "readout noise" was obtained during the same run by feeding the readout electronics with a fixed resistor with low temperature coefficient (0.6 ppm/K, from Vishay tech.) instead of a NTC sensor. The noise contribution from the NTC sensors during the measurement is more difficult to estimate: the last curve, labelled "sensor noise", was measured in a different setup with specially stable temperature conditions ($\approx 10^{-6}\mathrm{K}/\sqrt{\mathrm{Hz}}$) by the team responsible for this LTP diagnostics system [81]. Although this is the best possible estimation of the sensor noise in the rest of the curves shown in Figure 7.23, it represents only a lower limit, as the sensor noise in laboratory conditions may be affected by up-conversion into the LTP band of the large temperature drifts that occur at lower frequencies.

Noise projection

The temperature stability data presented in Figure 7.23 were multiplied by a factor of 200 mrad/K to obtain the projected phase noise shown as the lowest curve in Figure 7.24 (the coupling coefficient determined in Section 7.4.7 for the LTP interferometry was 400 mrad/K but we have here only one window in the optical path). The phase stability data from this run are shown for comparison.

The predicted phase noise is lower than the measured stability for frequencies below 30 mHz and reaches comparable levels for higher frequencies. It is important to remember that the model was, as stated in Section 7.4.7, a conservative upper limit, so that the phase noise actually caused by temperature fluctuations is expected to be lower. At frequencies higher than 0.1 Hz, both the external fluctuations are smaller and the filtering action better, such that the measured noise level is probably dominated by sensor noise and not
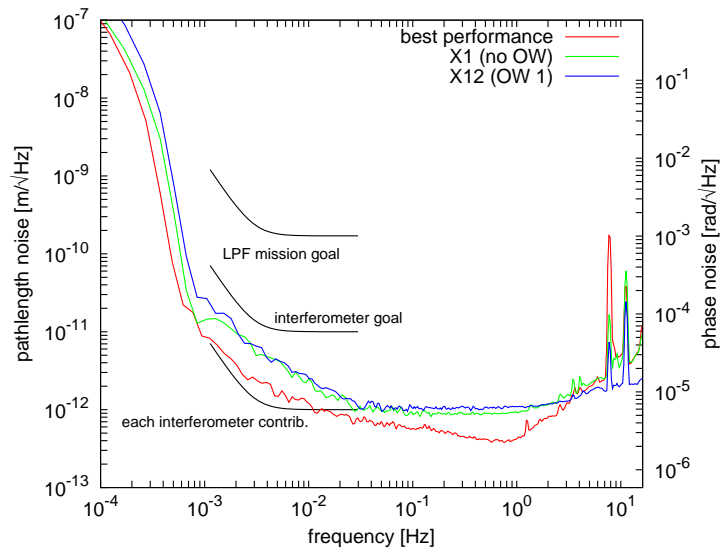
Figure 7.20: Sensitivity of the LTP interferometer and phasemeter system with AR-coated SN1 (no environmental test). Red: best performance. Green: performance of the X1 interferometer (without optical window). Blue: Performance of the X12 interferometer (with optical window).
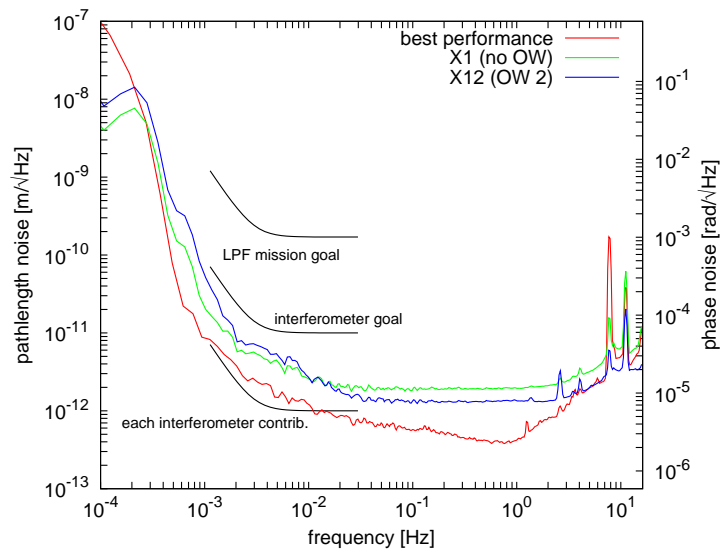
Figure 7.21: Sensitivity of the LTP interferometer and phasemeter system with AR-coated SN2 (undergone baking out). Red: best performance. Green: performance of the X1 interferometer (without optical window). Blue: Performance of the X12 interferometer (with optical window).
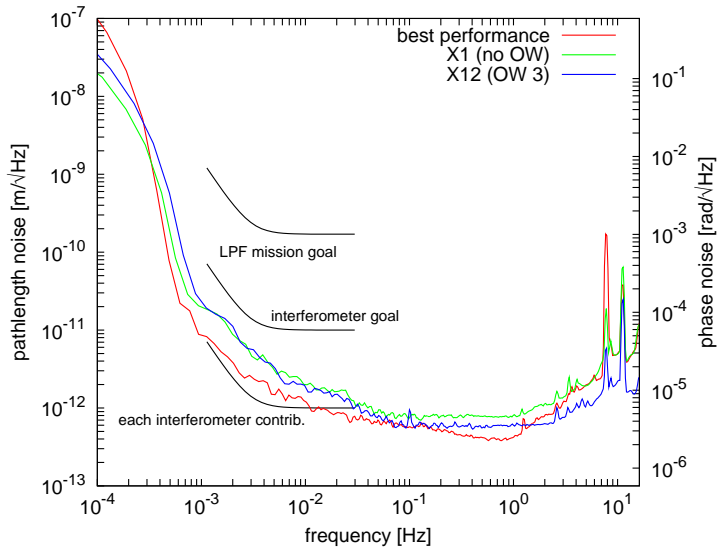
Figure 7.22: Sensitivity of the LTP interferometer and phasemeter system with AR-coated SN3 (undergone random vibration and thermal cycling). Red: best performance. Green: performance of the X1 interferometer (without optical window). Blue: Performance of the X12 interferometer (with optical window).
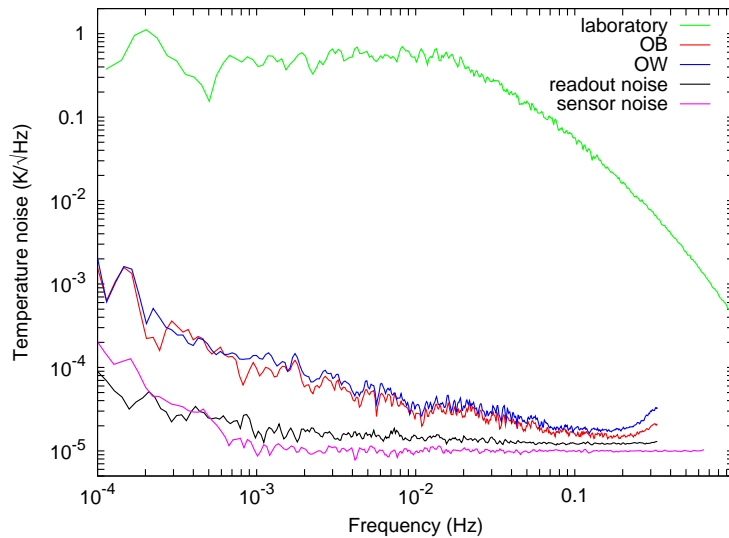
Figure 7.23: Temperature stability during a long run. The curves labelled "OW" and "OB" where measured during the performance measurement shown in Figure 7.18. Each of them corresponds to a different NTC sensor, one placed on the optical window prototype (see Figure 7.17) and the other placed in the engineering model of the optical bench. For comparison, the typical temperature fluctuations outside the vacuum tank are also shown. The curve labelled "readout noise" was obtained with a fixed resistor instead of an NTC sensor at the readout input. The curve labelled "sensor noise" was measured in a more stable temperature environment.
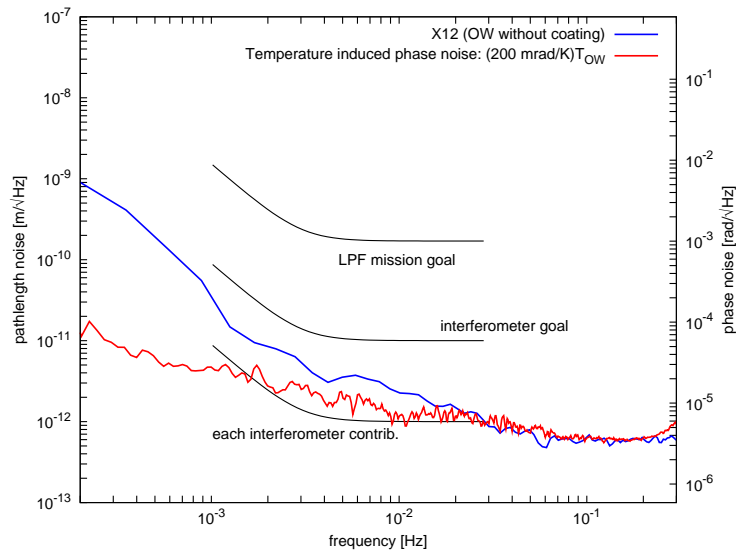
Figure 7.24: Projection of the measured temperature noise on the phase by means of the model presented in Section 7.4.7. The frequency range has been reduced with respect to earlier phase stability plots to match the range of available temperature data.

by real temperature fluctuations.

Furthermore, this noise projection confirms the model linearity in the range of micro Kelvin temperature fluctuations, which is the one relevant for LTP conditions. If the model linearity would not hold in this small fluctuations regime, higher phase noise should be detected.

7.6. Effects of ionising radiation on the optical glass

The degradation of the optical properties due to the radiation that the optical window will experience during the LTP mission is investigated in this section. The absorbed radiation dose has been estimated in [82] to be 12 krad. This calculation takes into account: 50 % margin, 17 months mission lifetime, shielding from satellite and vacuum enclosure (but not from optical bench).

The irradiation tests were performed at the Hahn-Meitner-Institute located in Berlin in the ISL (Ionen-Strahl-Labor which is German for Ion Beam Laboratory). The ISL offers ion beams from various accelerators and accelerator combinations with energies ranging from some tens of eV to some hundred MeV dedicated to the application of ion beam techniques in medicine, solid state physics, material science and biological science[83]. The 68.4 MeV proton beam is used for daily eye tumour therapy. To perform the material measurements as soon as possible, the ISL offered to do the testing over night with the same beam. The radiation tests were performed by Dr. Jens Reiche and Sascha Skorupka and the spectral transmission measurements presented in Section 7.6.3 were performed

by Dr. Jens Reiche.

7.6.1. Experimental Setup

The 68.4 Mev beam was guided to the ILS experimental physics laboratory by ion optics. This setup was done by ILS staff in the control centre. The beam size and alignment was checked, and then the beam energy was decelerated to 30 MeV by an 5 mm alloy shield. An aperture of 10 mm was used to select the homogenous part of the beam. Then a simple counter was calibrated to the number of particles. Afterwards the four probes were mounted in a metallic frame in front of the proton beam, as can be seen in the left part of Figure 7.25.

Each glass probe was radiated in four different locations with different radiation doses, as shown in the right part of Figure 7.25. To this end, the frame was placed in the corresponding position for a given exposure time per remote control. Before each radiation period it was checked that the beam would hit the probes at the right position. The radiation dose for each spot is listed in Table 7.6.
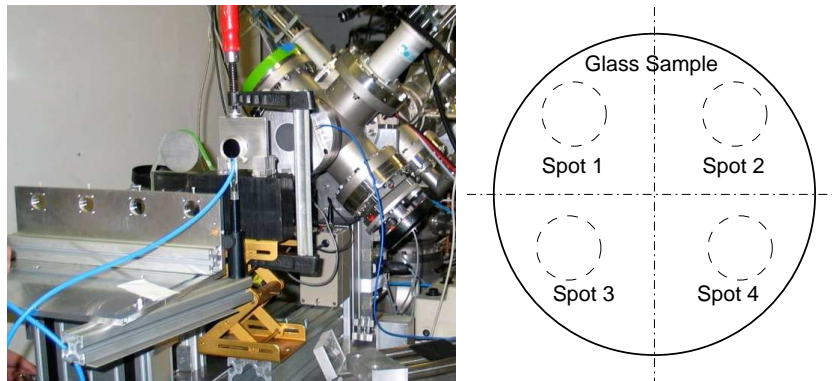
Figure 7.25: Left: Set-up for the radiation tests. The ion optics guide the proton beam to the glass samples. Right: Schematic view of one glass sample to be radiated in four different spots each one with a different dose.

7.6.2. Radiated samples

Pictures of the samples 2, 3 and 4 taken *just after the radiation tests* are shown in Figure 7.26. There is some darkening in the radiated spots. Sample number 3 (centre) shows the strongest darkening in the spot that was radiated with 200 krad. Sample number 4 (right) has an anti-reflection coating similar to the ones to be mounted on LTP. The observed darkening is due to the appearance of colour-centres, which are material defects caused by high energy particles.

The pictures of the radiated samples shown in Figure 7.27 were taken *two weeks* after the radiation tests. They do not show the annealing of the colour centres (or material

Table 7.6: Radiation dose distribution on the four glass samples.

Sample Number	Spot Position	Dose [Krad]
1	1	1
1	2	5
1	3	10
1	4	12
2	1	20
2	2	40
2	3	80
2	4	100
3	1	200
3	2	-
3	3	100
3	4	-
4 (AR-coated)	1	5
4 (AR-coated)	2	12
4 (AR-coated)	3	40
4 (AR-coated)	4	100

Figure 7.26: Samples number 2, 3, and 4 just after the tests. Darkening appeared in the spots radiated with high dose.

Figure 7.27: Samples number 2, 3, and 4 two weeks after the radiation tests. No spontaneous bleaching of the glass was observed.

bleaching) that can be found in the literature for other materials. Moreover, the annealing mechanisms described in the literature [84] are driven either by high temperature or external electromagnetic radiation, none of which are expected during the LPF mission

so that no bleaching effect are expected once colour centres appear.

7.6.3. Quantitative evaluation of the absorption

For a quantitative evaluation of the absorption caused by the colour centres in the radiated samples, several measurements of the light transmission through the samples were performed.

Absorption at 1064 nm

The absorption was measured with a Nd-YAG laser with the same properties (wavelength, polarisation and intensity) as in LTP. Figure 7.28 shows the experimental set-up: the laser beam power was detected by a photodiode after transmission through the glass sample. The position in which the beam hit the sample was scanned in the horizontal and vertical directions using the kinematic mount that was holding the sample. This way it was possible to determine the transmitted intensity in the four radiated spots and compare it with the transmission through a non irradiated sample. The results of the measurement are shown in Figure 7.29.
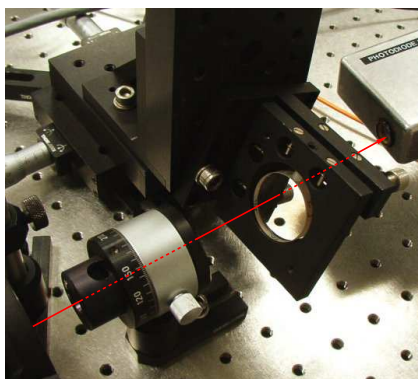
Figure 7.28: Experimental set-up of of the transmission measurements at 1064 nm.

The glass samples were tilted vertically with respect to the incoming beam by approximately 20° to avoid the formation of spurious cavities between the glass sample and the photodiode. This tilt slightly increased the length of the material to be traversed by the laser so that the results obtained here represent a worst case of the absorption in the material.

The detected absorption remained below 1.5 % even for a radiation dose of 200 krad.
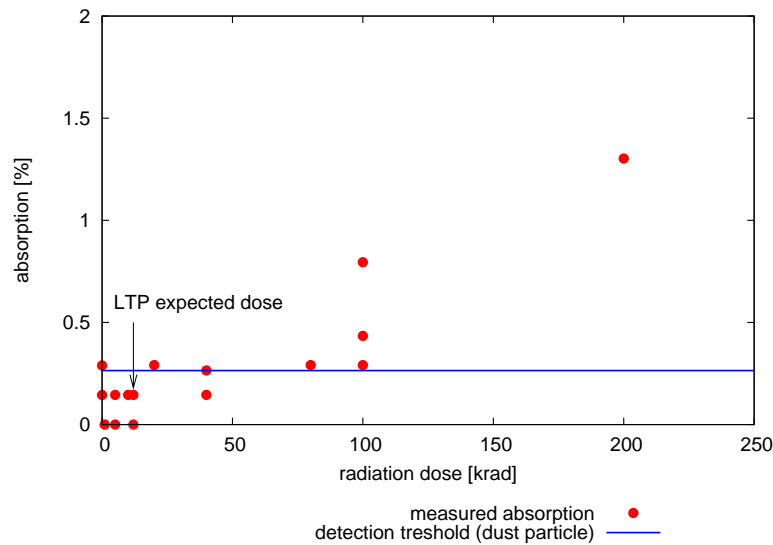
Figure 7.29: Relative absorption at 1064 nm for different radiation dose.

Absorption spectra

Relative transmission was also measured as a function of the wavelength with a spectrometer (Perkin Elmer UV/VIS/NIR Spectrometer Lambda 900) at the Laser Zentrum Hannover (LZH) facilities. Figure 7.30 shows the spectra of an AR coated and an uncoated sample in two different spots: the darkest spot (200 krad) and a non-irradiated area.
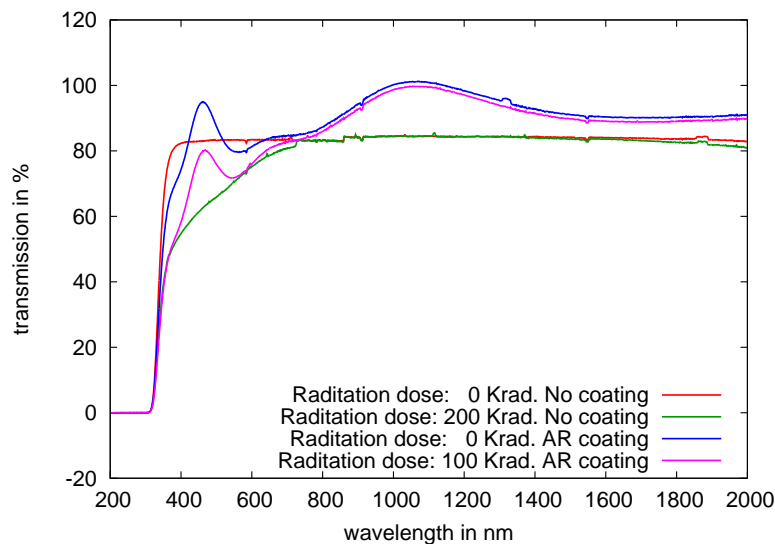
Figure 7.30: Absorption measured in a wide spectral range for two samples with and without anti-reflection coating.

The two spectra of the AR-coated window can be recognised due to its non-flat, improved transmittance around 1064 nm. In both samples, change in the absorption due to the radiation is only measurable for visible light with wavelengths well below 1064 nm, from 800 nm down to UV. Below 400 nm there is almost no transmission, as typically occurs with most glasses.

Another spectral measurement of the relative transmission through the sample radiated with 200 krad with respect to a non radiated samples can be seen in Figure 7.31. The experimental setup consists of a 1m-McPherson monochromator, and a slow-scan CCD camera from Princeton Instruments cooled with liquid nitrogen. At the laser wavelength of 1064 nm, the ratio between the transmission through the irradiated sample and the transmission through a non-irradiated sample is higher than 98 %, indicating less than 2 % transmission losses due to radiation.
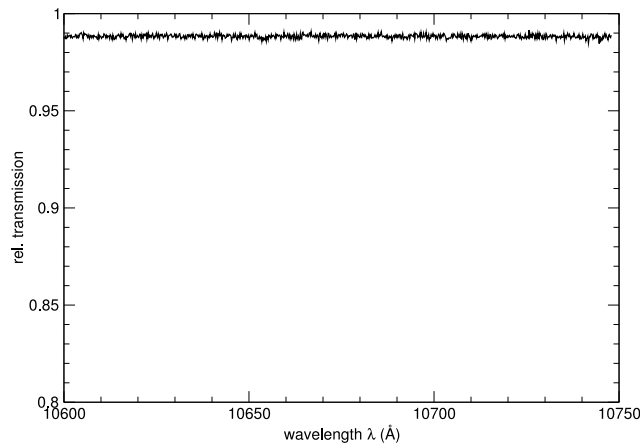
Figure 7.31: Absorption measured in a spectral range around the wavelength of interest with a 1m-McPherson monochromator.

A confirmation of the results presented here regarding radiation tests of the athermal glass Ohara S-PHM52 can be found in [85]. This reference describes proton radiation tests performed on the S-PHM52 with radiation dose up to 100 krad. The transmission spectra shown there are comparable to the ones measured by AEI, and the authors also conclude that there is "virtually no degradation in the IR wavelengths".

7.7. Conclusion

We have presented an analysis of the different factors concerning the optical window in LISA Pathfinder and LISA from the point of view of the interferometry. In this context, the main concern is the eventual degradation of the sensitivity due to excess noise from the optical pathlength of the window.

When analysing the possible effects that affect the pathlength stability in Section 7.3, it soon became clear that the special mounting of the glass as vacuum interface between test mass and optical bench makes it necessary to investigate the complete mechanical assembly, because of the combination of stress and thermal effects. It was decided to manufacture prototypes of assembled windows and experimentally determine their optical response to temperature variations.

Their response was characterised with a dedicated optical bench where they were placed as transmissive elements, as described in Section 7.4. Temperature steps were applied to the prototypes while their interferometric response was monitored, resulting in a model that relates temperature in the window and optical phase of the interferometer.

The main output from this model, as stated in Section 7.4.7, is an upper limit for the linear coupling between temperature fluctuations and induced phase noise for the LTP interferometer of 400 mrad/K. The temperature stability required to keep the associated phase noise under the typical requirement of $6\,\mu\mathrm{rad}/\sqrt{\mathrm{Hz}}$ level would be $1 \times 10^{-5}\mathrm{K}/\sqrt{\mathrm{Hz}}$. It was also found that two contributions account for most of the temperature related pathlength changes, namely the pure expansion and refractive index variations of the glass itself, and compression associated with differential thermal expansion of the materials surrounding it. Further improvements could be achieved in the thermal response of the assembly by matching the expansion coefficients of the materials more carefully or by including some stress absorbing material in the assembly such as rubber.

This kind of model relating the influence of environmental stimuli to interferometric output will play a major role in the scientific analysis of LISA and LISA Pathfinder data, so that they are object of ongoing refinement by several research groups. The latest advances of the model presented here —including frequency dependence of the coefficients— can be found in [86, 87].

In order to check for any effect that may not have been taken into account previously, the long-term behaviour of the optical window was tested with the engineering model LTP optical bench, and no degradation of the interferometric performance was detected with any of the prototypes. Furthermore, these measurements allowed to verify the validity of the model by means of noise projections, as described in Section 7.5.4.

A final aspect to be taken into account is the possible appearance of colour centres in the glass as consequence of the high radiation dose expected during the mission lifetime in space. Glass samples were radiated with representative dose levels to study this effect, as explained in Section 7.6. Although darkening was found in the visible spectrum — though for radiation dose much higher than the expected for LTP—, this darkening does not cause any appreciable loss of transmissivity at the wavelength of interest. This was also confirmed by existing literature [85].

From the investigations presented here it can be concluded that the inclusion of an optical window as described here in the interferometric design of LISA Pathfinder or LISA should not cause excess noise in the interferometric sensitivity of these missions.

Chapter 8.

Summary and outlook

The fundamental measurement of the LISA interferometry is one LISA arm, i.e. the measurement —with picometre precision in the LISA frequency range— of the fluctuations of the separation between two free-floating test masses in different satellites separated by 5 million km. The task is divided into two parts: determination of the position of each test mass with respect to the local optical bench and measurement of the distance between the local and the remote optical benches. The local part of this measurement will be tested by the LTP experiment onboard LISA Pathfinder.

In order to test the functionality and performance of the LISA technology pachage (LTP) interferometry, a test bed was implemented that resembles the LTP configuration except for the test masses, that have been substituted by gold coated mirrors. In its current status, this LTP test bed has demonstrated the required sensitivity to longitudinal test mass position fluctuations of $10\,\mathrm{pm}/\sqrt{\mathrm{Hz}}$ at $1\,\mathrm{mHz}$. The $100\,\mu\mathrm{rad}$ required dynamic range and $10\,\mathrm{nrad}/\sqrt{\mathrm{Hz}}$ alignment sensitivity have also been demonstrated. The next steps are the investigations of other interferometric elements and procedures on the way to the LTP flight model implementation and LISA.

A procedure to align the LTP test masses with respect to the interferometer was successfully designed and tested. Future implementation of the procedure will include refinement of the parameters to include the test mass dynamics.

The implementation of three laser stabilisation techniques —laser frequency, laser amplitude and optical pathlength difference (OPD)— and their influence on the final sensitivity of the LTP interferometry was also analysed. The main noise source to be stabilised consists of the non- linearities detected at the interferometric output and caused by electromagnetic pick-up from the modulation electronics. The influence of this non-linearities can be suppressed by stabilising the environmental pathlength difference fluctuations that affect all four LTP interferometers. A fall back option for a fibre-coupled actuator for the OPD stabilisation was also presented. This constitutes a robust laser phase modulator for large modulation index at low frequencies. The implementation of these stabilisations onboard LTP will also help to gather essential information for LISA about the fluctuations under study: frequency and amplitude stability of the laser and pathlength stability of optical fibres. The LTP frequency stabilisation could be directly implemented on LISA as one of the three foreseen stabilisation techniques.

The principle of the arm-locking frequency stabilisation technique for LISA was demonstrated with a hardware simulation of the LISA configuration. It was shown that the bandwidth of this kind of stabilisation is not limited to values far below the inverse of the light round-trip travel time, as was traditionally assumed. The performance of this kind of control loops is limited by processing delays present at the output of the phasemeter.

A different contribution to the pathlength noise is given by the optical windows of the vacuum enclosures containing the test masses, as they constitute the only transmissive element of the interferometer that is not bonded on an ultra stable optical bench. We have presented an analysis of the different factors concerning the optical window in LISA Pathfinder and LISA from the point of view of the interferometry. In this context, the main concern is the eventual degradation of the sensitivity due to excess noise from the optical pathlength of the window. In order to investigate their influence in the interferometric stability, optical window prototypes have been manufactured using a specially selected athermal glass. They were included in the optical path of the LTP test bed and no degradation of the interferometric performance was detected.

Another pathlength noise contribution in the interferometer axes is caused by cross-talk from the test masses degrees of freedom that are not monitored by the interferometer and thus show higher noise. One alternative under study is the optical readout of the test masses in these degrees of freedom. The principle of function of an optical readout technique based on a deep internal phase modulation has been demonstrated, including the measurement principles of position fluctuations and alignment. This technique brings much of the advantages of the LTP interferometry with a much more simpler modulation scheme.

It can be concluded, that the difficulties of local measurement of position fluctuations of the test masses are understood and the necessary sensitivity has been demonstrated. The next step will be the implementation of high precision interferometry with free-floating test masses using LISA Pathfinder.

The remote interferometry poses new challenges, such as Doppler shifts that make a new phasemeter necessary, the low incoming power in the remote satellite or the high frequency noise suppression required. Some of them have already been addressed, but many of them will have to be tested in the future, for which the experience gained with the LTP interferometry will surely prove very valuable.

Appendix A.

Evaluation of the optical response to temperature fluctuations of glass Ohara S-PHM52

The coupling of temperature fluctuations in the optical pathlength of the glass is given, as discussed in Section 7.3.1, by

$$\frac{1}{L}\frac{\mathrm{d}s}{\mathrm{d}T} = \left(\frac{\mathrm{d}n}{\mathrm{d}T} + (n-1)\alpha\right). \tag{A.1}$$

The linear thermal expansion coefficient is $\alpha = 10.1\,\mathrm{ppm/K}$. The refraction index at $1064\,\mathrm{nm}$, $n(1064) = 1.60645$, can be calculated with the Sellmeier dispersion formula:

$$n^2 - 1 = \frac{\mathrm{A}_1\lambda^2}{\lambda^2 - \mathrm{B}_1} + \frac{\mathrm{A}_2\lambda^2}{\lambda^2 - \mathrm{B}_2} + \frac{\mathrm{A}_3\lambda^2}{\lambda^2 - \mathrm{B}_3} \tag{A.2}$$

where the measured constants $\mathrm{A_i}$ and $\mathrm{B_i}$ are listed in Figure A.1. Several considerations have to be made to evaluate the term $\mathrm{d}n/\mathrm{d}T$, the temperature coefficient of the refractive index. We are interested in the fluctuations in vacuum (also called absolute) $\frac{\mathrm{d}n_{\mathrm{absolute}}}{\mathrm{d}T}$ but the ones listed in Figure A.1 have been measured at ambient air (101.3 kPa dry air) and are called relative $\frac{\mathrm{d}n_{\mathrm{relative}}}{\mathrm{d}T}$. To obtain the relation between them we write

$$n_{\mathrm{absolute}} = n_{\mathrm{relative}} \times n_{\mathrm{air}} \tag{A.3}$$

where n_{air} is the air refractive index. The absolute temperature coefficient $\frac{\mathrm{d}n_{\mathrm{absolute}}}{\mathrm{d}T}$ can be then obtained as the derivative of equation A.3:

$$\frac{\mathrm{d}n_{\mathrm{absolute}}}{\mathrm{d}T} = \frac{\mathrm{d}n_{\mathrm{relative}}}{\mathrm{d}T} + n_{\mathrm{absolute}}\frac{\mathrm{d}n_{\mathrm{air}}}{\mathrm{d}T}, \tag{A.4}$$

where the approximations $n_{\mathrm{air}} \approx 1$ and $n_{\mathrm{relative}} \approx n_{\mathrm{absolute}}$ have been made to suit the data available in Appendix A.1. The last step is to substitute the variables that appear in equation A.4 with values from Appendix A.1. These values are listed for different temperature ranges, so that the final result will be calculated as the mean between temperature ranges $0...20\,°$ and $20...40\,°$:

$$\frac{\mathrm{d}n_{\mathrm{absolute}}}{\mathrm{d}T} = \frac{1}{2}\left(\frac{\mathrm{d}n_{\mathrm{abs.}}}{\mathrm{d}T}(0\ldots 20\,°) + \frac{\mathrm{d}n_{\mathrm{abs.}}}{\mathrm{d}T}(20\ldots 40\,°)\right) = -5.54\,\mathrm{ppm/K}. \tag{A.5}$$

Finally,

$$\frac{1}{L}\frac{\mathrm{d}s}{\mathrm{d}T} = \left(\frac{\mathrm{d}n}{\mathrm{d}T} + (n-1)\alpha\right) = 0.59\,\mathrm{ppm/K}. \tag{A.6}$$

S-PHM52

Refractive Index	n_d	**1.61800** 1.618000	Abbe Number	v_d	**63.4** 63.33	Dispersion	n_F-n_C	**0.00975** 0.009758
Refractive Index	n_e	1.620327	Abbe Number	v_e	63.02	Dispersion	n_F'-$n_{C'}$	0.009844

Refractive Indicies		
$\lambda(\mu m)$		
n_{2325}	2.32542	1.59108
n_{1970}	1.97009	1.59587
n_{1530}	1.52958	1.60103
n_{1129}	1.12864	1.60561
n_t	1.01398	1.60714
n_s	0.85211	1.60983
$n_{A'}$	0.76819	1.61167
n_r	0.70652	1.61335
n_C	0.65627	1.61504
$n_{C'}$	0.64385	1.61551
n_{He-Ne}	0.6328	1.61595
n_D	0.58929	1.61791
n_d	0.58756	1.61800
n_e	0.54607	1.62033
n_F	0.48613	1.62479
$n_{F'}$	0.47999	1.62535
n_{He-Cd}	0.44157	1.62940
n_g	0.435835	1.63010
n_h	0.404656	1.63451
n_i	0.365015	1.64199

Partial Dispersions	
n_C-n_t	0.007893
n_C-$n_{A'}$	0.003370
n_d-n_C	0.002964
n_e-n_C	0.005291
n_g-n_d	0.012103
n_g-n_F	0.005309
n_h-n_g	0.004403
n_r-n_g	0.011891
n_C-n_t	0.008364
n_e-$n_{C'}$	0.004820
$n_{F'}$-n_e	0.005024
n_i-$n_{F'}$	0.016643

Relative Partial Dispersions	
$\theta_{C,t}$	0.8089
$\theta_{C,A'}$	0.3454
$\theta_{d,C}$	0.3038
$\theta_{e,C}$	0.5422
$\theta_{g,d}$	1.2403
$\theta_{g,F}$	0.5441
$\theta_{h,g}$	0.4512
$\theta_{i,g}$	1.2186
$\theta'_{C,t}$	0.8497
$\theta'_{e,C'}$	0.4896
$\theta'_{F,e}$	0.5104
$\theta'_{i,F}$	1.6907

Thermal Properties		
Strain Point StP (℃)		–
Annealing Point AP (℃)		–
Transformation Temperature Tg (℃)		587
Yield Point At (℃)		617
Softening Point SP (℃)		–
Expansion Coefficients (-30~+70℃)		101
α (10^{-7}/℃) (+100~+300℃)		120
Thermal Conductivity k (W/m·K)		0.599

Coloring			
λ_{80}	37	λ_5	33
λ_{70}			

Deviation of Relative Dispersions $\Delta\theta$ from "Normal"	
$\Delta\theta_{C,t}$	-0.0349
$\Delta\theta_{C,A'}$	-0.0072
$\Delta\theta_{g,d}$	0.0071
$\Delta\theta_{g,F}$	0.0051
$\Delta\theta_{i,g}$	0.0239

Mechanical Properties		
Young's Modulus E (10^8N/m²)	715	
Rigidity Modulus G (10^8N/m²)	277	
Poisson's Ratio σ	0.292	
Knoop Hardness Hk[Class]	390	4
Abrasion Aa	434	
Photoelastic Constant β (nm/cm/10^5Pa)	1.00	

Constants of Dispersion Formula	
A_1	1.09966550E+00
A_2	4.78125422E-01
A_3	1.13214074E+00
B_1	1.32718559E-02
B_2	-6.01649685E-04
B_3	1.30595472E+02

Chemical Properties	
Water Resistance(Powder) Group RW(P)	2
Acid Resistance(Powder) Group RA(P)	5
Weathering Resistance(Surface) Group W(S)	2
Acid Resistance(Surface) Group SR	5.0
Phosphate Resistance PR	4.0

Other Properties	
Bubble Quality Group B	
Specific Gravity d	3.67
Remarks	

Internal Transmittance	
λ(nm)	τ10mm
280	
290	
300	
310	
320	
330	0.05
340	0.25
350	0.51
360	0.72
370	0.85
380	0.923
390	0.957
400	0.974
420	0.986
440	0.990
460	0.992
480	0.994
500	0.996
550	0.998
600	0.998
650	0.998
700	0.998
800	0.997
900	0.996
1000	0.996
1200	0.996
1400	0.996
1600	0.991
1800	0.979
2000	0.961
2200	0.926
2400	0.89

Temperature Coefficients of Refractive Index							
Range of Temperature	dn/dt relative (10^{-6}/℃)						
(℃)	t	C'	He-Ne	D	e	F'	g
-40~-20	-3.7	-3.6	-3.6	-3.6	-3.4	-3.2	-3.0
-20~0	-3.8	-3.7	-3.7	-3.6	-3.5	-3.2	-3.0
0~20	-4.0	-3.7	-3.7	-3.6	-3.5	-3.2	-3.0
20~40	-4.1	-3.7	-3.7	-3.6	-3.5	-3.2	-3.0
40~60	-4.2	-3.8	-3.8	-3.6	-3.5	-3.2	-3.0
60~80	-4.2	-3.8	-3.8	-3.7	-3.6	-3.3	-3.0

OHARA 02-06

Figure A.1: Datasheet of the Ohara S-PHM52
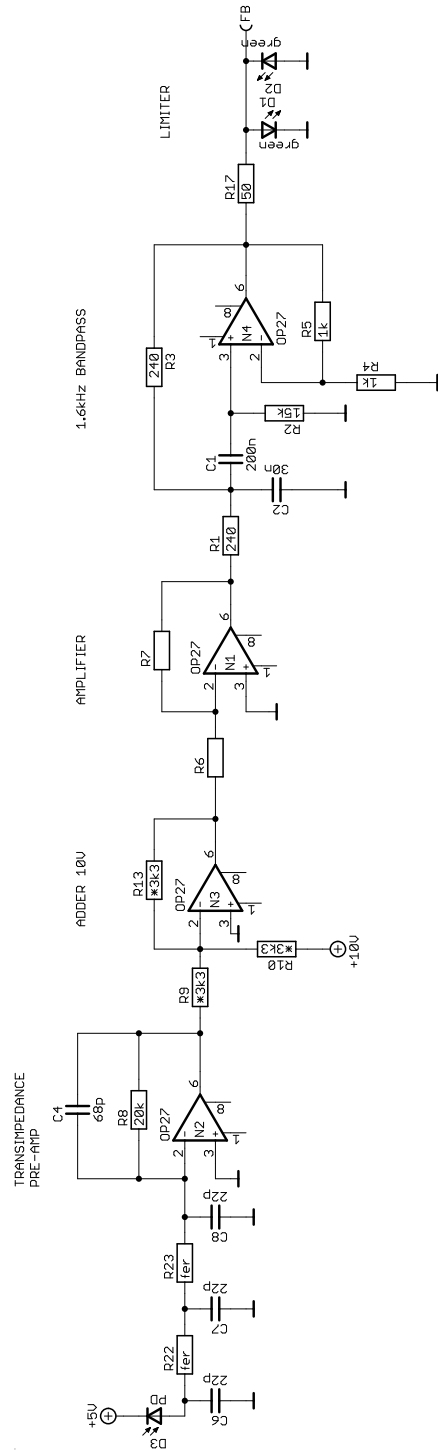
Appendix B.

Electronic layouts

Figure B.1: Circuit for the analog implementation of the amplitude stabilisation for the LTP interferometry presented in Section 5.2. It consists mainly of a band-pass filter with high gain at 1.6 kHz
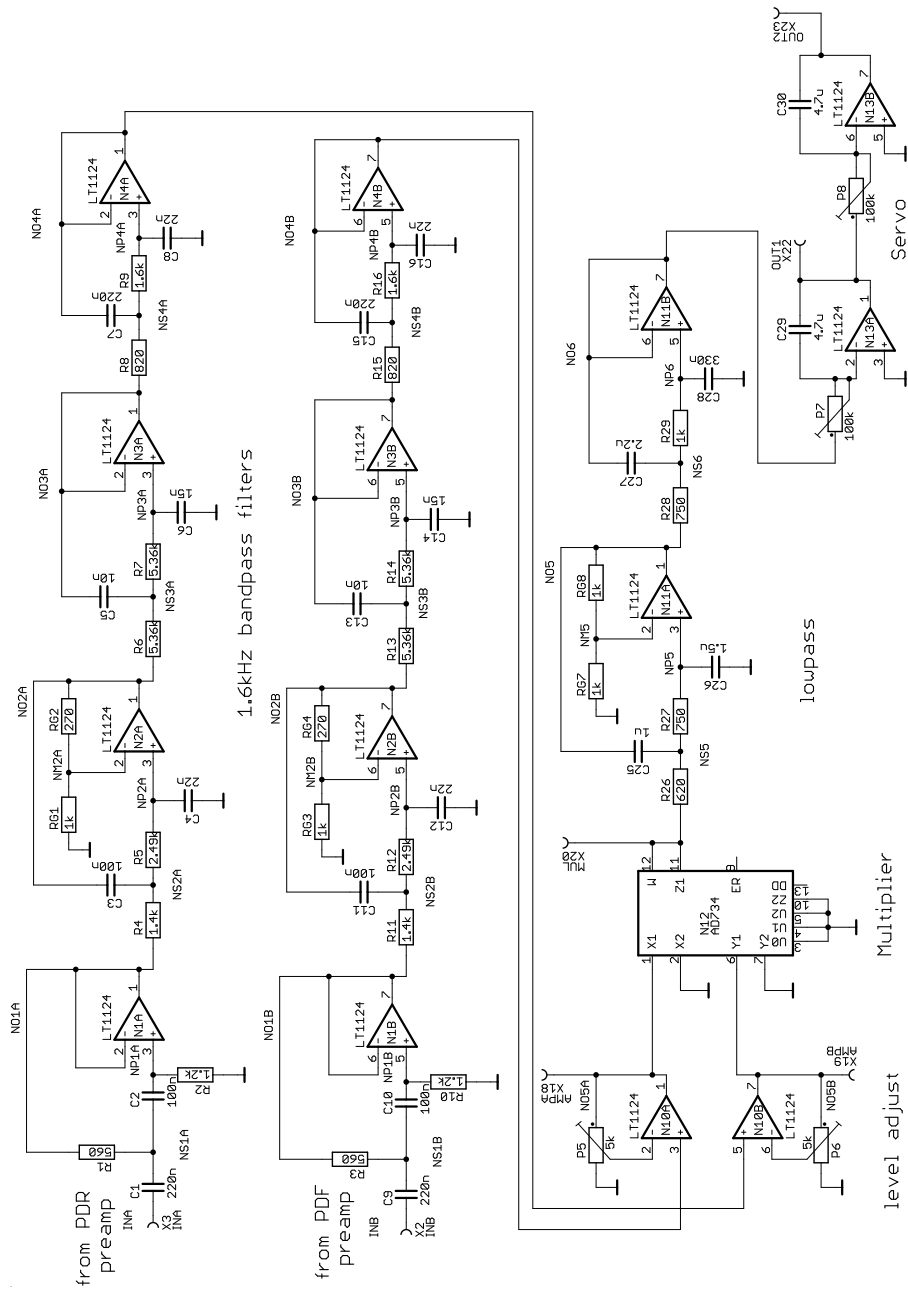
Figure B.2: Circuit for the analog implementation of the OPD and frequency stabilisation for the LTP interferometry. It consists of an analog phase difference detection between two input channels at 1.6 kHz, low-pass filter to suppress higher harmonics and servo.
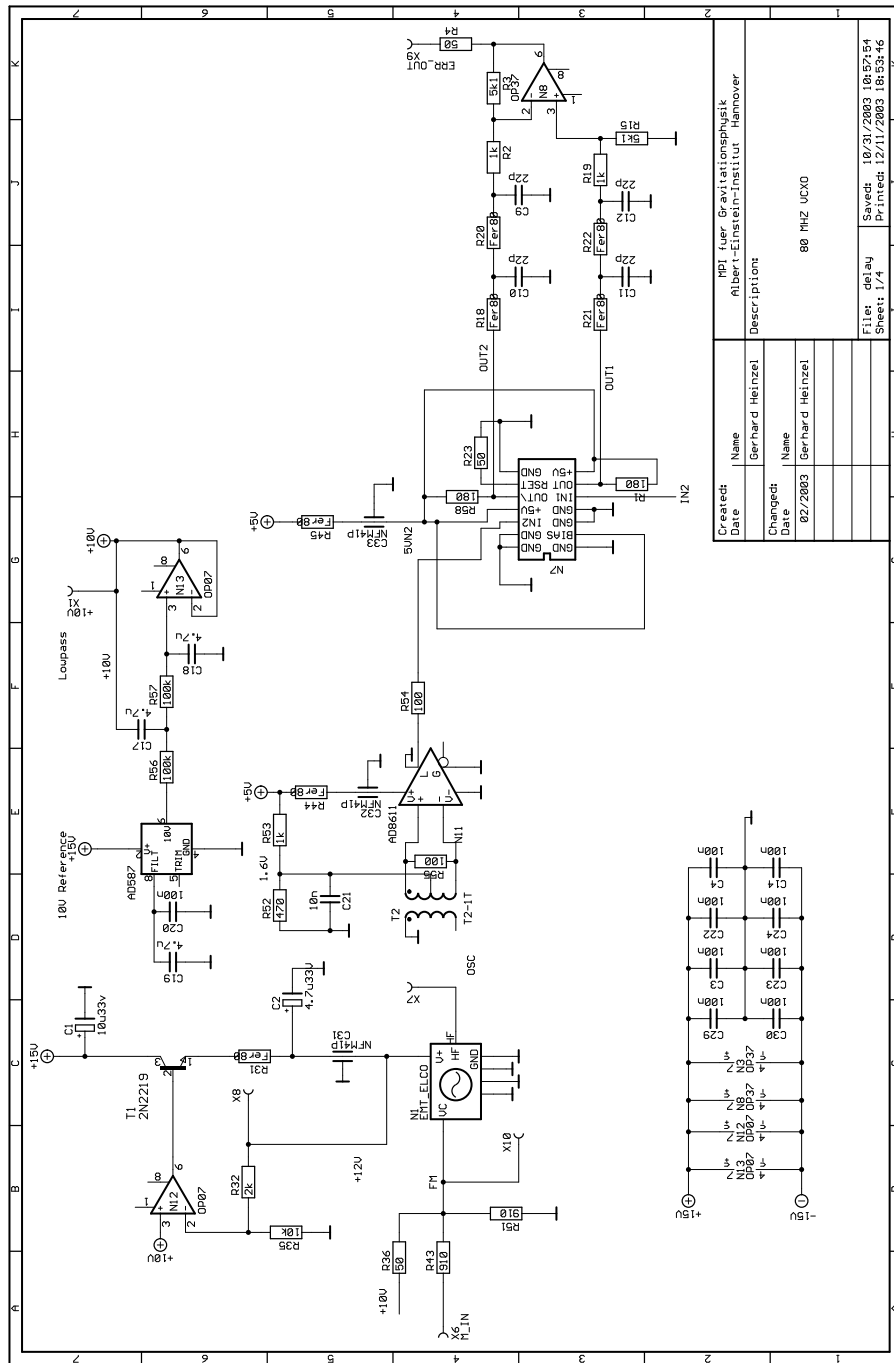
Figure B.3: Layout of the oscillator board for the arm-locking hardware simulation described in Chapter 6. Sheet 1.
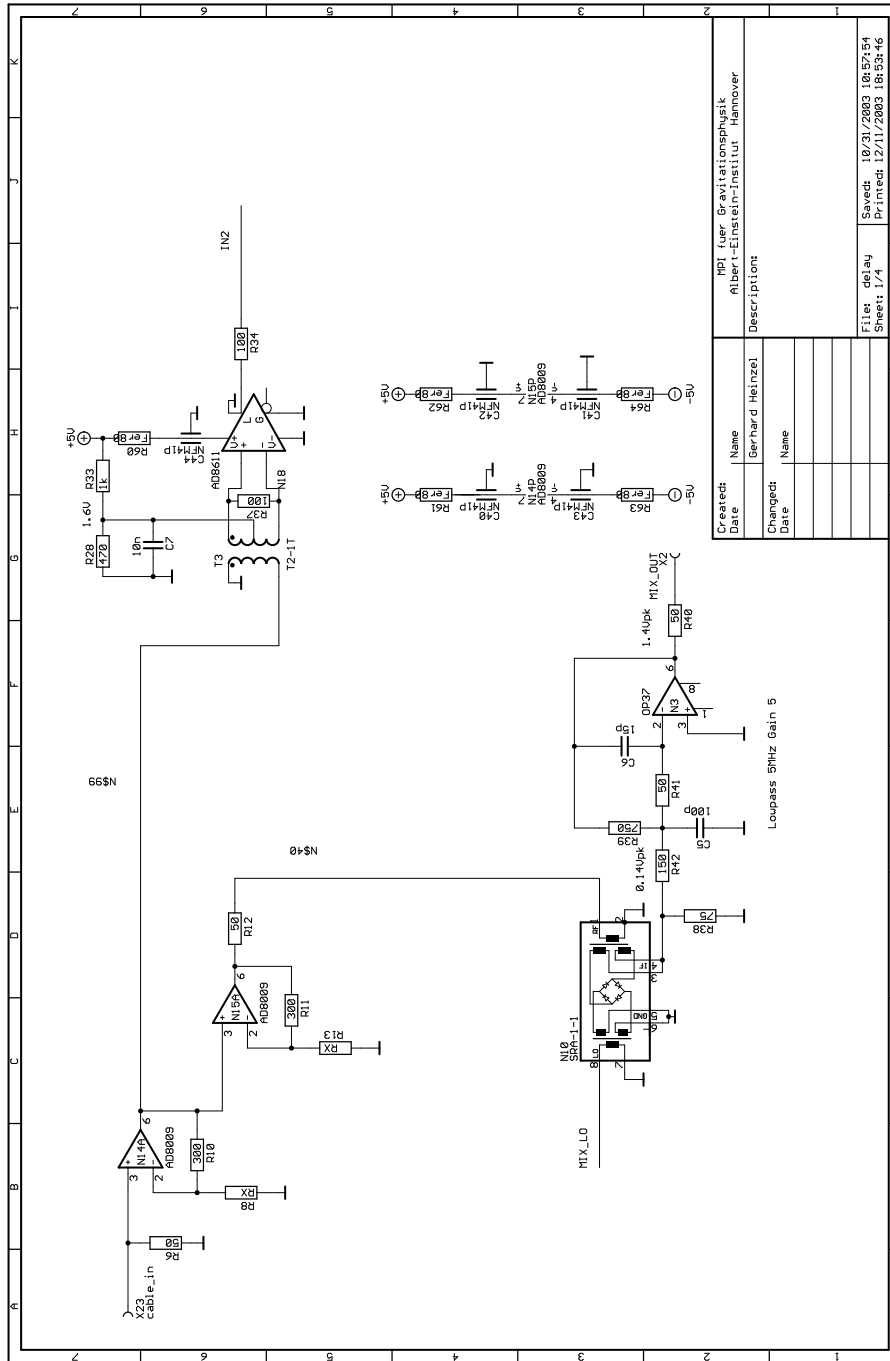
Figure B.4: Layout of the oscillator board for the arm-locking hardware simulation described in Chapter 6. Sheet 3.
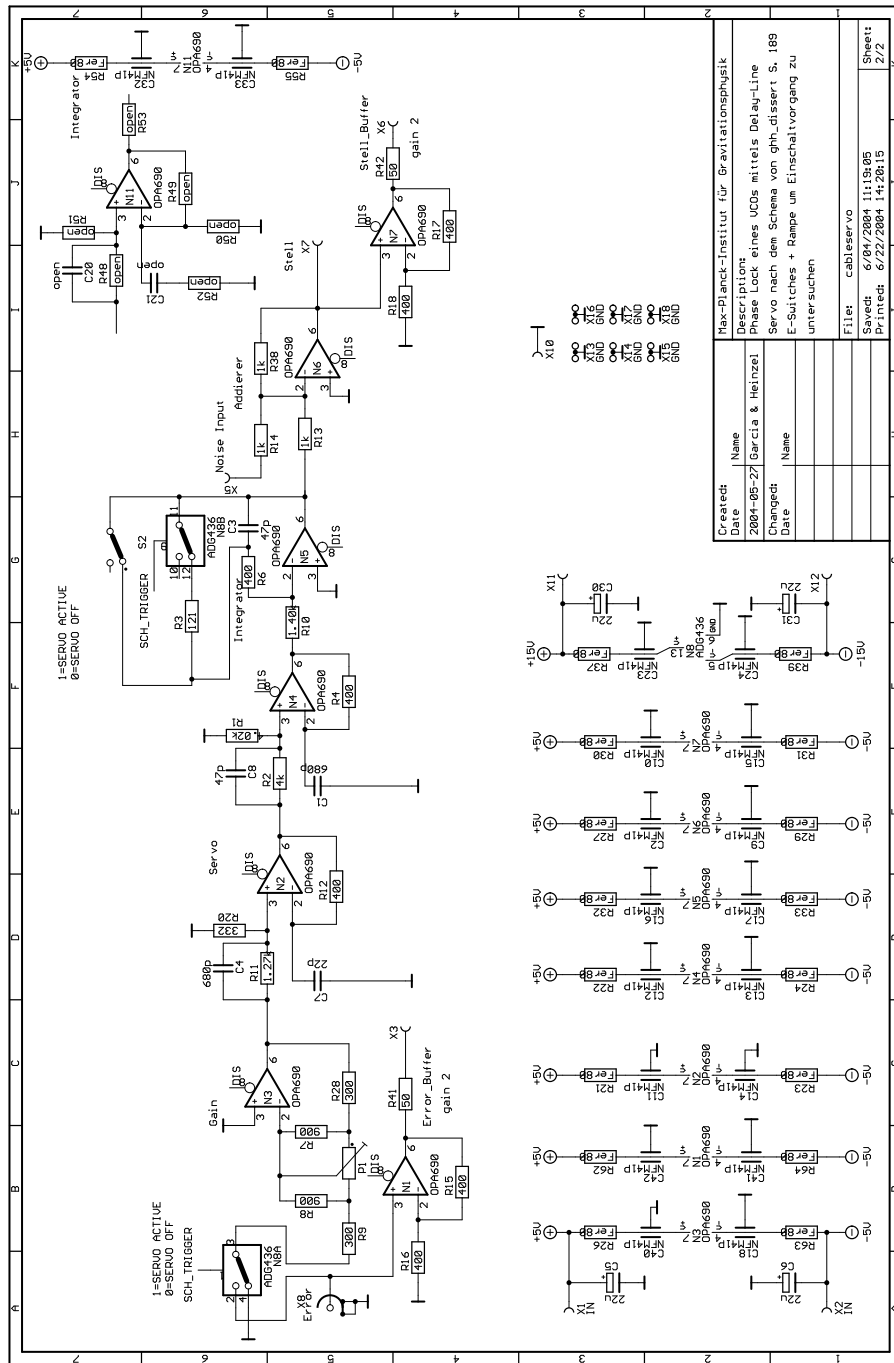
Figure B.5: Layout of the servo board for the arm-locking hardware simulation described in Chapter 6. Sheet 1.
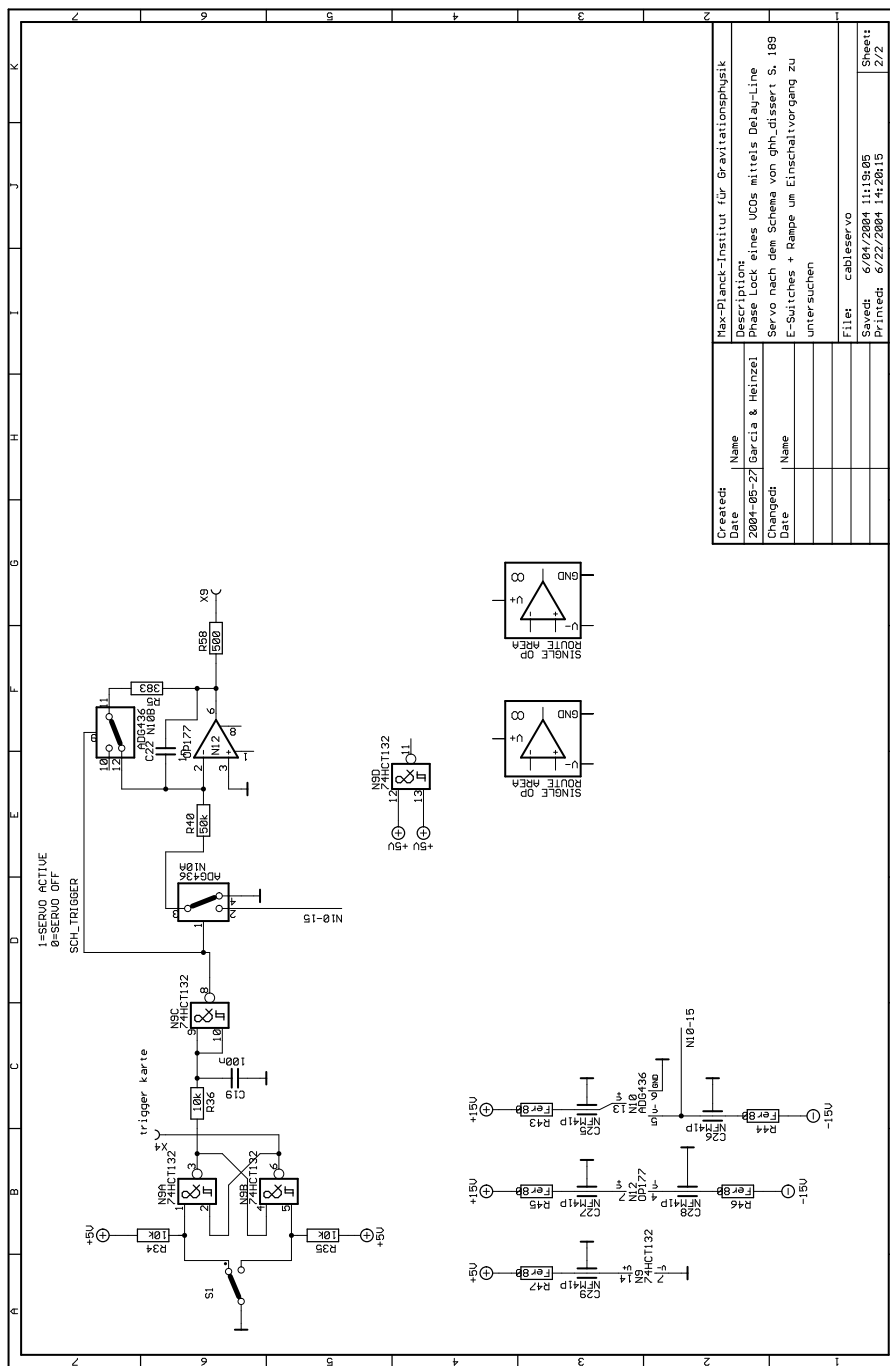
Figure B.6: Schmitt-trigger circuit used to switch the servo for the arm-locking hardware simulation described in Chapter 6.

Bibliography

[1] Peter R. Saulson. Status of Ground-Based Gravitational Wave Detectors. *AIP Conf Proc*, 873:41–48, November 2006. Merkowitz S and Livas JC eds Proceedings of the 6th LISA Symposium. ii

[2] LISA study team. LISA. Laser Intereferometer Space Antenna for the detection and observation of gravitational waves. 1998. Pre-Phase A Report (MPQ report 243). ix, 3, 4, 5, 60, 61, 80, 82

[3] `http://www.rssd.esa.int/index.php?project=LISAPATHFINDER&page=Index` and `http://sci.esa.int/lisapf`. Official ESA websites of the LISA Pathfinder project. ix, 9, 10, 12

[4] G. Heinzel. LISO: Linear Simulation and optimisation of analog circuits. see Appendix C of [42]. xi, 51, 73, 91

[5] K. Danzmann and the LISA Study Team. LISA - An ESA Cornerstone Mission for the Detection and Observation of Gravitational Waves. *Adv. Space Res.*, 32:1233–1242, 2003. 3

[6] K. Danzmann and A. Rüdiger. LISA technology – concept, status, prospect. *Class. Quantum Grav.*, 20:1–9, 2003. 3

[7] `http://www.lisa-science.org/`. Website of the LISA International Science Community (LISC). 3

[8] Oliver Jennrich. Proceedings of the Fifth International LISA Symposium. *Class. Quantum Grav.*, 22, April 2005. The material presented during the symposium can be found at `http://www.rssd.esa.int/index.php?project=SP\&page=LISA%20Symposium`. 3

[9] Merkowitz S and Livas JC eds. Proceedings of the Sixth International LISA Symposium. *AIP Conf Proc*, 873, November 2006. The material presented during the symposium can be found at `http://lisa6.gsfc.nasa.gov/conf/lisa6/program.html`. 3

[10] Astrium et al. LISA: Study of the Laser Interferometer Space Antenna, Final Technical Report. 2000. ESTEC Contract No 13631/99/NL/MS, Report No LI-RP-DS-009. 3, 60, 61

[11] LISA Study Team. *LISA Laser Interferometer Space Antenna*. ESA-SCI(2000)11, July 2000. 3, 80

[12] `http://www.rssd.esa.int/index.php?project=LISA&page=index` and `http://sci.esa.int/lisapf`. Official ESA websites of the LISA project. 3

[13] Ulrich A. Johann, Peter F. Gath, Wolfgang Holota, Hans Reiner Schulte, and Dennis Weise. Novel Payload Architectures for LISA. *AIP Conf Proc*, 873:304–311, November 2006. Merkowitz S and Livas JC eds Proceedings of the 6th LISA Symposium. 4

[14] D. Bortoluzzi, P. Bosetti, L. Carbone, A. Cavalleri, A. Ciccolella, M. Da Lio, K. Danzmann, R. Dolesi, A. Gianolio, G. Heinzel, D. Hoyland, C.D. Hoyle, M. Hueller, F. Nappo, M. Sallusti, P. Sarra, M. Te Plate, C. Tirabassi, S. Vitale, and W.J. Weber. Testing LISA drag-free control with the LISA technology package flight experiment. *Class. Quantum Grav.*, 20:89–97, 2003. 5, 9, 12

[15] Vitale S et al. LISA and its in-flight test precursor SMART-2. *Nucl. Phys. B (Proc. Suppl.)*, 110:209, 2002. 9

[16] S. Anza et al. The LTP experiment on the LISA Pathfinder mission. *Class. Quantum Grav.*, 22:125–138, 2005. 9, 12

[17] S. Vitale and K. Danzmann. LTPA-UTN-ScRD Science Requirements and Top-level Architecture Definition for the Lisa Technology Package (LTP) on Board LISA Pathfinder (SMART-2). July 2005. LPF project document. 9, 12

[18] M. Landgraf, M. Heckler, and S. Kemble. Mission Design for LISA Pathfinder. *Class. Quantum Grav.*, 22:487, 2005. 9

[19] C. J. Killow, J. Bogenstahl, F. Guzmán Cervantes, M. Perreur-Lloyd, D. I. Robertson, F. Steier, and H. Ward. Construction of the LTP Optical Bench Interferometer. *AIP Conf Proc*, 873:297–303, November 2006. Merkowitz S and Livas JC eds Proceedings of the 6th LISA Symposium. 10, 15

[20] G. Heinzel, C. Braxmaier, R. Schilling, A. Rüdiger, D. Robertson, M. te Plate, V. Wand, K. Arai, U. Johann, and K. Danzmann. Interferometry for the LISA technology package (LTP) aboard SMART-2. *Class. Quantum Grav.*, 20:153–161, 2003. 12, 13, 16, 93

[21] G. Heinzel, V. Wand, A. García, O. Jennrich, C. Braxmaier, D. Robertson, K.Middleton, D. Hoyland, A. Rüdiger, R. Schilling, U. Johann, and K Danzmann. The LTP interferometer and Phasemeter. *Class. Quantum Grav.*, 21:581–587, 2004. 13, 16, 17, 20, 24, 50, 93

[22] G. Heinzel, V. Wand, and A. García. Optical Bench for SMART-2 WP3100: Preinvestigation of Differential Wavefront Sensing and WP3200: Preinvestigation of Phasemeter. November 2002. LTP project technical note. 14, 17, 50

[23] V. Wand. Interferometrie und Phasenauslesung für die wissenschaftliche Weltraummission SMART2. Master's thesis, März 2003. Diplomarbeit. 14, 50

[24] F. Guzmán Cervantes. Real-time spatioally resolving phasemeter for LISA Pathfinder. Master's thesis, December 2004. Master thesis. 14

[25] E. J. Ellife, J. Bogenstahl, A. Deshpande, J. Hough, C. Killow, S. Reid, D. Robertson, S. Rowan, H. Ward, , and G. Cagnoli. Hydroxide-catalysis bonding for stable optical systems for space. *Class. Quantum Grav.*, 22:257–267, 2005. 15

[26] Robertson D et al. LTP interferometer - noise sources and performance. *Class. Quantum Grav.*, 22:155–163, 2005. 15, 26, 55, 69

[27] C. J. Killow. *Interferometry Developments for Spaceborne Gravitational Wave Detectors.* PhD thesis, 2005. PhD. thesis. 15, 17, 26, 42, 55, 58, 69

[28] G. Heinzel et al. S2-AEI-TN-3028 Investigation of noise sources in the LTP interferometer. 2005. LPF project document. ESTEC/Contract no. 18589/04/NL/HB. 17, 23, 24, 25, 50, 53, 59, 61, 78

[29] Felipe Guzmán Cervantes and Harry Ward. S2-UGL-TN-3016 Modifications to OBI Layout. April 2006. LTP project technical note. 17

[30] E. Morrison, B. J. Meers, D. I. Robertson, and H. Ward. Experimental demonstration of an automatic alignment system for optical interferometers and automatic alignment of optical interferometers. *Appl. Opt.*, 33:5037–5040 and 5041–5049, 1994. 20, 32

[31] G. Heinzel et al. S2-AEI-TN-3017 Lisa Pathfinder Optical Bench Engineering model: functional and performance tests - Test Report. 2004. LTP project technical note. 21, 26, 52, 63

[32] `http://www.innolight.de/products/mephisto/INNOLIGHT_Mephisto.pdf`. Innolight Mephisto datasheet. 22

[33] G. Heinzel, C. Braxmaier, M. Caldwell, K. Danzmann, F. Draaisma, A. García, J. Hough, O. Jennrich, U. Johann, C. Killow, K. Middleton, M. te Plate, D. Robertson, A. Rüdiger, R. Schilling, F. Steier, V. Wand, and H Ward. Successful testing of the LISA Technology Package (LTP) interferometer engineering model. *Class. Quantum Grav.*, 22:149–154, 2005. 23, 30

[34] C. Braxmeier, G. Heinzel, K.F. Middleton, M.E. Caldwell, W. Konrad, H. Stockburger, S. Lucarelli, M.B. te Plate, V. Wand, A.C. Garcia, F. Draaisma, J. Pijnenburg, D.I. Robertson, C. Killow, H. Ward, K. Danzmann, and U.A. Johann. LISA Pathfinder optical interferometry. *Proc. SPIE*, 5500:164–173, 2004. 23

[35] A. F. García Marín, V. Wand, F. Steier, F. Guzmán Cervantes, J. Bogenstahl, O. Jennrich, G. Heinzel, and K Danzmann1. On-orbit alignment and diagnostics for the LISA Technology Package. *Class. Quantum Grav.*, 23:133–140, 2006. 29

[36] G. Heinzel, A. García, V. Wand, and F. Steier. S2-AEI-TN-3020 LTP alignment procedure. December 2004. LTP project technical note. 29

[37] U. Denskat et al. S2-ASD-RS-3018 PHASEMETER PROCESSING AND LASER CONTROL. 09 2006. LTP project technical note. 29, 34, 53

[38] M. Armano, K. Danzmann, R. Dolesi, A. Garcia Marin, G. Heinzel, M. Hueller, S. Vitale, and W. Weber. S2-UTN-PL-3001. LTP Experiment Operation Master Plan. March 2005. LTP project technical note. 34, 54, 60

[39] Thilo Schuldt, Hans-Jürgen Kraus, Dennis Weise, Achim Peters, Ulrich Johann, and Claus Braxmaier. A High Sensitivity Heterodyne Interferometer as Optical Readout for the LISA Inertial Sensor. *AIP Conf Proc*, 873:374–378, November 2006. Merkowitz S and Livas JC eds Proceedings of the 6th LISA Symposium. 35

[40] Stuart M. Aston and Clive C. Speake. An Interferometric Based Optical Read-Out Scheme For The LISA Proof-Mass. *AIP Conf Proc*, 873:326–333, November 2006. Merkowitz S and Livas JC eds Proceedings of the 6th LISA Symposium. 35

[41] Fausto Acernese, Rosario De Rosa, Luciano Di Fiore, Fabio Garufi, Adele La Rana, and Leopoldo Milano. Some Progress In The Development Of An Optical Readout System For The LISA Gravitational Reference Sensor. *AIP Conf Proc*, 873:339–343, November 2006. Merkowitz S and Livas JC eds Proceedings of the 6th LISA Symposium. 35

[42] G. Heinzel. Advanced optical techniques for laser-interferomertric gravitational-wave detectors. 1999. University of Hannover and MPQ report 243. 39, 92, 147

[43] F. Steier, A. Garcia, V.Wand, and G. Heinzel. S2-AEI-TN-3022 LTP Extra Modes Definition. February 2005. LTP project technical note. 54, 60

[44] M. Tröbs. *Laser development and charaterization for the spaceborne interferometric gravitational wave detector LISA*. PhD thesis, 2005. Universität Hannover. 57, 81

[45] A. Freise. *The Next Generation of Interferometry: Multi-Frequency Optical Modelling, Control Concepts and Implementation*. PhD thesis, 2003. 57, 88

[46] R.W.P. Drever and J.L. Hall F.V. Kowalski J. Hough G.M. Ford A.J. Munley H. Ward. Laser Phase and Frequency Stabilization Using an Optical Resonator. *Appl. Phys. B*, 31:133–140, 1983. 57, 60, 81

[47] A. García, G. Heinzel, V. Wand, F. Steier, and F.Guzmán. S2-AEI-TN-3035. Performance analysis of the fast LTP interferometric control loops: OPD and Laser frequency. September 2006. LTP project technical note. 61, 66, 70

[48] NTE. S2-ASD-RS-3004 DDS Subsystem Specification. June 2006. LISA Pathfinder project. 66

[49] J.G. Burnett et al. Birefringence compensated cylindrical piezoelectric fibre phase modulator. *Journal of Modern Optics*, 43:583–589, 1996. 71

[50] D.G. Luke et al. Polarization-Maintaining Single-Mode Fiber Piezoelectric Phase Modulators. *Optics Communications*, 121:115–120, 1995. 71

[51] F. Steier. Methoden zur thermo-optischen Charakterisierung optischer Komponenten. Master's thesis, Juni 2004. Diplomarbeit. 75

[52] R. Logan, L. Maleki, and M. Shadaram. Stabilization of Oscillator Phase Using a Fibre Optic Delay Line. *Proceedings of the 45th Annual Symposium on Frequency Control*, May 1991. 79, 98

[53] B. S. Sheard, M. B. Gray, D. E. McClelland, and D. A. Shaddock. Laser frequency stabilization by locking to a LISA arm. *Physics Letters A*, 320:9–21, 2003. 79, 81, 91, 92, 97

[54] R. Schilling. LIST Meeting Presentation, July 2003. 79

[55] B. Schumaker. LIST Meeting Presentation, July 2003. 79

[56] M. Tinto and M. Rakhmanov. On the laser frequency stabilization by locking to a LISA arm. *arXiv:gr-qc/0408076*. 79, 97

[57] B. S. Sheard, M. B. Gray, D. A. Shaddock, and D. E. McClelland. Laser frequency noise suppression by arm-locking in LISA: progress towards a bench-top demonstration. *Class. Quantum Grav.*, 22(10):221–226, 2005. 81, 98

[58] B. S. Sheard. *Arm locking for space-based gravitational wave detectors and optomechanical effects in interferometers*. PhD thesis, 2005. The Australian National University. 81, 82, 98

[59] J. I. Thorpe, R. J. Cruz, S. R. Sankar, G. Mueller, , and P. McNamara. First step toward a benchtop model of the Laser Interferometer Space Antenna. *Opt. Lett.*, 29:2843–2845, 2004. 81, 98

[60] M. Herz. Active laser frequency stabilization and resolution enhancement of interferometers for the measurement of gravitational waves in space. *Opt. eng.*, 44, 2005. 81, 96, 98

[61] M.Tinto, D.A. Shaddock, J. Sylvestre, and J.W.Amstrong. Implementation of Time-Delay Interferometry for LISA. *Phys. Rev. D*, 67, 2003. 81, 82

[62] D. A. Shaddock, B. Ware, R. E. Spero, and M. Vallisneri. Post-processed time-delay interferometry for LISA. *Phys. Rev. D*, 70, 2004. 81

[63] G. Heinzel, A. Rüdiger, and R. Schilling. Spectrum and spectral density estimation by the Discrete Fourier transform (DFT), including a comprehensive list of window functions and some new at-top windows. 2002. Technical note. 85

[64] Yves Surrel. Fringe analysis. *Photomechanics, Topics Appl. Phys.*, 77:55–102, 2000. 93

[65] Michael Tröbs and Gerhard Heinzel. Improved spectrum estimation from digitized time series on a logarithmic frequency axes. *Measurement*, 39:120–129, February 2006. 95

[66] D. Shaddock. Arm-locking: Improvements and impact. LISA Technical Interchange Meeting, September 2005. 96, 98

[67] Benjamin S. Sheard, Malcolm B. Gray, and David E. McClelland. High-bandwidth laser frequency stabilization to a fiber-optic delay line. *Applied Optics*, 45:8491–8499, 2006. 98

[68] J. I. Thorpe and G. Mueller. Experimental verification of armlocking for LISA using electronic phase delay. *Phys. Lett. A*, 342:199–204, July 2005. 98

[69] J. I. Thorpe, R. J. Cruz, S. R. Sankar, G. Mueller, , and P. McNamara. Electronic phase delay–A first step towards a bench-top model of LISA. *Class. Quantum Grav.*, 22:227–234, 2005. 98

[70] A. F. García Marín, J. Bogenstahl, F. Guzmán Cervantes, F. Steier, J. Reiche, S. Skorupka, V. Wand, M. Nofrarias, J. Sanjuan, O. Jennrich, G. Heinzel, and K. Danzmann. Interferometric characterization of the optical window for LISA Pathfinder and LISA. *AIP Conf Proc*, 873:344–348, November 2006. Merkowitz S and Livas JC eds Proceedings of the 6th LISA Symposium. 99

[71] M. Nofrarias, A. F. García Marín, and J. Sanjuan. S2-AEI-TN-3016 S2-IEEC-TN-3019 Optical window characterization. October 2006. LTP project technical note. 99

[72] G. Heinzel. S2-AEI-TN-3016 Requirements on LPF optical windows. June 2004. LTP project technical note. 99

[73] `www.ohara-gmbh.com/e/katalog/downloads/techinfo_e.pdf`. Properties of Ohara glasses. 107

[74] `www.schott.com/optics_devices/english/download/tie-27_stress_in_optical_glass.pf`. 107

[75] `asm.matweb.com`. Properties of Titanium. 108

[76] Carlo Gavacci Space. Optical window breadboard. Personal technical note. 110

[77] Carlo Gavacci Space. Optical window assembly leak test report. October 2005. LTP project technical note. 111

[78] J. Ramos and J. Sanjuan. S2-UPC-DDD-3001 DDS Thermal Diagnostic Prototype Design. April 2005. LTP project technical note. 113

[79] J. Bogenstahl. Interferometer zur Charakterisierung von optischen Komponenten. Master's thesis, 2005. Diplomarbeit. 113

[80] Frank Steier, Felipe Guzmán, and Gerhard Heinzel. S2-AEI-TN-3041 Beam Clipping and Angular Noise Subtraction in the LTP Interferometer. April 2007. LTP project technical note. 120

[81] J. Sanjuán, J. Ramos-Castro, A. Lobo, M. Nofrarias, and P.J. Riu. Thermal diagnostics Front-End Electronics for LISA Pathfinder. *Submitted to Rev. Sci. Instrum.*, June 2007. 123

[82] H. G. Grothues. S2-DLR-TN-3001 Preparation of Particle Irradiation Tests of OHARA S-PHM52 Optical Glass Windows. July 2005. LTP project technical note. 126

[83] `www.hmi.de`. Hahn-Meitner-Institute. 126

[84] J.-M. Costantini and F. Beuneu. Thermal recovery of colour centres induced in cubic yttria-stabilized zirconia by charged particle irradiations. *J. Phys.: Condens. Matter*, 18:3671–3682, 2006. 128

[85] J. B. Breckinridge and A. J. Marker. Damage to space optics and properties and characteristics of optical glass. *Proceedings of SPIE*, 1761:46–57, January 1993. 131, 132

[86] M. Nofrarias, A.F. García Marín, A. Lobo, G. Heinzel, J. Ramos-Castro, J. Sanjuán, and K Danzmann2. Thermal diagnostic of the Optical Window on board LISA PathFinder. *Class. Quantum Grav.*, 24:5103–5121, 2007. 132

[87] M. Nofrarias, A. F. García Marín, G. Heinzel, A. Lobo, J. Ramos-Castro, J. Sanjuan, and K. Danzmann. Thermal diagnostic test in the LTP experiment. *AIP Conf Proc*, 873:199–203, November 2006. Merkowitz S and Livas JC eds Proceedings of the 6th LISA Symposium. 132

Acknowledgements

Curriculum Vitae

Antonio Francisco García Marín
Tulpenstr. 12
30167 Hannover

born on May 6$^{\text{th}}$, 1979 in Almería, Spain

1993–1997	Bachillerato and COU
06.1997	Selectividad (corresponds to Abitur)
10.1997–09.2002	Physics Studies, Universidad de Granada, Spain
10.2000–08.2001	Physics Studies, Universität Hannover
09.2002	Licenciado en Física (corresponds to Diplom), Universidad de Granada
since 10.2002	Scientific Assistant, Max-Planck-Institut für Gravitationsphysik (Albert-Einstein-Institut), Hannover Doctoral Studies in Physics, Universität Hannover

Publications

- A.F. García Marín, G. Heinzel, R. Schilling, A. Rüdiger, V. Wand, F. Steier, F. Guzmán Cervantes, A. Weidner, O. Jennrich, F.J. Meca Meca, K. Danzmann "Phase locking to a LISA arm: first results of a hardware model" Class. Quantum Grav. 22 (2005) S235 S242

- S Anza et al, "The LTP experiment on the LISA Pathfinder mission", Class. Quantum Grav. 22 S125-S138

- G Heinzel, C Braxmaier, M Caldwell, K Danzmann, F Draaisma, A García, J Hough, O Jennrich, U Johann, C Killow, K Middleton, M te Plate, D Robertson, A Rüdiger, R Schilling, F Steier, V Wand and H Ward, "Successful testing of the LISA Technology Package (LTP) interferometer engineering model", Class. Quantum Grav. 22 S149-S154

- David Robertson, Christian Killow, Harry Ward, Jim Hough, Gerhard Heinzel, Antonio Garcia, Vinzenz Wand, Ulrich Johann and Claus Braxmaier, "LTP interferometer-noise sources and performance", 2005 Class. Quantum Grav. 22 S55-S163

- A.F. García Marín, V. Wand, F. Steier, F. Guzmán Cervantes, J. Bogenstahl, O. Jennrich, G. Heinzel, K. Danzmann ,"On-orbit alignment and diagnostics for the LISA Technology Package", Class. Quantum Grav. 23 (2006) S133 - S140

- V. Wand, J. Bogenstahl, C. Braxmaier, K. Danzmann, A. García, F. Guzmán, G. Heinzel, J. Hough, O. Jennrich, C. Killow, D. Robertson, Z. Sodnik, F. Steier, H. Ward, ,"Noise sources in the LTP heterodyne interferometer", Class. Quantum Grav. 23 (2006) S159 - S167

- G. Heinzel, J. Bogenstahl, C. Braxmaier, K. Danzmann, A. García, F. Guzmán, J. Hough, D. Hoyland, O. Jennrich, C. Killow, D. Robertson, Z. Sodnik, F. Steier, H. Ward, V. Wand ,"Interferometry for the LISA technology package LTP: an update", J. Phys.: Conf. Ser. 32 (2006) 132 - 136

- A. F. García Marín, J. Bogenstahl, F. Guzmán Cervantes, F. Steier, J. Reiche, S. Skorupka, V. Wand, M. Nofrarias, J. Sanjuan, O. Jennrich, G. Heinzel, K. Danzmann, "Interferometric characterization of the optical window for LISA Pathfinder and LISA", AIP Conf. Proc. 873 (2006) 344-348

- M. Nofrarias, A. F. García Marín, G. Heinzel, A. Lobo, J. Ramos-Castro, J. Sanjuan, K. Danzmann, "Thermal diagnostic test in the LTP experiment", AIP Conf. Proc. 873 (2006) 199-203

- C. Braxmeier, G. Heinzel, K.F. Middleton, M.E. Caldwell, W. Konrad, H. Stockburger, S. Lucarelli, M.B. te Plate, V. Wand, A.C. Garcia, F. Draaisma, J. Pijnenburg, D.I. Robertson, C. Killow, H. Ward, K. Danzmann, U.A. Johann: 'LISA Pathfinder optical interferometry" in: J. Hough, G.H. Sanders (eds.) Gravitational Wave and Particle Astrophysics Detectors. Proc. SPIE 5500 (2004) 164 - 173

- G. Heinzel, V. Wand, A. García, O. Jennrich, C. Braxmeier, D. Robertson, K. Middleton, D. Hoyland, A. Rüdiger, R. Schilling, U. Johann, K. Danzmann, "The LTP interferometer and phasemeter", Class. Quantum Grav. 21 (2004) S581 - S587

- Felipe Guzmán Cervantes, Gerhard Heinzel, Antonio F. García Marín, Vinzenz Wand, Frank Steier, Oliver Jennrich,2 and Karsten Danzmann, "Real-time phasefront detector for heterodyne interferometers", Vol. 46, No. 23 Applied optics

- M. Nofrarias, A.F. García Marín, A. Lobo, G. Heinzel, J. Ramos-Castro, J. Sanjuan, and K Danzmann, "Thermal diagnostic of the Optical Window on board LISA PathFinder", In preparation for submission to Classical and quantum gravity.

- A. F. García Marín, G. Heinzel and K. Danzmann on behalf of the LISA community: "LISA and its precursor LISA Pathfinder", Proceedings of science, International Europhysics Conference on High Energy Physics July 21st - 27th 2005 Lisboa, Portugal

- A. F. García Marín et al: "Interferometry for LISA and LISA Pathfinder", J. Phys.: Conf. Ser. 66, XXIXth Spanish Relativity Meeting (ERE 2006)